

AD-A131 267

NUMERICAL SIMULATION OF THE VELOCITY RECORDS FROM THE  
SRI GROUT SPHERES EXPERIMENTS(U) S-CUBED LA JOLLA CA  
N RIMER ET AL. 01 SEP 82 SSS-R-82-5580 DNA-TR-82-54

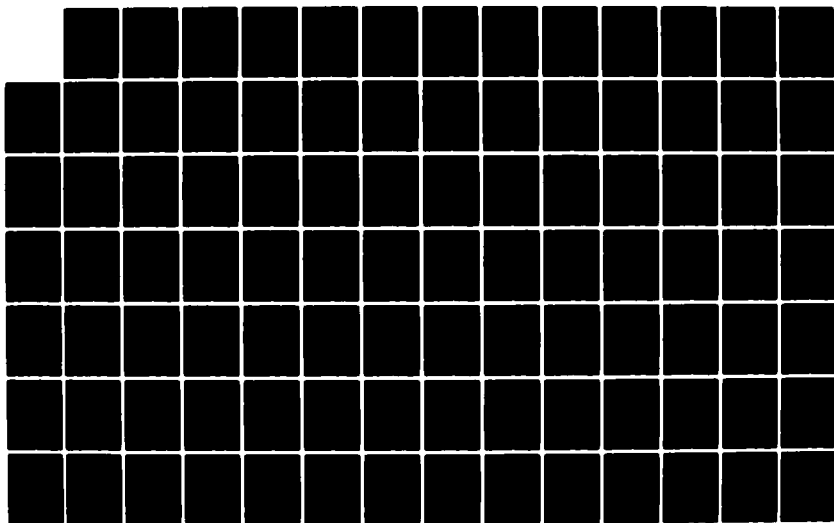
1/2

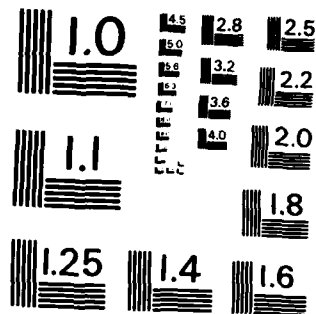
UNCLASSIFIED

DNA001-82-C-0043

F/G 20/11

NL





MICROCOPY RESOLUTION TEST CHART  
NATIONAL BUREAU OF STANDARDS-1963-A

ADA 131267

12

DNA-TR-82-54

# NUMERICAL SIMULATION OF THE VELOCITY RECORDS FROM THE SRI GROUT SPHERES EXPERIMENTS

N. Rimer  
K. Lie  
S-CUBED  
P.O. Box 1620  
La Jolla, California 92038

1 September 1982

Technical Report

CONTRACT No. DNA 001-82-C-0043

APPROVED FOR PUBLIC RELEASE;  
DISTRIBUTION UNLIMITED.

THIS WORK WAS SPONSORED BY THE DEFENSE NUCLEAR AGENCY  
UNDER RDT&E RMSS CODES S400082466 J26BAXYX00002 H2590D  
AND S400082466 J24AAXYX00037 H2590D.

DTIC FILE COPY

Prepared for  
Director  
DEFENSE NUCLEAR AGENCY  
Washington, DC 20305

DTIC  
ELECTE  
AUG 11 1983

B

82

Destroy this report when it is no longer  
needed. Do not return to sender.

PLEASE NOTIFY THE DEFENSE NUCLEAR AGENCY,  
ATTN: STTI, WASHINGTON, D.C. 20305, IF  
YOUR ADDRESS IS INCORRECT, IF YOU WISH TO  
BE DELETED FROM THE DISTRIBUTION LIST, OR  
IF THE ADDRESSEE IS NO LONGER EMPLOYED BY  
YOUR ORGANIZATION.



UNCLASSIFIED

SECURITY CLASSIFICATION OF THIS PAGE (When Data Entered)

REPORT DOCUMENTATION PAGE		READ INSTRUCTIONS BEFORE COMPLETING FORM
1. REPORT NUMBER DNA-TR-82-54	2. GOVT ACCESSION NO. ADA131 267	3. RECIPIENT'S CATALOG NUMBER
4. TITLE (and Subtitle) NUMERICAL SIMULATION OF THE VELOCITY RECORDS FROM THE SRI GROUT SPHERES EXPERIMENTS		5. TYPE OF REPORT & PERIOD COVERED Technical Report
7. AUTHOR(s) N. Rimer K. Lie		6. PERFORMING ORG. REPORT NUMBER SSS-R-82-5580
9. PERFORMING ORGANIZATION NAME AND ADDRESS S-CUBED P. O. Box 1620 La Jolla, CA 92038		8. CONTRACT OR GRANT NUMBER(s) DNA 001-82-C-0043
11. CONTROLLING OFFICE NAME AND ADDRESS Director Defense Nuclear Agency Washington, DC 20305		10. PROGRAM ELEMENT, PROJECT, TASK AREA & WORK UNIT NUMBERS Tasks J26BAXYX-00002 J24AAXYX-00037
14. MONITORING AGENCY NAME & ADDRESS (if different from Controlling Office) Field Command Defense Nuclear Agency Kirtland Air Force Base, NM 87115		12. REPORT DATE 1 September 1982
		13. NUMBER OF PAGES 150
		15. SECURITY CLASS. (of this report) Unclassified
		15a. DECLASSIFICATION/DOWNGRADING SCHEDULE NA since UNCLASSIFIED
16. DISTRIBUTION STATEMENT (of this Report)  Approved for public release; distribution unlimited.		
17. DISTRIBUTION STATEMENT (of the abstract entered in Block 20, if different from Report)		
18. SUPPLEMENTARY NOTES  This work was sponsored by the Defense Nuclear Agency under RDT&E RMSS Codes S400082466 J26BAXYX00002 H2590D and S400082466 J24AAXYX00037 H2590D.		
19. KEY WORDS (Continue on reverse side if necessary and identify by block number) Residual Stress Fields Shock Damage Effective Stress Model Alluvium Simulant Strain Rate Dependence P- $\alpha$ Model Stress Relaxation Particle Velocity Measurements Maxwell Solid Pore Fluid Pressure		
20. ABSTRACT (Continue on reverse side if necessary and identify by block number)  Spherically symmetric finite difference calculations are presented here which successfully simulate the particle velocity measurements from the small scale grout spheres experiments performed at SRI International and show that particle velocity measurements together with numerical simulations may be used to obtain dynamic material properties. In these experiments, 3/8 gm charges of PETN explosive are detonated in 11" diameter spheres of grout in a water tank which simulates overburden. Numerical simulations are presented for experiments		

DD FORM 1 JAN 73 1473 EDITION OF 1 NOV 65 IS OBSOLETE

UNCLASSIFIED

SECURITY CLASSIFICATION OF THIS PAGE (When Data Entered)

## 20. Abstract (continued)

in two types of grout, 2C4 rock-matching grout and a high-porosity, low-density grout, LD2C4. Successful matches to the particle velocity pulses are obtained for each grout using two very different numerical constitutive models, a strain rate and shock damage dependent model (the RDD model) and the rate independent effective stress model. For 2C4 grout, the simulations involve primarily changes in the laboratory measured static failure surface to account for increases in the strength during shock loading and decreases in the strength on unload. For LD2C4 grout, the simulations involve primarily backing out a loading (air void crushup) curve from the particle velocity measurement. Small changes in this curve at pressures below 0.25 Kb are shown to cause large variations in the calculated peak particle velocities and in the pulse shape. A later laboratory measurement of this crush curve is shown to be in excellent agreement with the crush curve derived from the particle velocity measurements.

## PREFACE

The continued support of Mr. Carl Keller, DNA Field Command, for both the laboratory and computational efforts made this work possible. His judgement in persisting with the grout spheres experiments, in spite of criticisms from the author, among others, has made possible the development of these powerful experimental and calculational tools for containment science and material properties investigations.

✓	
By _____	
Distribution/ _____	
Availability Codes	
Dist	Avail and/or Special
A	



# TABLE OF CONTENTS

<u>Section</u>	<u>Page</u>
PREFACE	1
LIST OF ILLUSTRATIONS- - - - -	
1 LIST OF TABLES- - - - -	
2 INTRODUCTION AND SUMMARY - - - - -	11
CONSTITUTIVE MODELS FOR 2C4 ROCK-MATCHING GROUT- - - - -	29
2.1 CHARACTERIZATION OF THE PETN EXPLOSIVE- - - - -	29
2.2 EQUATION OF STATE FOR THE LUCITE SHELL- - - - -	30
2.3 MATERIAL PROPERTIES FOR 2C4 ROCK MATCHING GROUT- - - - -	33
2.4 THE EFFECTS OF CONSTITUTIVE MODELING CHANGES ON THE PARTICLE VELOCITIES- - - - -	44
2.5 THE RATE AND DAMAGE DEPENDENT (RDD) CONSTITUTIVE MODELS- - - - -	54
3 2.6 UNIQUENESS - - - - -	64
EFFECTIVE STRESS MODELS FOR 2C4 GROUT- - - - -	81
3.1 THE EFFECTIVE STRESS MODEL- - - - -	81
3.2 RESULTS FOR 2C4 GROUT- - - - -	83
4 3.3 A PROPOSED GROUT SPHERES SCALING EXPERIMENT- - - - -	93
CONSTITUTIVE MODELS FOR HIGH POROSITY LD2C4 GROUT- - - - -	107
4.1 MATERIAL PROPERTIES FOR LD2C4 GROUT - - - - -	108
4.2 THE INFLUENCE OF CRUSH CURVE UPON PARTICLE VELOCITY- - - - -	112
4.3 EFFECTIVE STRESS CALCULATIONS FOR LD2C4 GROUT- - - - -	128
5 4.4 IMPLICATION FOR CONTAINMENT- - - - -	140
CONCLUSIONS - - - - -	142
REFERENCES- - - - -	145



# LIST OF ILLUSTRATIONS

<u>Figure</u>	<u>Page</u>
1.1 Comparison between measured and calculated particle velocities in 2C4 grout at a range of 1.27 cm- - - - -	13
1.2 Comprison between measured and calculated particle velocities in 2C4 grout at a range of 1.90 cm- - - - -	14
1.3 Comparison between measured and calculated particle velocities in 2C4 grout at a range of 2.54 cm - - - - -	15
1.4 Comparison between measured and calculated particle velocities in 2C4 grout at a range of 4.0 cm- - - - -	16
1.5 Calculated "residual" stresses for 2C4 grout at 80 $\mu$ s- - - - -	17
1.6 Comparison between measured and calculated particle velocities in LD2C4 grout at a range of 1.27 cm- - - - -	20
1.7 Comparison between measured and calculated particle velocities in LD2C4 grout at a range of 1.90 cm- - - - -	21
1.8 Comparison between measured and calculated particle velocities in LD2C4 grout at a range of 2.54 cm- - - - -	22
1.9 Comparison between measured and calculated particle velocities in LD2C4 grout at a range of 4.0 cm- - - - -	23
1.10 Calculated residual stresses for LD2C4 grout at 85 $\mu$ s- - - - -	24
1.11 Crush curve for LD2C4 grout- - - - -	25
2.1 Peak velocity vs. range for 2C4 grout- - - - -	32
2.2 Crush curve for 2C4 grout- - - - -	37
2.3 Failure surfaces for 2C4 rock matching grout- - - - -	39
2.4 Triaxial compression tests, at different confining pressures, undrained- - - - -	40
2.5 Comparison between measured particle velocities at a range of 1.90 cm in 2C4 grout and a calculation using the static laboratory measured failure surface- - - - -	45
2.6 Comparison between measured particle velocities at a range of 1.90 cm in 2C4 grout and a calculation using strain rate dependent increases in strength- - - - -	46

# LIST OF ILLUSTRATIONS (Continued)

<u>Figure</u>		<u>Page</u>
2.7	Comparison between measured particle velocities at 1.90 cm in 2C4 grout and a calculation using both strain rate dependent increases in strength and shock damage dependent decreases in strength- - - - -	48
2.8	Comparison between measured particle velocities at 1.90 cm in 2C4 grout and a calculation including strain rate dependent increases in strength and shock damage dependent decreases in both strength and shear modulus- - - - -	51
2.9	Comparison between measured particle velocities at a range of 1.90 cm in 2C4 grout and a calculation with strain rate dependent increases in strength but not for damaged grout- - -	52
2.10	Comparison between measured velocities in 2C4 grout at a range of 1.90 cm and a calculation in which strain rate dependent increases in strength were gradually reduced to zero for increasing shock damage- - - - -	53
2.11	Comparison between measured velocities in 2C4 grout at a range of 1.90 cm and a calculation using the RDD constitutive models with $V_c$ corresponding to the crush pressure, $\delta$ equal to 0.2 $\mu$ sec, and 1.8 percent air-filled porosity- - - - -	61
2.12	Comparison between measured velocities in 2C4 grout at a range of 1.90 cm, and a calculation using the RDD constitutive models with $V_c$ corresponding to a pressure of 1.0 Kb, $\delta$ equal to 1.0 $\mu$ sec, and 1.8 percent air-filled porosity- - - - -	62
2.13	Comparison between measured velocities in 2C4 grout at a range of 1.90 cm and a calculation using the RDD constitutive models with $V_c$ corresponding to a pressure of 1.5 Kb, $\delta$ equal to 1.0 $\mu$ sec, and 1.8 percent air-filled porosity- - - - -	63
2.14	Comparison between measured velocities in 2C4 grout at 1.27 cm and a calculation using the RDD constitutive models with $\delta$ equal to 2.0 $\mu$ sec and the original JWL coefficients for PETN- - - -	65
2.15	Comparison between measured velocities in 2C4 grout at 1.90 cm and a calculation using the RDD constitutive models with $\delta$ equal to 2.0 $\mu$ sec and the original JWL coefficients for PETN- - - -	66
2.16	Comparison between measured velocities in 2C4 grout at 2.54 cm and a calculation using the RDD constitutive models with $\delta$ equal to 2.0 $\mu$ sec and the original JWL coefficients for PETN- - - -	67
2.17	Comparison between measured velocities in 2C4 grout at 4.0 cm and a calculation using the RDD constitutive models with $\delta$ equal to 2.0 $\mu$ sec and the original JWL coefficients for PETN- - - -	68

# LIST OF ILLUSTRATIONS (Continued)

<u>Figure</u>	<u>Page</u>
2.18 Calculated "residual" stresses for 2C4 grout at 80 $\mu$ sec using the RDD constitutive models with $\delta$ equal to 2.0 $\mu$ sec and the original JWL coefficients for PETN- - - - -	69
2.19 Comparisons between measured velocities in 2C4 grout at a range of 1.90 cm and a calculation using the RDD constitutive models ( $\delta$ equal to 1. $\mu$ sec and $V_c$ corresponding to a pressure of 1.5 Kb) without shear modulus reduction due to damage - - - -	71
2.20 Comparison between measured velocities in 2C4 grout at a range of 1.27 cm and a calculation using the RDD constitutive models without shear modulus reduction due to damage, $\delta$ equal to 0.4 $\mu$ sec and $V_c$ corresponding to 1.5 Kb pressure - - - - -	72
2.21 Comparison between measured velocities in 2C4 grout at a range of 1.90 cm and a calculation using the RDD constitutive models without shear modulus reduction due to damage, $\delta$ equal to 0.4 $\mu$ sec and $V_c$ corresponding to 1.5 Kb pressure - - - - -	73
2.22 Comparison between measured velocities in 2C4 grout at a range of 2.54 cm and a calculation using the RDD constitutive models without shear modulus reduction due to damage, $\delta$ equal to 0.4 $\mu$ sec and $V_c$ corresponding to 1.5 Kb pressure - - - - -	74
2.23 Comparison between measured velocities in 2C4 grout at a range of 4.0 cm and a calculation using the RDD constitutive models without shear modulus reduction due to damage, $\delta$ equal to 0.4 $\mu$ sec and $V_c$ corresponding to 1.5 Kb pressure - - - - -	75
2.24 Comparison between measured velocities in 2C4 grout at a range of 1.27 cm and a calculation using the RDD constitutive models without shear modulus reduction due to damage, $\delta$ equal to 0.6 $\mu$ sec and $V_c$ corresponding to 1.0 Kb peak pressure- - - - -	76
2.25 Comparison between measured velocities in 2C4 grout at a range of 1.90 cm and a calculation using the RDD constitutive models without shear modulus reduction due to damage, $\delta$ equal to 0.6 $\mu$ sec and $V_c$ corresponding to 1.0 Kb peak pressure- - - - -	77
2.26 Comparison between measured velocities in 2C4 grout at a range of 2.54 cm and a calculation using the RDD constitutive models without shear modulus reduction due to damage, $\delta$ equal to 0.6 $\mu$ sec and $V_c$ corresponding to 1.0 Kb peak pressure- - - - -	78
2.27 Comparison between measured velocities in 2C4 grout at a range of 4.0 cm and a calculation using the RDD constitutive models without shear modulus reduction due to damage, $\delta$ equal to 0.6 $\mu$ sec and $V_c$ corresponding to 1.0 Kb peak pressure- - - - -	79

# LIST OF ILLUSTRATIONS (Continued)

<u>Figure</u>	<u>Page</u>
3.1 Comparison between measured velocities in 2C4 grout and effective stress law simulation at 1.90 cm - - - - -	85
3.2 Comparison between measured velocities in 2C4 grout and effective stress law calculation at 1.90 cm (no pore pressure buildup on loading)- - - - -	86
3.3 Comparison between measured velocities in 2C4 grout and best fit effective stress law calculation at 1.90 cm (no pore pressure buildup on loading)- - - - -	87
3.4 Comparison between measured velocities in 2C4 grout and best fit effective stress law calculation at 1.27 cm- - - - -	88
3.5 Comparison between measured velocities in 2C4 grout and best fit effective stress law calculation at 2.54 cm- - - - -	89
3.6 Comparison between measured velocities in 2C4 grout and best fit effective stress law calculation at 4.0 cm- - - - -	90
3.7 Calculated residual stress in 2C4 grout at 80 $\mu$ sec using effective stress model- - - - -	92
3.8 Predicted particle velocities at 8.0 cm for the proposed 3 gm charge test in 2C4 grout using the RDD models together with the measured velocities from the standard tests scaled to 3 gm- -	95
3.9 Predicted particle velocities at 5.08 cm for the proposed 3 gm charge test in 2C4 grout using the RDD models together with the measured velocities from the standard tests scaled to 3 gm- -	96
3.10 Predicted particle velocities at 3.80 cm for the proposed 3 gm charge test in 2C4 grout using the RDD models together with the measured velocities from the standard tests scaled to 3 gm- -	97
3.11 Predicted particle velocities at 2.54 cm for the proposed 3 gm charge test in 2C4 grout using the RDD models together with the measured velocities from the standard tests scaled to 3 gm- -	98
3.12 Calculated particle velocities at 2.54 cm for the proposed 3 gm charge in 2C4 grout using the RDD constitutive models with scaled material properties. Measured velocities from the standard 3/8 gm tests are shown scaled to 3 gms for comparison- - - - -	100
3.13 Calculated particle velocities at 3.80 cm for the proposed 3 gm charge in 2C4 grout using the RDD constitutive models with scaled material properties. Measured velocities from the standard 3/8 gm tests are shown scaled to 3 gms for comparison- -	101

# LIST OF ILLUSTRATIONS (Continued)

<u>Figure</u>	<u>Page</u>
3.14 Calculated particle velocities at 5.08 cm for the proposed 3 gm charge in 2C4 grout using the RDD constitutive models with scaled material properties. Measured velocities from the standard 3/8 gm tests are shown scaled to 3 gms for comparison- - - - -	102
3.15 Calculated particle velocities at 8.0 cm for the proposed 3 gm charge in 2C4 grout using the RDD constitutive models with scaled material properties. Measured velocities from the standard 3/8 gm tests are shown scaled to 3 gms for comparison- - - - -	103
3.16 Calculated particle velocities at 3.80 cm for the 3 gm charge in 2C4 grout using the RDD constitutive models with scaled material properties and the same lucite thickness as the standard 3/8 gm tests - - - - -	104
3.17 Calculated particle velocities at 3.80 cm for the 3 gm charge in 2C4 grout using the RDD constitutive models and the same lucite thickness as the standard 3/8 gm tests- - - - -	106
4.1 Comparison between measured particle velocities at 1.27 cm in LD2C4 grout and a calculation using the RDD constitutive models and the measured crush curve- - - - -	115
4.2 Comparison between measured particle velocities at 1.90 cm in LD2C4 grout and a calculation using the RDD constitutive models and the measured crush curve- - - - -	116
4.3 Comparison between measured particle velocities at 2.54 cm in LD2C4 grout and a calculation using the RDD constitutive models and the measured crush curve- - - - -	117
4.4 Comparison between measured particle velocities at 4.0 cm in LD2C4 grout and a calculation using the RDD constitutive models and the measured crush curve- - - - -	118
4.5 Comparison between measured particle velocities at 2.54 cm in LD2C4 grout and a calculation using the RDD constitutive models and "best fit" crush curve (Table 4.2) with 20 percent higher values of strain rate coefficients $f_1$ and $f_3$ .- - - - -	120
4.6 Comparison between measured particle velocities at 2.54 cm in LD2C4 grout and a calculation using the RDD constitutive models showing the effect of reducing the pressure from 0.40 Kb to 0.35 Kb at point 10 of Table 4.2- - - - -	122
4.7 Comparison between measured velocities at 2.54 cm in LD2C4 grout and a calculation using the RDD constitutive models showing the effect of increasing the pressure from 0.21 to 0.22 Kb at point 11 from the calculation of Figure 4.6- - - - -	123

# LIST OF ILLUSTRATIONS (Continued)

<u>Figure</u>	<u>Page</u>
4.8 Comparison between measured velocities at 2.54 cm in LD2C4 grout and a calculation showing the effect of increasing the pressure at point 11 to 0.25 Kb for slightly different material properties- - - - -	124
4.9 Comparison between measured velocities at 2.54 cm in LD2C4 grout and a calculation using the RDD constitutive models showing the effect of decreasing the pressure from 0.21 to 0.20 Kb at point 11 from the calculation of Figure 4.6- - - - -	125
4.10 Comparison between measured velocities at 2.54 cm in LD2C4 grout and a calculation using the RDD constitutive models showing the effect of increasing the specific volume from 0.518 to 0.519 cc/gm at point 11 from the calculation of Figure 4.9- - - - -	127
4.11 Comparison between measured particle velocities at 1.27 cm in LD2C4 grout and the velocities calculated using the measured crush curve (Table 4.2) and the effective stress model for the first time- - - - -	129
4.12 Comparison between measured particle velocities at 1.90 cm in LD2C4 grout and the velocities calculated using the measured crush curve (Table 4.2) and the effective stress model for the first time- - - - -	130
4.13 Comparison between measured particle velocities at 2.54 cm in LD2C4 grout and the velocities calculated using the measured crush curve (Table 4.2) and the effective stress model for the first time- - - - -	131
4.14 Comparison between measured particle velocities at 4.0 cm in LD2C4 grout and the velocities calculated using the measured crush curve (Table 4.2) and the effective stress model for the first time- - - - -	132
4.15 Comparison between measured particle velocities at 2.54 cm in LD2C4 grout and the velocities calculated by Cherry and Rimer (Reference 5) using the effective stress model- - - - -	133
4.16 Comparison between measured particle velocities at 1.27 cm for LD2C4 grout and "best fit" simulation using the effective stress model- - - - -	135
4.17 Comparison between measured particle velocities at 1.90 cm for LD2C4 grout and "best fit" simulation using the effective stress model- - - - -	136

# LIST OF ILLUSTRATIONS (Continued)

<u>Figure</u>	<u>Page</u>
4.18 Comparison between measured particle velocities at 2.54 cm for LD2C4 grout and "best fit" simulation using the effective stress model- - - - -	137
4.19 Comparison between measured particle velocities at 4.0 cm for LD2C4 grout and "best fit" simulation using the effective stress model- - - - -	138
4.20 Calculated residual stresses for LD2C4 grout at 85 $\mu$ sec using the effective stress model- - - - -	139

## LIST OF TABLES

<u>Table</u>	<u>Page</u>
2.1 C-J State and JWL Coefficients for PETN (1.0 gm/cc)- - - - -	31
2.2 Material properties for 2C4 grout- - - - -	35
4.1 Material properties for LD2C4 grout- - - - -	109
4.2 Crush Curves for LD2C4 grout- - - - -	114



## SECTION 1

### INTRODUCTION AND SUMMARY

As part of the DNA late-time containment program for underground nuclear testing, SRI International has since 1976 been conducting small scale laboratory experiments to study the residual stress fields around explosively formed cavities. The standard experiment involves casting a 12-inch diameter sphere of rock-matching grout (2C4) around a lucite-encased sphere of high explosive (3/8 gm of PETN), placing this grout sphere in a pressurized water tank to simulate overburden pressure, and detonating the PETN. While maintaining overburden pressure, the sphere is then hydrofractured from the explosively formed cavity using a tube emplaced preshot. Breakdown pressure is compared with breakdown pressure from a precast (unexploded) sphere to obtain an estimate of the magnitude of the explosively formed residual stress fields. A detailed description and discussion of the experimental results may be found in Cizek and Florence (References 1 and 2).

S-CUBED was asked to numerically simulate these experiments in order to increase understanding of the laboratory results, and to validate our capability to calculate containment related phenomena. Part of our calculational effort, the finite difference simulation of the high explosive detonation and the subsequent nonlinear dynamic processes which result in the formation of compressive residual stress fields in the grout surrounding the exploded cavity, has been reported by Rimer and Lie (References 3 and 4).

Before 1981, the only laboratory data available to be directly compared to the dynamic calculations consisted of final cavity radius and the pressure and integrated impulse at a quartz gauge emplaced in the bottom of the water tank. While cavity radius is an important discriminator of constitutive models and material properties, the quartz gauge data (See Table C.1 of Reference 2) may vary by 25 percent or more from individual shot to shot. Calculations have shown that variations

of 15 percent or more may be due to 1/8 inch tolerances in the radii of individual grout spheres or in locating the center of a grout sphere relative to the quartz gauge (See Reference 4).

In order to provide laboratory data which could be directly compared to the finite difference calculations, SRI began in 1981 to emplace particle velocity gauges inside the grout spheres. These gauges (see Reference 2) consist of concentric circular current-carrying loops of wire cast symmetrically about the charge. A magnetic field was generated normal to the plane of the loops by passing current through a coil which surrounds the sphere. Charge detonation produces radial motion of the loops that cut the magnetic flux lines. In accordance with Faraday's law, the voltage induced in each conducting loop is proportional to the particle velocity. Records of radial particle velocity vs time obtained from these gauges have proved to be reproducible from shot to shot.

The coil surrounding the sphere has necessitated a reduction in the diameter of the grout sphere from 12 to 11 inches and replacement of the confining water in the tank by a nonconducting oil. These modifications further increase the ambiguity of the quartz gauge measurements as a tool for code validation, but have been shown calculationally to not influence the residual stress fields or particle velocity records. The impact of another required experimental modification, replacement of the manganin bridge wire detonator by a mild detonating fuse (MFD), is difficult to quantify with our calculations.

In this report, we begin by discussing the successful numerical simulation of the SRI particle velocity records and final cavity radius from spheres of 204 rock matching grout. The comparisons between measured and calculated particle velocities are shown at four gauge locations (See Figures 1.1-1.4) and the calculated compressive residual stress fields in Figure 1.5.

PV2 273

R = 127 (CM)

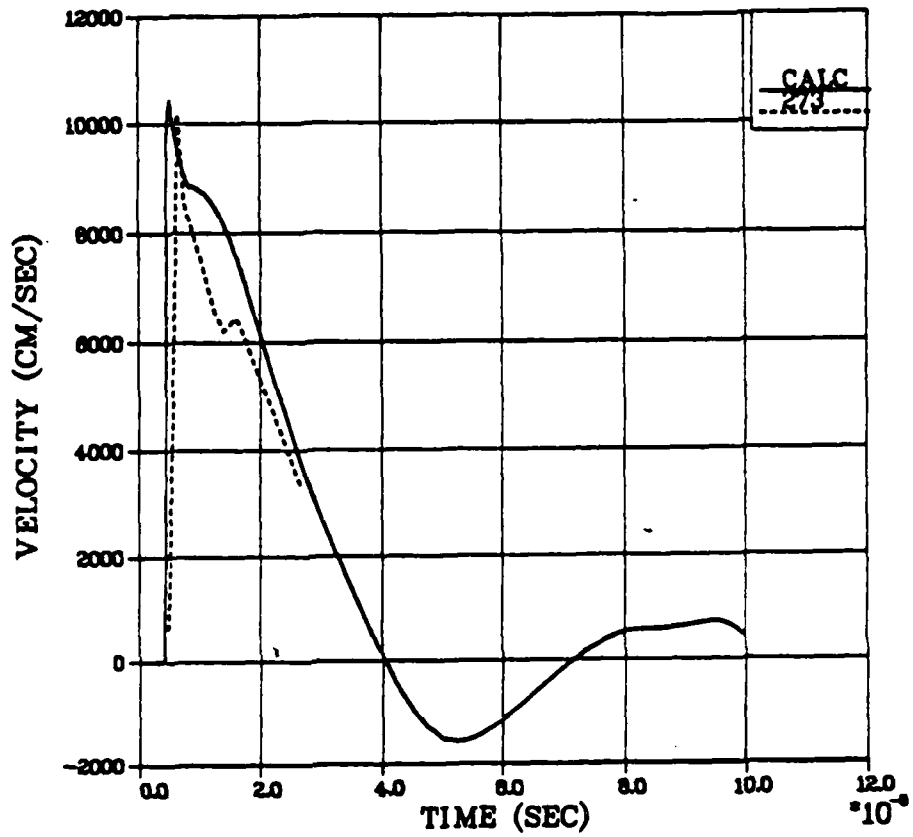


Figure 1.1. Comparison between measured and calculated particle velocities in 2C4 grout at a range of 1.27 cm.

PV3 272  
PV3 273

R = 1.90 (CM)

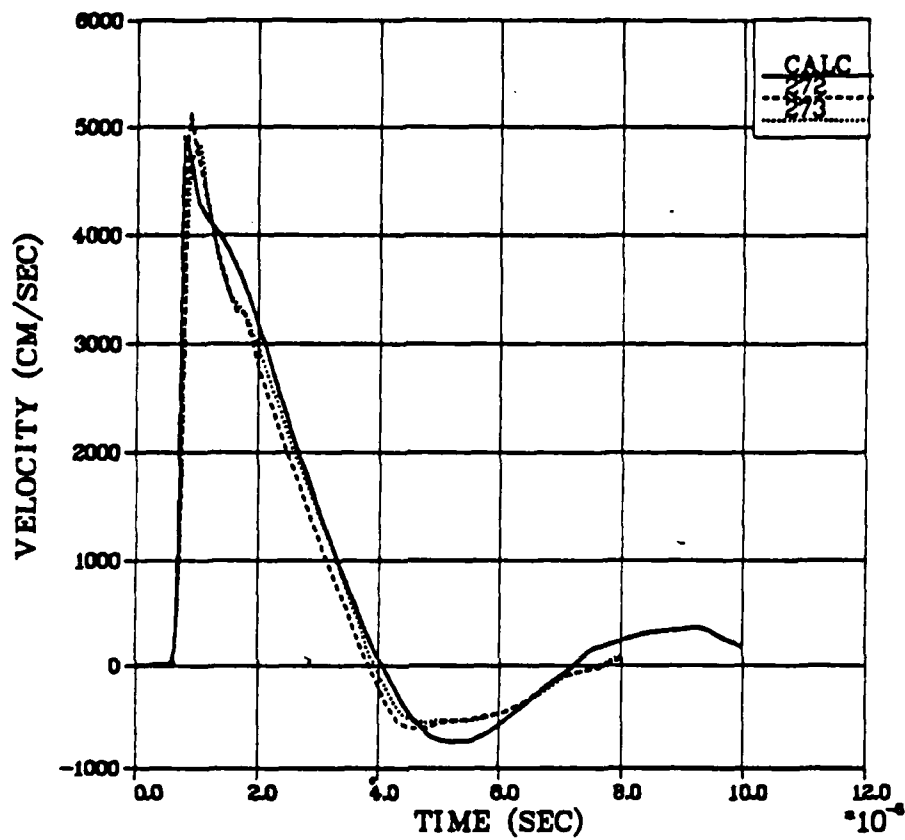


Figure 1.2. Comparison between measured and calculated particle velocities in 2C4 grout at a range of 1.90 cm.

PV 272  
PV 273

R = 2.54 (CM)

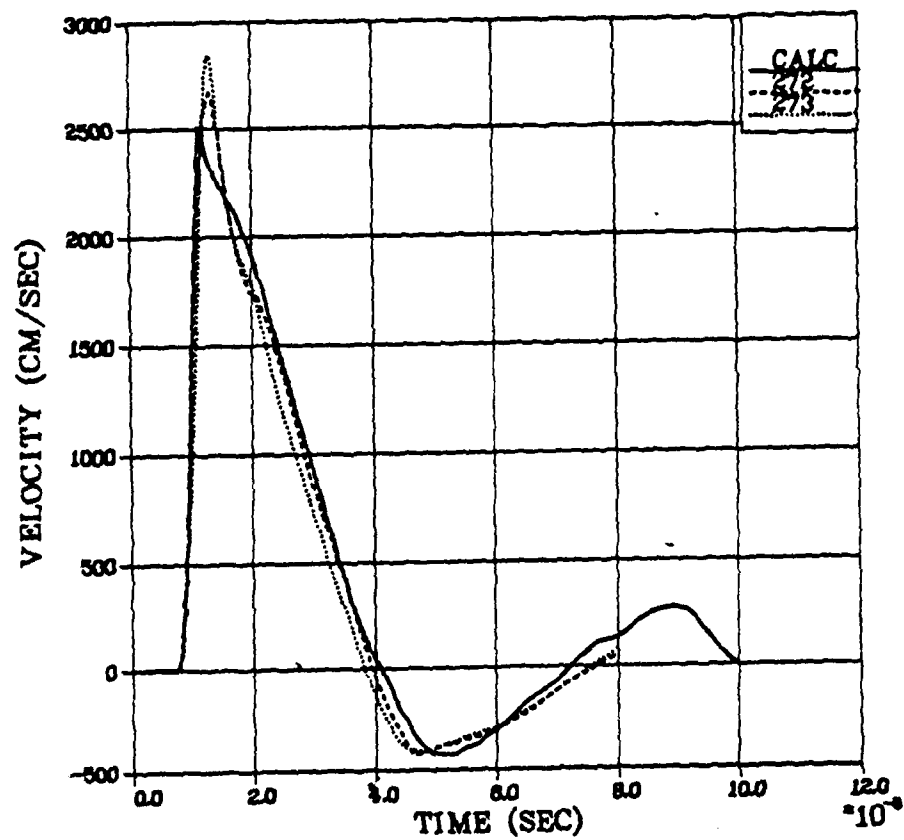


Figure 1.3. Comparison between measured and calculated particle velocities in 2C4 grout at a range of 2.54 cm.

PV5 272  
PV5 273

R = 4.00 (CM)

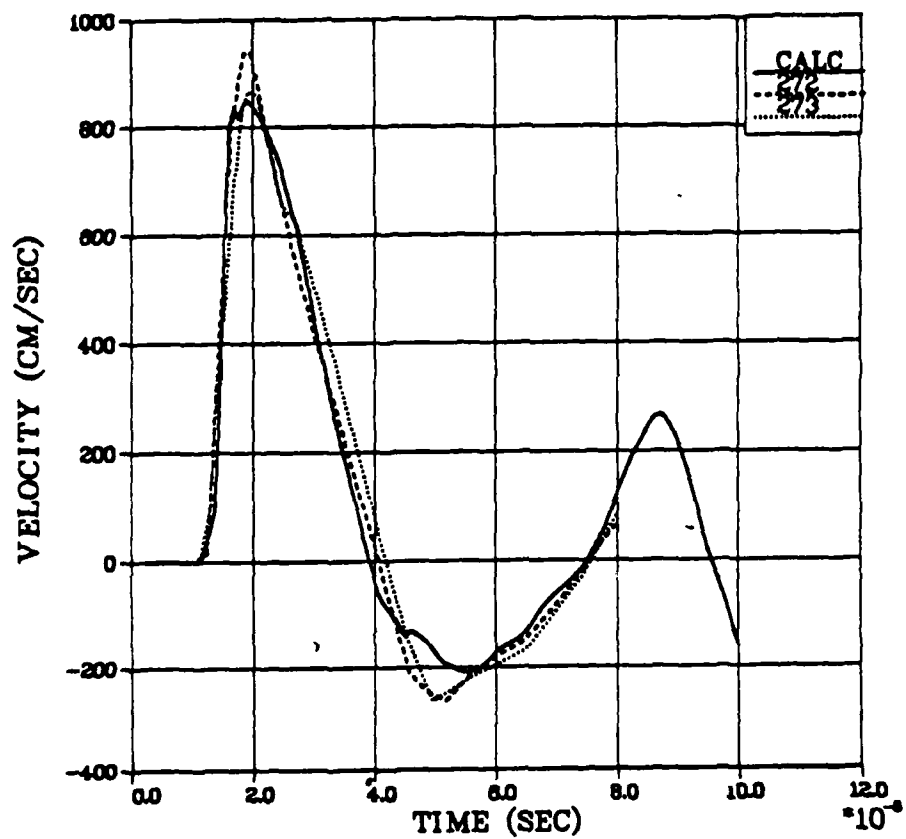


Figure 1.4. Comparison between measured and calculated particle velocities in 2C4 grout at a range of 4.0 cm.

# Skipper Stress Field 2C4

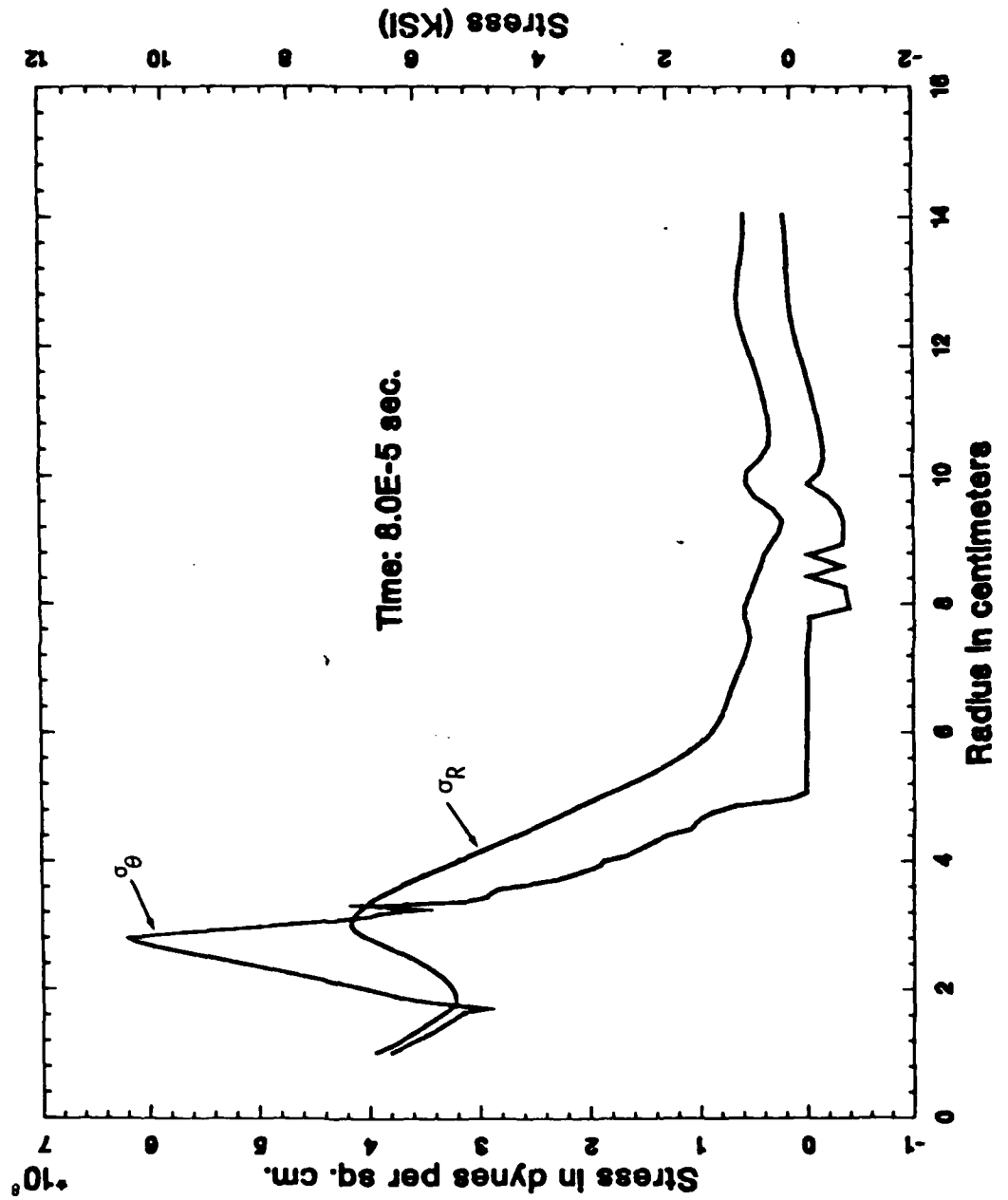


Figure 1.5. Calculated "residual" stresses for 2C4 grout at  $80 \mu s$ . Elastic waves generated at wall of water tank are still reverberating through computational grid.

The simple constitutive models used successfully in the past to predict peak stresses and velocities from nuclear events in saturated tuffs proved to be unsuited to the more difficult task of calculating full velocity records for these small scale experiments. (At this time, the particle velocity data from nuclear events in tuff are insufficient to validate any constitutive model.) In Section 2, we discuss in some detail the computational constitutive models used successfully to match the particle velocity records from 2C4 grout and summarize the other models which were tried including those which were partially successful and those which failed. The successful constitutive models include an increase in strength at high strain rates, a shear modulus reduction postshock, and a time dependent and damage dependent (Maxwell solid) relaxation of deviatoric stresses to a lower "shock damaged" failure surface. These models will be referred to collectively as the RDD model (for rate and damage dependent). Since the RDD models include rate dependent effects, results at one explosive yield do not simply scale to another yield.

In Section 3 of this report, an alternative approach, the effective stress law model, developed with DARPA support (see Cherry and Rimer, Reference 5), is shown to give excellent agreement with the velocity data without the use of rate dependent models. Figures 3.3-3.7 show these results. Thus, the particle velocity data, although greatly restricting our choice of constitutive models did not allow a unique specification of a constitutive model for the 2C4 grout. A purely experimental test of the importance of rate dependent effects in the SRI 2C4 tests is proposed. This test, using 3 gms of PETN instead of 3/8 gm (a factor of two lower strain rates), is shown computationally to distinguish between the two numerical models.

For 2C4 grout, the modeling effort was directed toward modifications of the constitutive models dealing with shear failure; i.e., rate effects, shock damage, and effective stress. The irreversible crush-up of air-filled porosity had been determined from static laboratory material property tests under uniaxial strain loading and unloading conditions. Details of the crush curve for this almost saturated material proved to



be relatively unimportant in matching the velocity pulses at the ranges of interest. These details would, of course, become increasingly more important at greater ranges where peak stress levels are lower.

Particle velocity measurements have recently been made at the gauge locations of Figures 1.1-1.4 for LD2C4 grout, a lower density, more porous grout, intended as an alluvium simulant, in which 13.4 percent air-filled porosity has been added in the form of microballoons (See Cizek and Florence, Reference 6). S-CUBED was asked by DNA to simulate numerically these particle velocity records using the RDD model before laboratory material properties data were made available. This exercise proved to be a successful demonstration that material properties could be determined from particle velocity records for earth materials such as alluvium from which core for laboratory tests is very difficult to obtain. At the ranges of interest, stress levels were much lower for the porous LD2C4 than for 2C4. Thus, the modeling effort became largely a backing out of a dynamic crush curve which would reproduce numerically the velocity records from the LD2C4 grout spheres experiments.

Figures 1.6-1.9 show the successful match between measured and calculated particle velocities for LD2C4 using the RDD model. Figure 1.10 gives the calculated residual stresses for LD2C4 grout which are approximately half of those calculated for 2C4 rock matching grout. (Figures 4.11-4.14 show the excellent agreements obtained using the effective stress model for LD2C4 grout).

Very recently, Terra Tek, Inc. (R. D. Smith, Reference 7) has made static load-unload measurements in uniaxial strain to determine a crush curve for LD2C4 grout. Figure 1.11 shows the excellent agreement between the laboratory measurements and the dynamic crush curve we had determined numerically from the velocity records before receiving this laboratory data. The only significant changes in calculated particle velocities using the laboratory measurements were 6 percent lower peak velocities in Figures 1.7 and 1.8.

PV2 287  
PV2 288

R = 1.27 (CM)

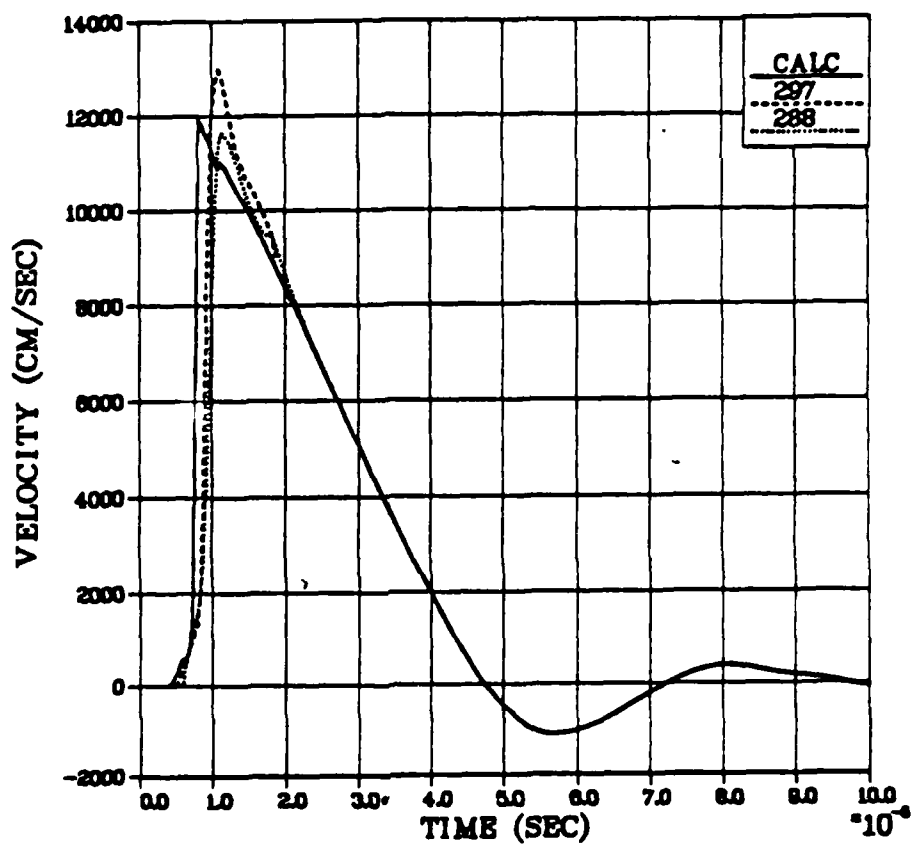


Figure 1.6. Comparison between measured and calculated particle velocities in LD2C4 grout at a range of 1.27 cm.

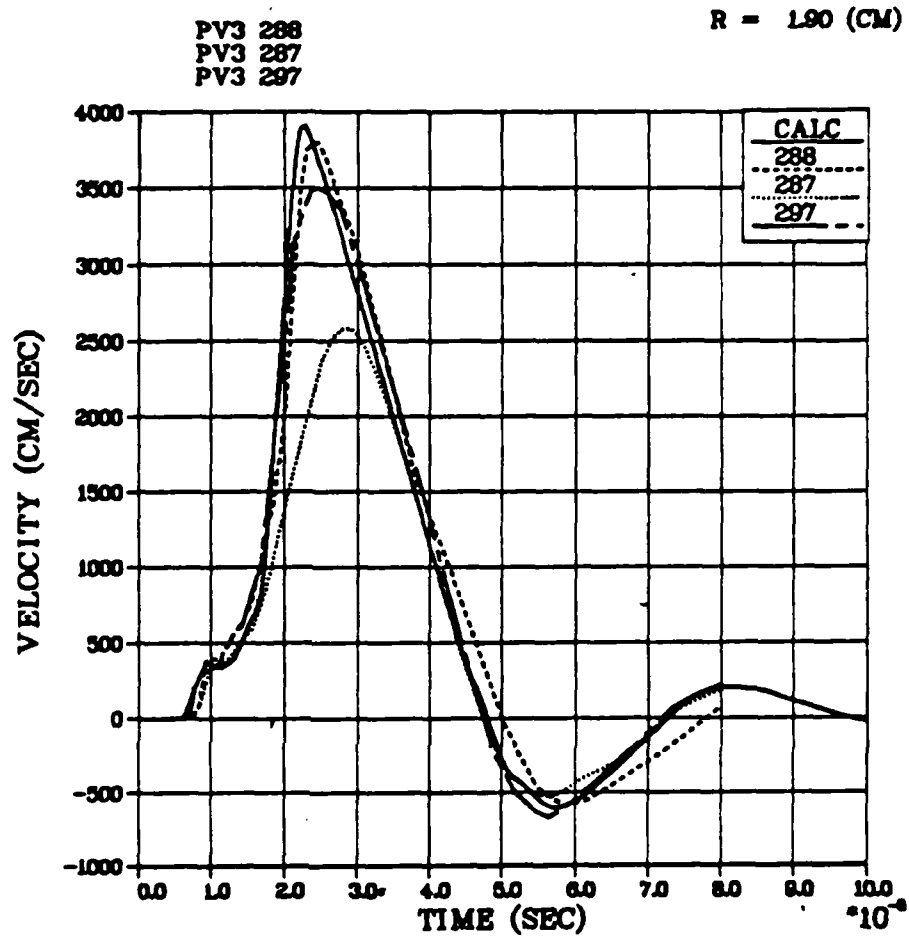


Figure 1.7. Comparison between measured and calculated particle velocities in LD2C4 grout at a range of 1.90 cm.

PW 288  
PW 297

R = 2.54 (CM)

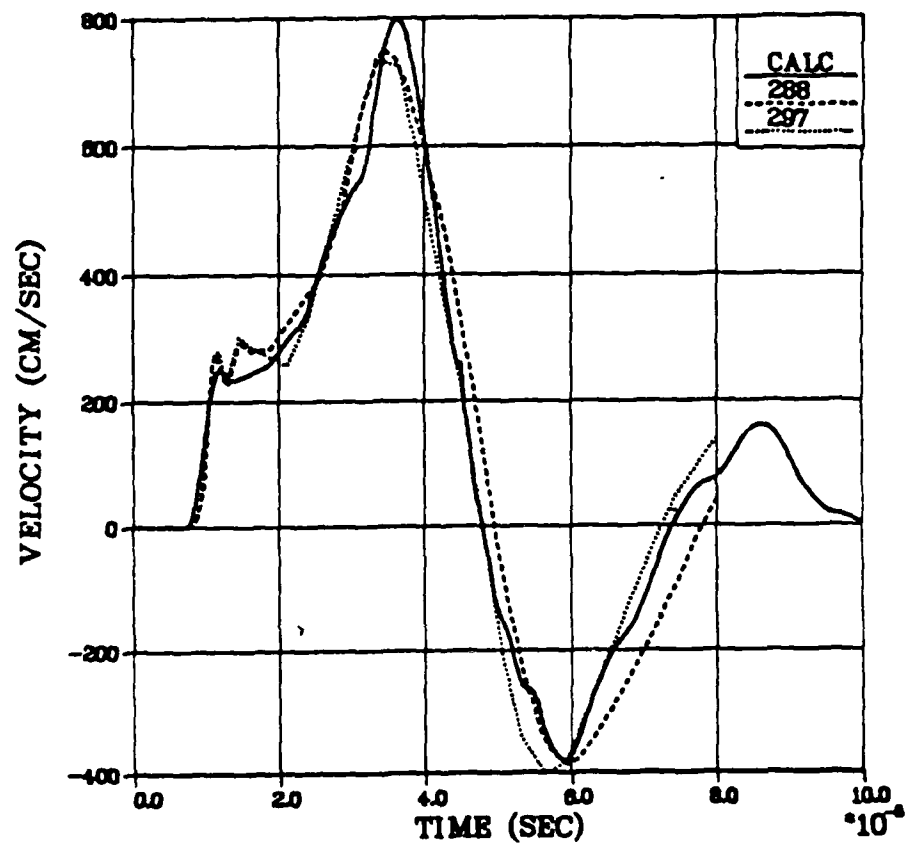


Figure 1.8. Comparison between measured and calculated particle velocities in LD2C4 grout at a range of 2.54 cm.

PV5 287  
PV5 297

R = 4.00 (CM)

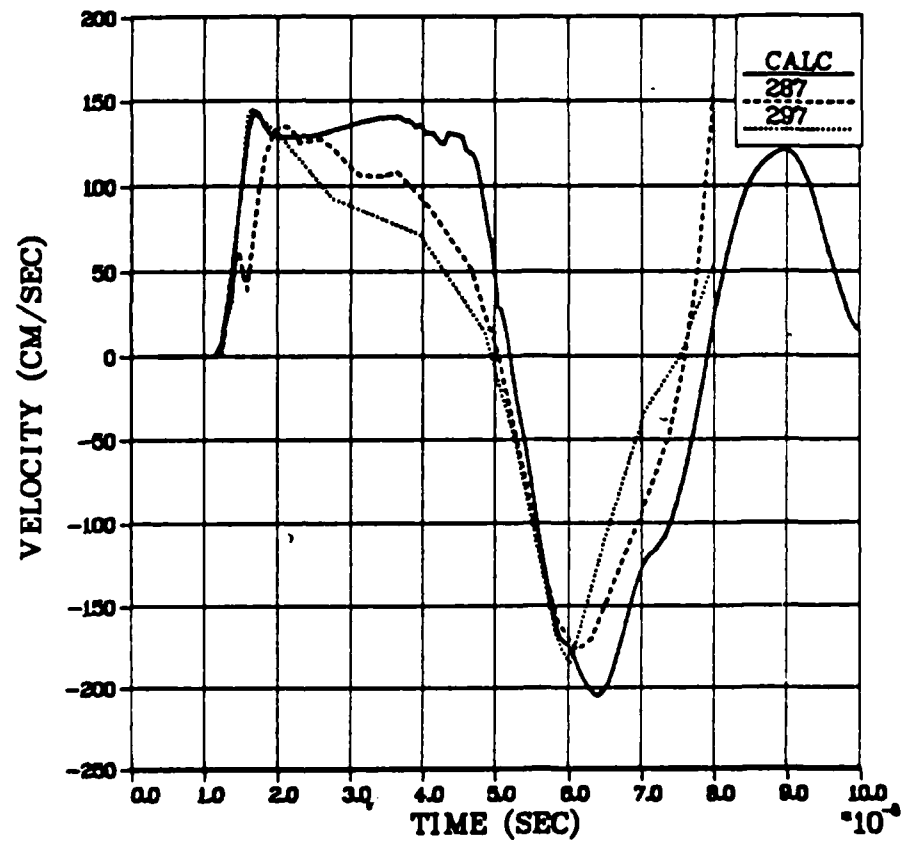


Figure 1.9. Comparison between measured and calculated particle velocities in LD2C4 grout at a range of 4.0 cm.

# Skipper Stress Field LD2C4

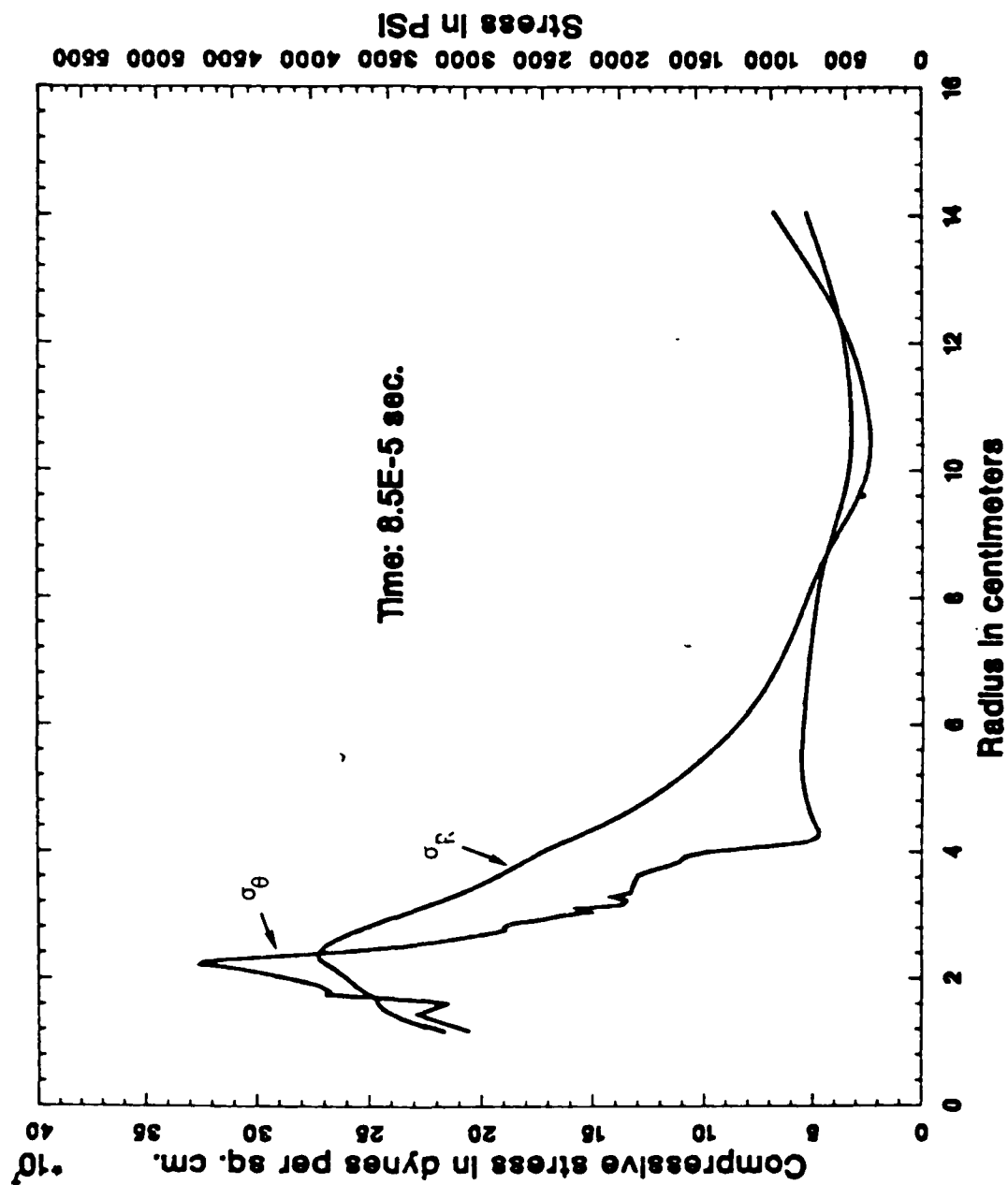


Figure 1.10. Calculated residual stresses for LD2C4 grout at 85  $\mu$ s.

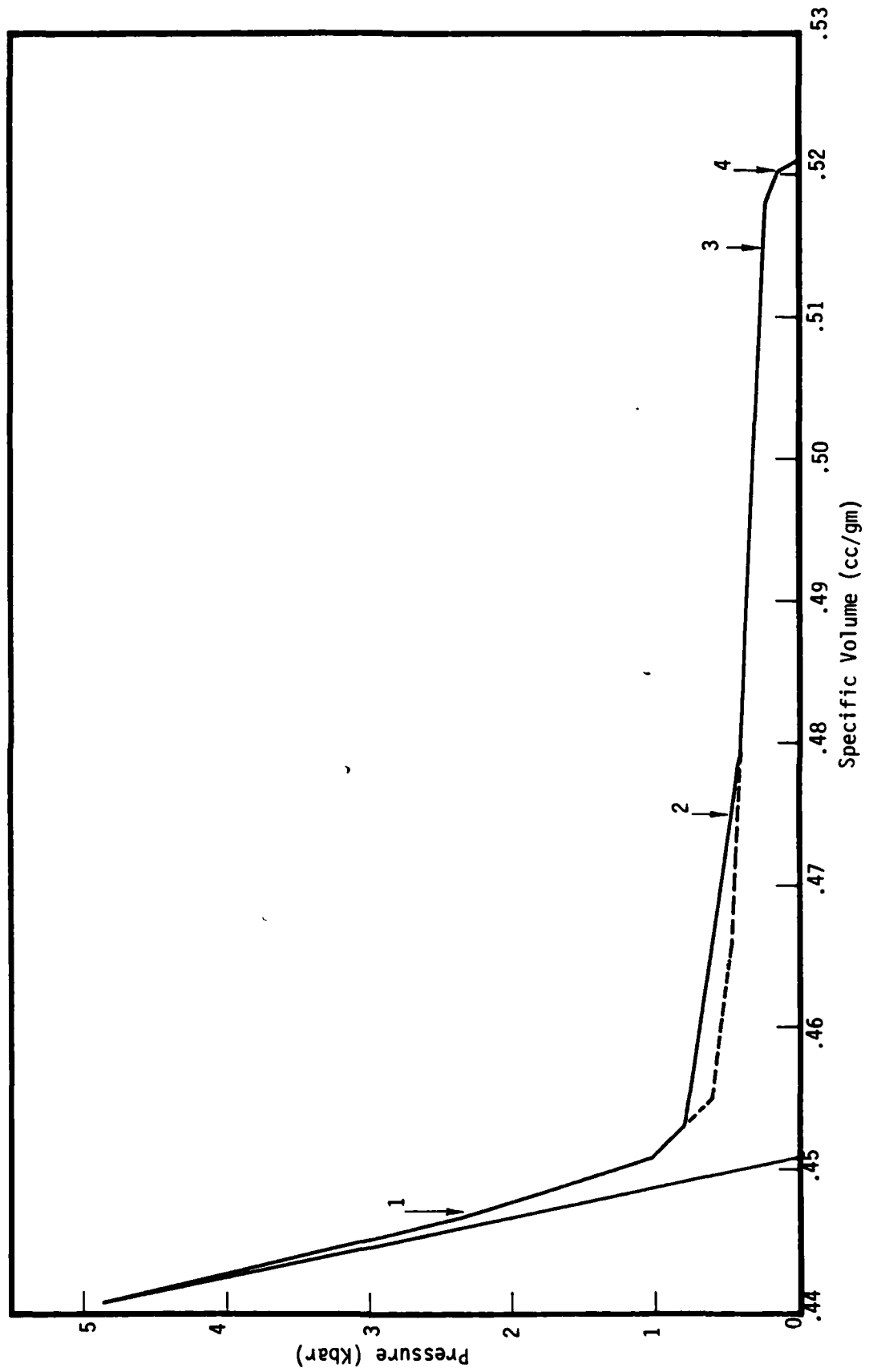


Figure 1.11. Crush curve for LD2C4 grout. The solid curve was developed for the RDD model calculation and the dotted curve represents the subsequent laboratory measurements. The arrows indicate the approximate loadings corresponding to the velocity peaks at the four gauges.

Section 4 of this report contains a detailed discussion of the modeling effort for LD2C4 grout, including the sensitivity of the calculated velocity records to the shape of the crush curve.

The results described in this report have a significance beyond the development and validation of constitutive models for the grouts used in the SRI experiments. The important results and conclusions are summarized as follows beginning with those most specific to the grout spheres experiments and ending with the most general.

1. A higher strength than obtained from static laboratory measurements is required to numerically match the measured cavity radii. This is accomplished either by using strain rate dependent strength increases as in the RDD model or by defining a dry strength of the grout as in the effective stress law model.

2. A considerably lower strength after passage of the shock wave is needed to match the velocity pulses, particularly the wide negative pulse. The strength reduction in the RDD model, i.e., shock damage or shock conditioning assumed a function of the amount of void crushup is made time dependent using a Maxwell solid in order to best reproduce the measured peak velocities at the high strain rates of the small scale experiment. These rate effects may not be important for large scale events. The effective stress model accomplishes a rate independent stress reduction from the dry strength to a lower wet strength which depends upon the pore fluid pressure, here made a function of the amount of void crushup. Thus, both models relate the strength reduction to the crush curve.

3. Compressive residual stress fields are calculated for both the 2C4 rock matching grout and the porous, low density LD2C4 grout using two models validated by excellent agreement with the measured velocities and cavity expansion. For 2C4 grout the magnitudes of both calculated residual stress fields are compatible with the hydrofracture records for these tests.



4. The hydrofracture records for LD2C4 grout show no increase in breakdown pressure for exploded spheres over unexploded (precast spheres). This experimental result appears not to be compatible with the calculated residual stress fields for LD2C4. Since LD2C4 is intended to be a simulant of a weak, high porosity rock such as alluvium, the experimental result brings into question the application of the residual stress concept to events in these earth materials. The experimental result may yet prove to be due to very rapid stress relaxation from the calculated residual stress fields. If such a rapid stress relaxation occurs in alluvium at the much larger scale of a nuclear test, residual stress fields may not prevent hydrofracture by the hot cavity gases from a nuclear event.

5. Particle velocity and cavity radius measurements from the SRI small scale experiments have been shown to provide severe constraints on the choice of equation of state models for grout. Measurements of rock response in these simple, uncontroversial geometries may provide us the standards by which we can measure our modeling success for the rocks of interest to containment. We recognize the objections to application of the results of these very small scale tests to insitu events (size effects, rate effects, insitu stresses), but despair of obtaining cheap, reproducible/reliable and frequent experimental data from nuclear tests to adequately verify our calculational models. As a first step, particle velocity measurements will be obtained at SRI from cores of tuff taken from the site of the upcoming Sandia National Laboratory ONE TON high explosive test in G-tunnel. These velocity measurements on representative cores of tuff (determined using laboratory material properties measurements) will be compared with velocity data from the ONE TON event to determine size effects, etc. Calculational models calibrated with the SRI tuff measurements will be applied to the ONE TON results.

6. As demonstrated for the LD2C4 experiments, particle velocity measurements, together with cavity radius data, can be used in conjunction with appropriate constitutive models to determine material properties for earth materials from which core is not available. Insitu particle velocity measurements from high explosive tests are recommended as material properties tests in these media. The CIST test is such a test for near surface cylindrical geometries. For contained nuclear test beds, however, we recommend spherically symmetric explosive tests which lead to less expensive one-dimensional simulations.

## SECTION 2.

### CONSTITUTIVE MODELS FOR 2C4 ROCK-MATCHING GROUT

Here, we discuss the computational constitutive models and material properties used to simulate the particle velocity data from the SRI small scale explosive tests in 2C4 rock-matching grout. We begin with a discussion of the "source", i.e., characterization of the PETN explosive and the surrounding lucite shell. These are followed by a summary of the significant laboratory material properties measurements for 2C4 grout. The discussion of grout constitutive models is presented in roughly the chronological order in which they were employed in this investigation. Included are those models which failed to match the data and those which were partially successful so that future calculators may avoid duplicating our less successful investigations.

#### 2.1 CHARACTERIZATION OF THE PETN EXPLOSIVE

The JWL equation of state (see Reference 8) was developed at Lawrence Livermore National Laboratory to describe the pressure-volume-energy behavior of explosive detonation products. The pressure  $P(\text{Mb})$  is given as a function of internal energy  $E(\text{Mb cc/cc})$  and  $V$ , the ratio of volume of detonation products to undetonated explosive volume, by

$$P = A(1 - \frac{w}{R_1 V}) e^{-R_1 V} + B(1 - \frac{w}{R_2 V}) e^{-R_2 V} + \frac{wE}{V}$$

The equation for  $P$  as a function of  $V$  at constant entropy, i.e., the isentrope, is

$$P_s = Ae^{-R_1 V} + Be^{-R_2 V} + CV^{-(w+1)}$$

where  $A$ ,  $B$ ,  $C$ ,  $R_1$ ,  $R_2$  and  $w$  are coefficients determined for a limited number of explosives by matching the equation with experimental C-J conditions, calorimetric data, and expansion behavior -

generally cylinder tests. These coefficients have been estimated for explosives where data is not available.

In the absence of calorimetric data for the PETN density of interest (1.0 gm/cc) Finger (Reference 9) has calculated the coefficients given in Table 2.1 from the measured C-J pressure and detonation velocity (D). We calculated a revised set of JWL coefficients, also given in Table 2.1, which also reproduce the measured detonation velocity and C-J pressure in order to investigate the effects of HE equation of state variations. The revised coefficients gave smaller calculated peak particle velocities which are in better agreement with the grout spheres measurements (shown in Figure 2.1) within one final cavity radius (1.0 cm) of the explosive. (The "x" in Figure 2.1 denotes earlier, not as reliable, measurements made in cylinders of grout). With the revised JWL coefficients, used for all simulations shown in this report, calculated velocity pulse widths in the grout are also slightly smaller than for the original coefficients.

At ranges greater than 1 cm, almost no changes in results from a full HE detonation calculation occurred when the PETN was assumed to burn at constant volume and then to follow the JWL equation of state isentrope (given by  $P_s$ ) down in pressure from the initial volume. Since the latter procedure results in considerable savings in time and money compared to a full detonation calculation, it was used in all of the simulations discussed in this report.

## 2.2 EQUATION OF STATE FOR THE LUCITE SHELL

Fortunately, details of the lucite equation of state were found not to impact the simulations to first order. However, simulations of decoupled explosives in the SRI grout spheres are likely to be more sensitive to these details. The pressure-volume equation of state used to describe the lucite shell was developed by Duff (Reference 10) for the K0 code at Lawrence Livermore Laboratory. It fits shock velocity-particle velocity data to a straight line of the form

$$U_s = C_B + s U_p$$

TABLE 2.1. C-J STATE AND JWL COEFFICIENTS FOR PETN (1.0 gm/cc)

		<u>Finger</u>	<u>"Revised"</u>
$P_{cj}$	(Mb)	0.085	
D	(cm/ $\mu$ s)	0.555	
$E_0$	(Mb cc/cc)	0.057	
$V_{cj}$	(cc/gm)	0.724	
A	(Mb)	2.372	7.38
B	(Mb)'	0.1061	0.10
C	(Mb)	0.01008	0.00994
$R_1$		5.6	7.0
$R_2$		1.8	2.0
w		0.24	0.28

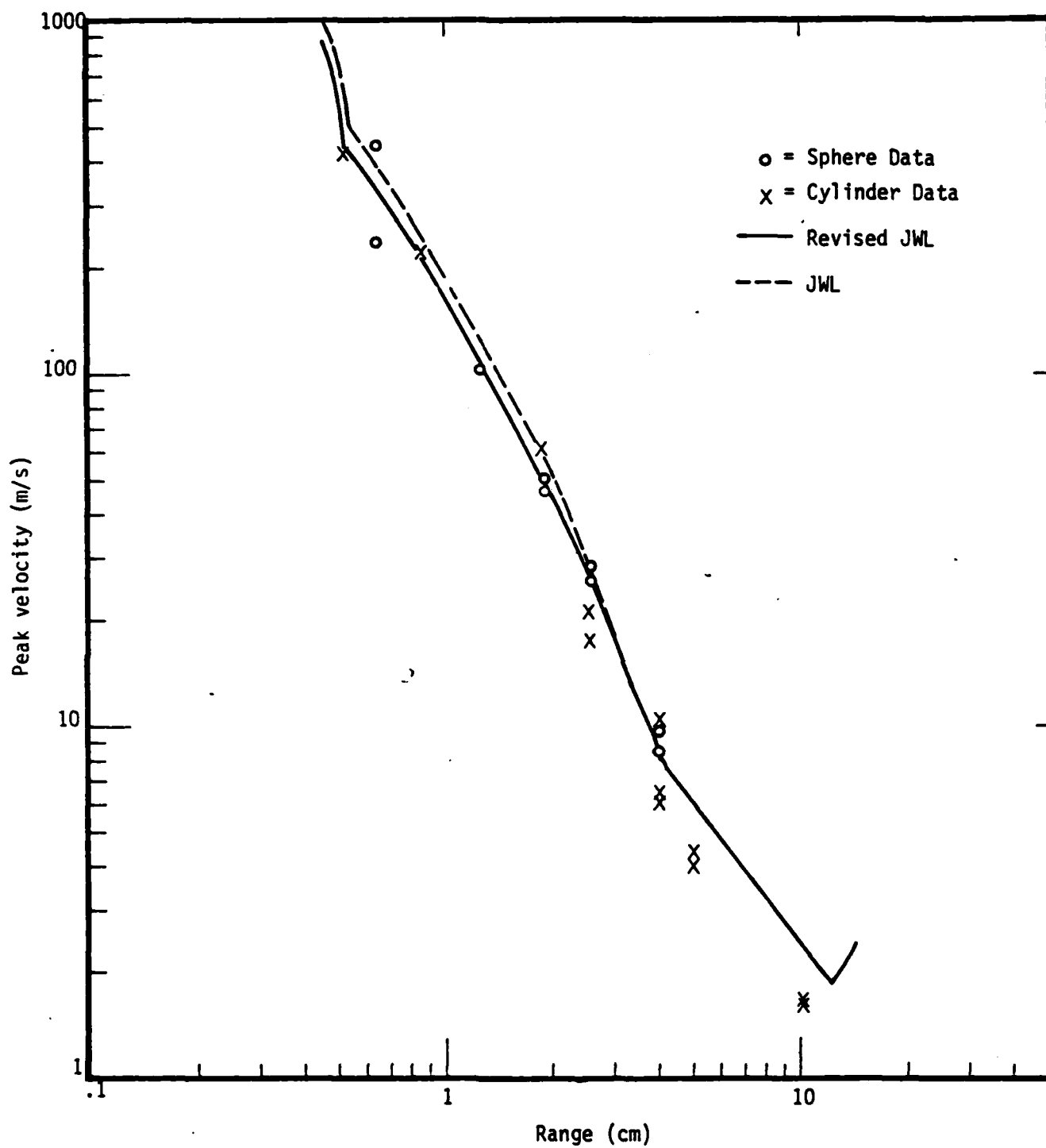


Figure 2.1. Peak velocity vs. range for 2C4 grout.

where  $U_s$  is the shock velocity,  $U_p$  the particle velocity, and  $C_B$  and  $s$  coefficients of the fit for lucite given as

$$C_B = 0.206 \text{ cm}/\mu\text{s}$$

$$s = 1.545$$

The pressure is calculated from

$$p = \rho_0 C_B^2 \mu \left[ 1 + \left( \frac{2s-1}{2} \right) \mu + s(s-1) \mu^2 \right]$$

where  $\mu = \rho/\rho_0 - 1$

and  $\rho_0 = 1.18 \text{ gm/cc.}$

The lucite was assumed to have a shear modulus of 18 Kb and to have a failure surface given by

$$Y = 0.682 + 0.9 \bar{P} \quad (\text{Kb}) \quad \bar{P} \leq 0.62$$

$$Y = 1.052 + 0.3 \bar{P} \quad (\text{Kb}) \quad 0.62 < \bar{P} < 6.5$$

$$Y = 3.0 \quad (\text{Kb}) \quad \bar{P} > 6.5 \text{ Kb}$$

where  $y$  is the maximum allowable stress difference and  $\bar{P}$  is the average of the maximum and minimum principal stresses.

### 2.3 MATERIAL PROPERTIES FOR 2C4 ROCK MATCHING GROUT

The rock-matching grout known as 2C4 replaced the more variable 2C3 grout as the host material for the SRI small scale experiments in 1977. Cyzek and Florence (Reference 11) reported static unconfined

compressive strength and physical properties measurements made at SRI as well as the results of static uniaxial strain load-unload tests to 4 Kb confining pressure performed at Terra Tek, Inc. Ultrasonic measurements of longitudinal and shear velocity and static tensile strength measurements (Brazil test) are first reported in Reference 12. Reference 13 reported dynamic measurements at SRI (at an average strain rate of  $0.15 \text{ sec}^{-1}$ ) which were significantly higher than the static measurements. Increases in strength of 30 to 50 percent above static measurements at strain rates of  $2\text{--}8 \text{ sec}^{-1}$  were later reported by Ehrgott (Reference 14) for a stronger grout intended to be 2C4. More recently, an extensive laboratory material properties program was conducted by Terra Tek for DNA (See Cooley, et al, Reference 15) which included uniaxial and hydrostatic compressive tests, strain rate tests, pore pressure tests (drained, undrained, etc), permeability measurements, and triaxial compression tests on virgin samples and on grout samples previously loaded to 4 Kb confining pressure in uniaxial strain and then unloaded.

Table 2.2 gives the physical properties and elastic wave speeds for 2C4 grout obtained from the above laboratory measurements and used in the calculations. Also shown are the compressive and tensile strengths measured under static loading and at an average strain rate of  $0.15 \text{ sec}^{-1}$ .

It is difficult to separate a discussion of material properties from the constitutive models used in the calculations. Let us review the basic constitutive models (used in the DNA containment community to model NTS Area 12 tuff) which were first applied to the grout spheres. These include a pressure-volume equation of state and constitutive models for shear and tension failure.

#### P-V Equation of State and Pore Crushup

The nominally saturated 2C4 grout was shown in Reference 15 to have approximately 1.5 percent air-filled porosity which was fully crushed up under uniaxial strain loading at approximately 3 Kb. The



TABLE 2.2. MATERIAL PROPERTIES FOR 2C4 GROUT

Density	(gm/cc)	2.205
Air-filled porosity	( % )	1.5
Bulk modulus	(Kb)	148.27
Shear modulus	(Kb)	70.78
Longitudinal wave speed	(m/s)	3317
Shear wave speed	(m/s)	1792
Poisson's ratio	-	0.294
Maximum stress difference	(Kb)	0.30
Unconfined compressive strength	(Kb)	
Static		0.270 ± 0.03
At strain rate of 0.15 sec <sup>-1</sup>		0.367
Tensile strength from Brazil Test (Kb)		
Static		0.036 ± 0.01
At strain rate of 0.15 sec <sup>-1</sup>		0.061

P- $\alpha$  porous rock crushup model, Reference 16, together with a polynomial equation of state were used to describe the P - V behavior of a rock element. The pressure of the material without air-filled voids is given by

$$P_n = 202 \mu + 288 \mu^2 \quad (\text{Kb})$$

where the coefficients were fit to the uniaxial load-unload data. Earlier calculations using the energy dependent Tillotson equation of state (Reference 17) showed no significant difference in results, probably due to the low C-J pressure of the HE.

For a material containing air-filled voids the pressure may be obtained from  $P_n$  through the use of the P- $\alpha$  crush model. The distension ratio  $\alpha$  is defined as the ratio of the density of the material without voids to its density with voids included. Thus as the grout is loaded,  $\alpha$  decreases from its initial value  $(1 - \phi_0)^{-1}$ , where  $\phi_0$  is the air-filled porosity (1.5 percent), down to 1.0 at 3 Kb, the pressure at which all air-filled porosity is irreversibly removed. Over the early portion of the loading (the linearly elastic portion) which is assumed here to extend up to 100 bars, the porosity is assumed to be completely recoverable upon unloading. Between 100 bars and 3 Kb, the air-filled porosity is assumed to be partially recoverable on unloading.

Figure 2.2 shows the load-unload curve based on the measurements in Reference 15. The elastic limit of 100 bars was chosen, somewhat arbitrarily, to be greater than the applied overburden pressure of 69 bars in the water tank. We found that for the four ranges of the grout spheres particle velocity data, the results were independent of the choice of elastic limit. However, the peak velocities at the larger ranges from the grout cylinder tests could be better simulated by assuming more void crushup below a stress of 0.5 Kb than given by the laboratory uniaxial strain load-unload data of Reference 15.

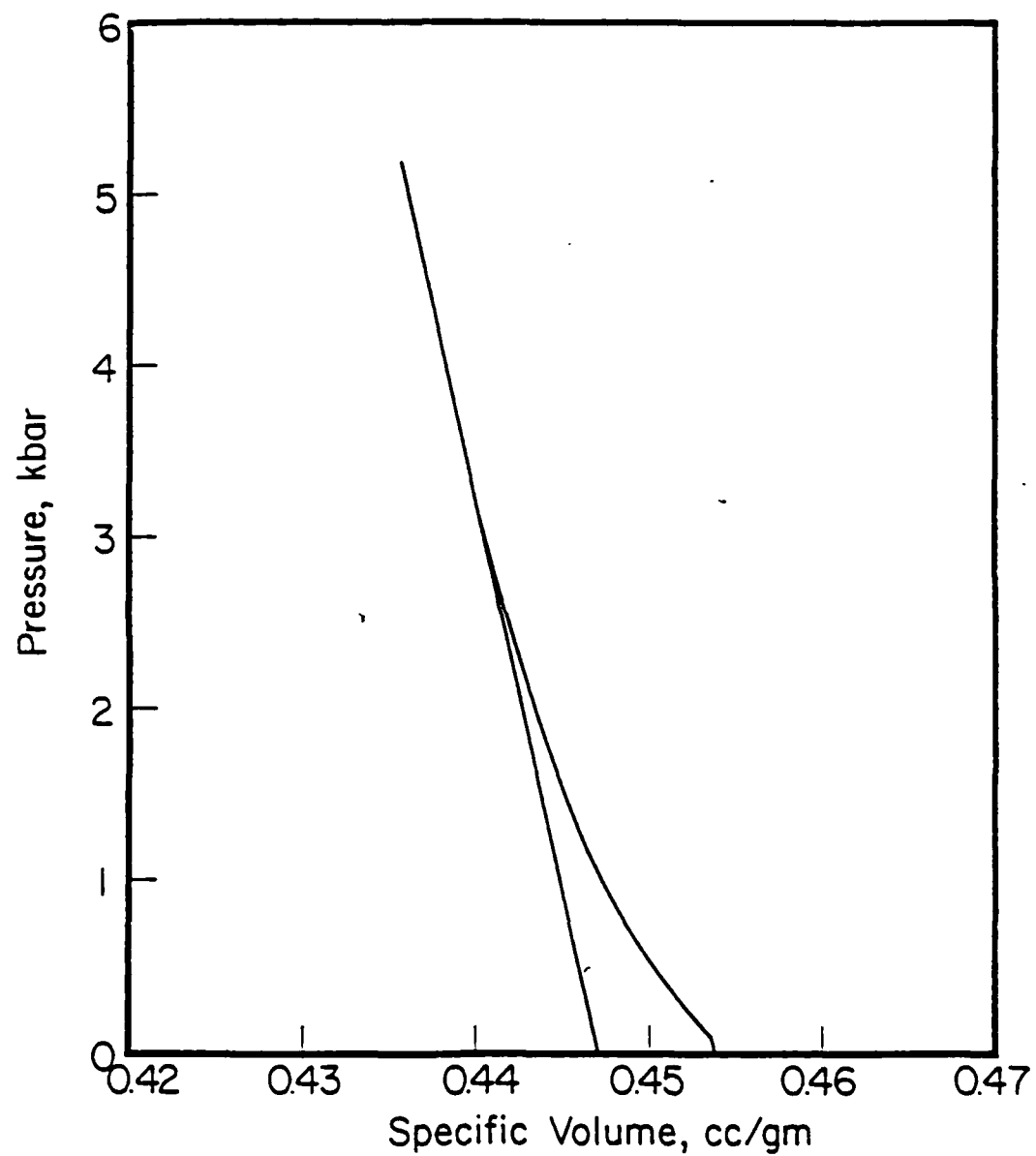


Figure 2.2. Crush curve for 2C4 grout.

### Shear and Tension Failure

As described in Reference 16, the material strength  $Y$  (the maximum stress difference) is chosen to be a function of  $\bar{P}$ , in spherical symmetry the average of the maximum and minimum principal stresses. This empirical formulation allows data from laboratory tests in compression (shear), extension, and torsion to be represented by a single failure surface. The laboratory static triaxial compression data for 2C4 grout has been plotted in  $Y$  vs  $\bar{P}$  space in Figure 2.3. (Figure 2.4 shows the raw data for each confining pressure.) Two types of data are shown; damaged, referring to grout samples which have been cycled in uniaxial strain to 4 Kb before testing, and intact, i.e., test results from virgin grout samples. These tests define a maximum static strength of 0.30 Kb for virgin 2C4 grout and a maximum "damaged" strength of 0.18 Kb for samples in which the air-filled porosity has been completely crushed up. No data is available for partially crushed samples.

The failure surface for intact grout (below maximum strength) was chosen as a straight line in  $\bar{P}$  space, shown in Figure 2.3 and given by

$$Y = 0.055 + 1.6 \bar{P} \quad (\text{Kb})$$

This failure surface is based on the measured static unconfined compressive strength of 0.275 Kb (at  $Y = 2 \bar{P}$ ) and also gives shear failure under extensional loading at stress levels corresponding to the measured tensile strengths given in Table 2.2.

Computationally, Hooke's law is used to obtain an initial estimate of the stress deviators. Shear failure occurs if the stress difference exceeds the failure surface. Then, adjustment of the stress deviators is required. In this simple constitutional model, each deviatoric stress component is reduced by multiplying it by the factor  $f_L$  given by

$$f_L = \frac{Y + \frac{b}{2} \left( \frac{J_3}{-2} \right)^{1/3}}{\sqrt{3} J_2 + \frac{b}{2} \left( \frac{J_3}{-2} \right)^{1/3}}$$

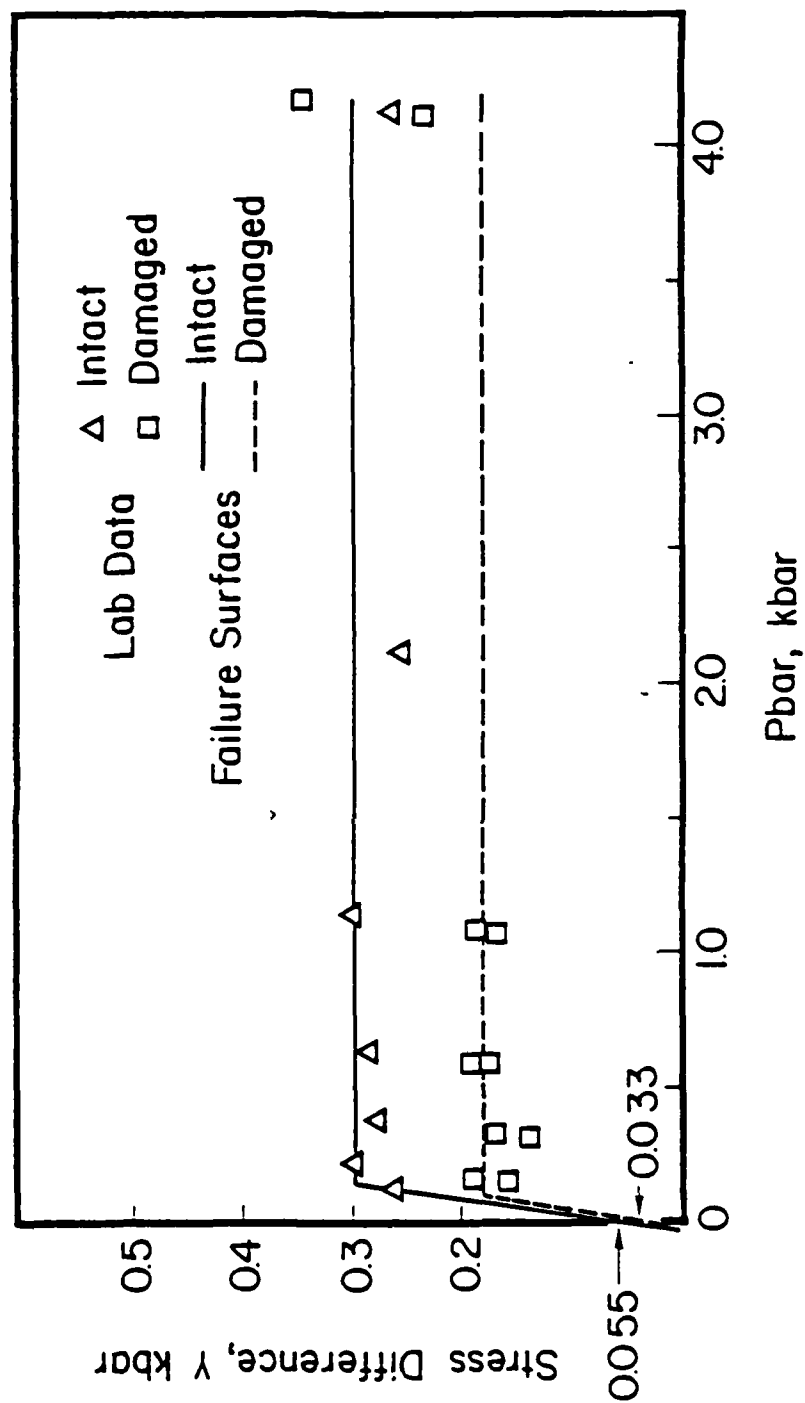


Figure 2.3. Failure surfaces for 204 rock matching grout.

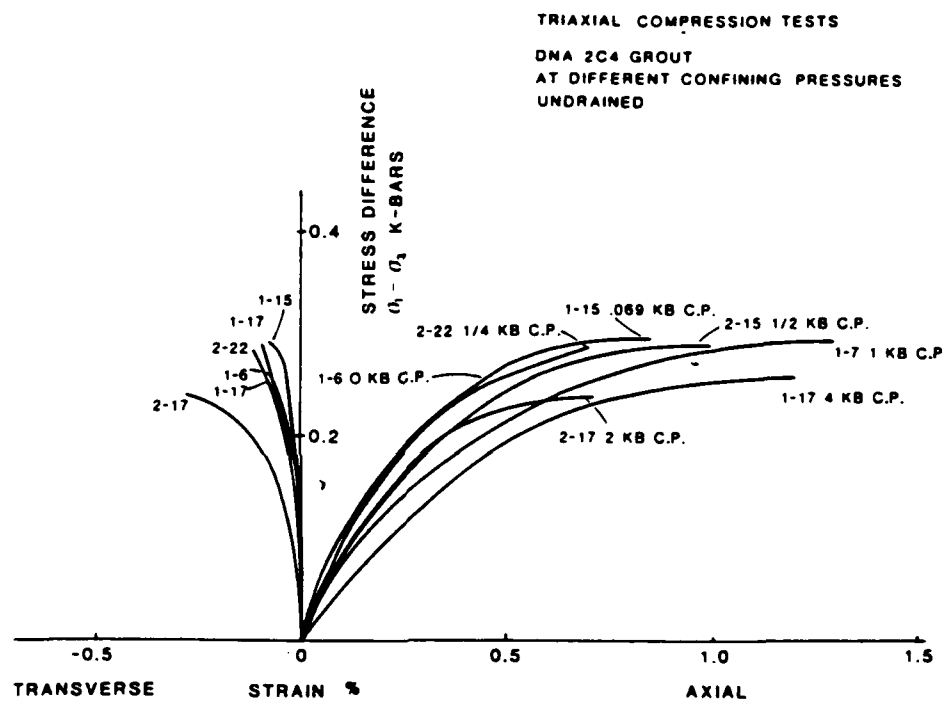


Figure 2.4. Triaxial compression tests, at different confining pressures, undrained.

where  $b = dY/d\bar{P}$  is the slope of the failure surface,  
 $J_2$  is the second deviatoric stress invariant,  $\sqrt{3J_2}$  is  
 therefore, the stress difference,  
 $J_3$  is the third deviatoric stress invariant  
 and  

$$\bar{P} = P - 1/2 (J_3/2)^{1/3}.$$

Tension failure is assumed to occur in an element if a principal stress becomes tensile only when the element has previously exceeded the failure surface, which has been calibrated to give the tensile strength for extensional states. We then apply the tension failure model proposed by Maenchen and Sack (Reference 18) and introduce an inelastic strain normal to the crack which is just sufficient to zero the normal stress. Stress components are calculated from Hooke's law. The inelastic strain increments are accumulated during each cycle in which the normal stress is calculated to be tensile, thus giving an estimate of the crack width. Once this unadjusted principal stress becomes compressive, the crack width begins to decrease. Crack closure continues until the inelastic strain becomes zero. When this state is achieved, the element is able to support a compressive stress.

Grout spheres calculations, see Reference 3, made with the above material properties and constitutive models, gave cavity radii 20 percent greater than the measured cavity radius of 1.0 cm. Rimer and Lie (Reference 4) chose to increase the dynamic strength of the grout above the static laboratory measurements in order to successfully match the measured cavity radius.

#### Dynamic Failure Surface

In our discussions so far, we have assumed that the strength or failure surface was an inherent material property of the grout. In fact, a number of experimenters have shown that the strength of a rock depends upon the rate of loading and inversely upon the size of

the sample tested and that the fracture toughness of the material, i.e., the stress intensity factor at which a crack will propagate unstably, should be considered the fundamental material property. The macroscopic strength is shown to depend primarily on the largest flaws in the sample. For the small scale explosive spheres experiments, we chose to neglect these size effects in the uniform grout medium.

The SRI laboratory data given in Table 2.2 and the work at WES (Reference 14) clearly indicate an increase in unconfined strengths at strain rates as low as  $0.1 \text{ sec}^{-1}$ . Work at Terra Tek (Reference 15) however, led to the conflicting conclusion that "within the resolution of these experiments, there are no perceptible strain rate effects for uniaxial strain tests and triaxial compression tests conducted at strain rates between  $10^{-5} \text{ sec}^{-1}$  and  $10^{-3} \text{ sec}^{-1}$  and for the unconfined compression tests conducted at strain rates between  $10^{-5} \text{ sec}^{-1}$  and  $10^{-1} \text{ sec}^{-1}$ ". The literature as summarized in Reference 19, does in fact show relatively small changes in strength at low-strain rates (from  $10^{-5} - 10^{-3} \text{ sec}^{-1}$ ) and larger increases in strength beginning at higher strain rates ( $10^{-3} - 10^1 \text{ sec}^{-1}$ ) depending upon material.

Rimer and Lie (Reference 4) chose to modify the static laboratory failure surface for 2C4 by assuming that strength increases linearly with the logarithm of strain rate (the classical theory for metals) beginning with a reference (static) strain rate of  $10^{-3} \text{ sec}^{-1}$ . (This was done before the Terra Tek experiments of Reference 15). Our grout spheres calculations have shown radial strain rates of  $10^5 - 10^7 \text{ sec}^{-1}$  at the shock wave, eight orders of magnitude or more greater than the static loading data and at least six orders of magnitude greater than the dynamic loading data of Table 2.2. Thus the strain rate model must extrapolate the existing data over many orders of magnitude, and therefore could be quite inaccurate. Fortunately, over most of the volume of the grout, strain rates of  $10^3 \text{ sec}^{-1}$  are exceeded only at the shock front.

In Reference 4, we reported the following dynamic failure surface for 2C4 grout.



$$Y = 0.055 f_1 + 1.6 f_2 P \text{ (Kb)}$$

$$Y_{\max} = 0.33 f_3 \text{ (Kb)}$$

where

$$f_1 = 1 + 0.32 \epsilon$$

$$f_2 = 1 - 0.0287 \epsilon$$

$$f_3 = 1 + 0.155 \epsilon$$

and

$$\bar{\epsilon} = \log_{10} (\text{radial strain rate}/0.001).$$

Due to the changing strain rates, the failure surface may be different in each grout element and at each instant of time. Adjustments of the stress deviator during dynamic yielding are accomplished using  $b = 1.6 f_2$  as the slope of the failure surface. The coefficients of the above failure surface were calculated to give both the measured unconfined compressive strength and the tensile strength at a strain rate of  $0.15 \text{ sec}^{-1}$ . At the strain rates of  $2\text{--}8 \text{ sec}^{-1}$  corresponding to the WES measurements of Reference 14, a 50 percent increase in unconfined strength is computed from the above formulas, in agreement with the WES data.

The maximum strength,  $Y_{\max}$ , from Reference 4, is 10 percent greater than given by later laboratory measurements (Figure 2.3 and Table 2.2). No data was available to normalize  $f_3$ , the increase in  $Y_{\max}$  with strain rate. The choice made in Reference 4 was to increase  $Y_{\max}$  in the same manner as the unconfined strength. However, the literature (Reference 19) indicates that rate effects are even more drastic at confining pressure than for unconfined stress states. Whenever the strain rate dependent failure model is used in conjunction with other constitutive models for strength in the remainder of this report,  $f_3$  will be increased to be equal to  $f_1$ .

This strain rate dependent failure surface of Reference 4 gave a calculated cavity radius of 0.99 cm, in agreement with the measurements. However, the higher strength resulted in an increase in the peak tangential residual stress from 625 bar to approximately 1 Kb, not compatible

with the hydrofracture measurements. When particle velocity data became available, it was clear that these high strengths also resulted in much too narrow velocity pulses. The higher value of  $f_3$  gave even narrower pulses, similar residual stress peaks, and a cavity radius of 0.84 cm.

## 2.4 THE EFFECTS OF CONSTITUTIVE MODELING CHANGES ON THE PARTICLE VELOCITIES

The starting point for our summary of the effects of constitutive modeling changes on the calculated particle velocity records are the basic constitutive models described in Section 2.3. We show comparisons between measured and calculated velocities only at a range of 1.90 cm (the other stations are qualitatively similar), beginning with Figure 2.5, for the laboratory static failure surface. The calculated peak velocity is too high, the positive pulse width is too large, and the negative pulse width is far too narrow. Invoking strain rate dependent increases in strength (see Figure 2.6) reduces the peak velocity but drastically narrows the pulses by approximately a factor of two.

A series of modeling changes were initiated which did not significantly improve the agreement between calculated velocity pulses and the measurements.

1. Crush curve variations: These mainly impacted the peak velocities at the largest ranges where void crushup is incomplete.
2. P - V EOS and elastic moduli of grout: These variations gave, at most, second order changes in results.
3. Strength, strain rate dependence, shock damage, and EOS changes in the models for the lucite shell surrounding the explosive: These variations about the models discussed in Section 2.2 gave only second order changes in results.

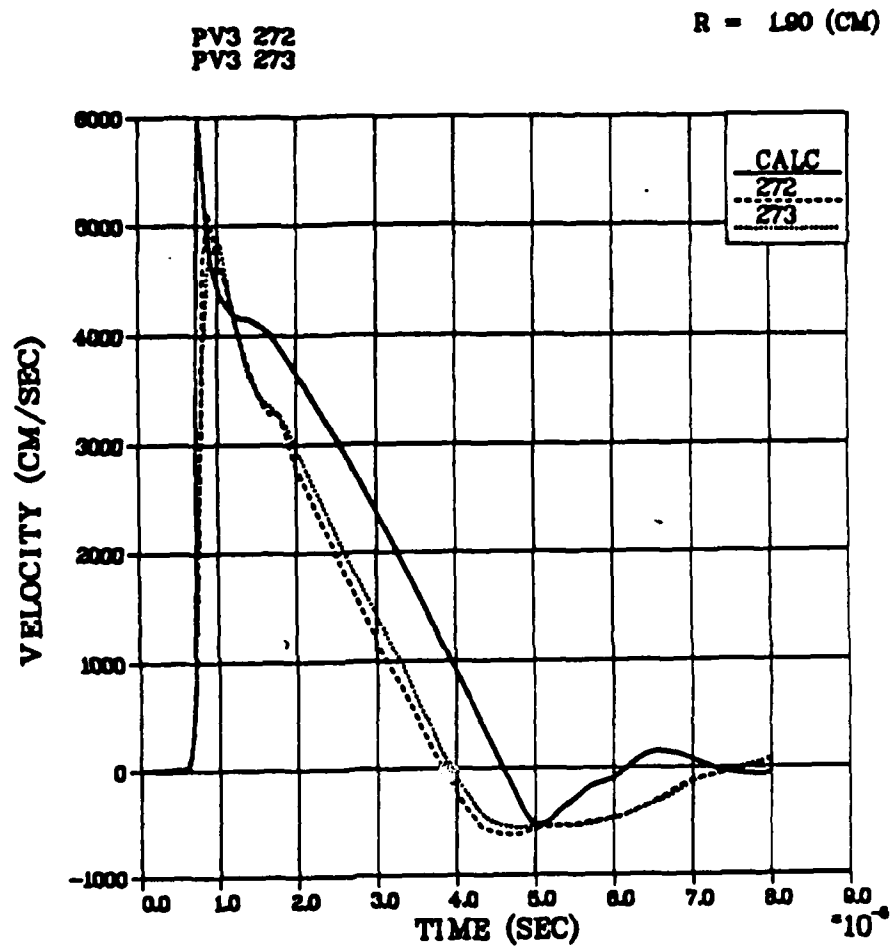


Figure 2.5. Comparison between measured particle velocities at a range of 1.90 cm in 2C4 grout and a calculation using the static laboratory measured failure surface.

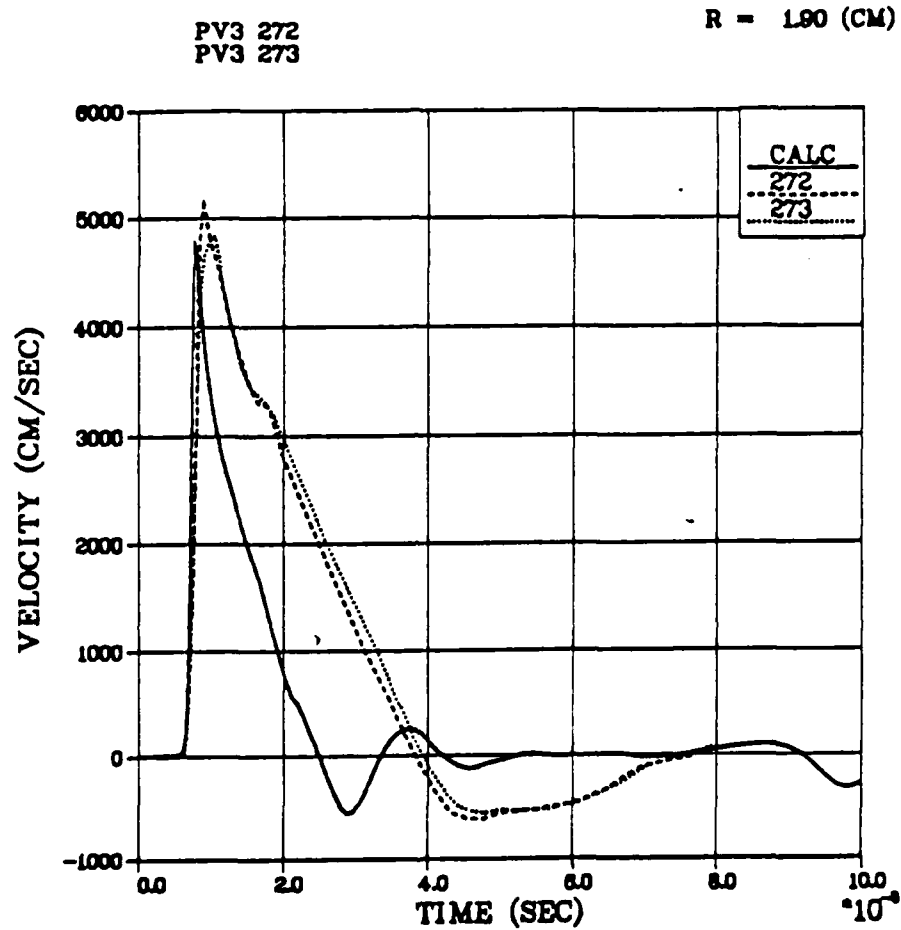


Figure 2.6. Comparison between measured particle velocities at a range of 1.90 cm in 2C4 grout and a calculation using strain rate dependent increases in strength.

4. Modifications in the HE source: As discussed in Section 2.1, the revised JWL constants resulted in some reduction of peak particle velocities at the gauge locations inside 2.0 cm.

A major improvement in the constitutive models was the incorporation of a shock damaged failure surface based on the laboratory material properties measurements shown in Figure 2.3. A calculation was made in which the allowable maximum stress difference after complete pore crushup was decreased 40 percent to a "damaged" failure surface. Strain rate dependence as given in Reference 4 was assumed to increase the strength of damaged grout in a similar manner to undisturbed grout. Partial pore crushups resulted in a "partially damaged" linearly interpolated failure surface intermediate between the two failure surfaces of Figure 2.3. This calculation gave positive particle velocity pulses slightly wider than the measurements, peak velocities larger than the data (the unrevised JWL coefficients were still being used at this time), an 18 percent reduction in peak residual hoop stress, and a slightly larger cavity than the data. Only a small improvement in negative velocity pulse width was achieved. When the more recent value of  $f_3$  for strain rate dependence was used (and the revised JWL coefficients), positive pulse widths, peak velocities and cavity radius were in good agreement with the data. Figure 2.7 compares the results of this calculation with the measurements at 1.90 cm. The major discrepancy in the simulation is in the duration of the negative pulse. The remainder of the modeling effort was largely directed toward increasing the duration of the negative velocity.

The laboratory material properties data gives no information about the extent of damage at higher stress levels. A reasonable assumption is that increased shock damage, i.e., higher peak stress levels, should reduce the maximum allowable stress difference below the 0.18 Kb value given in Figure 2.3. The calculational results shown in Figure 1.7 assumed that this strength could be reduced by shock damage to a minimum

PV3 272  
PV3 273

R = 190 (CM)

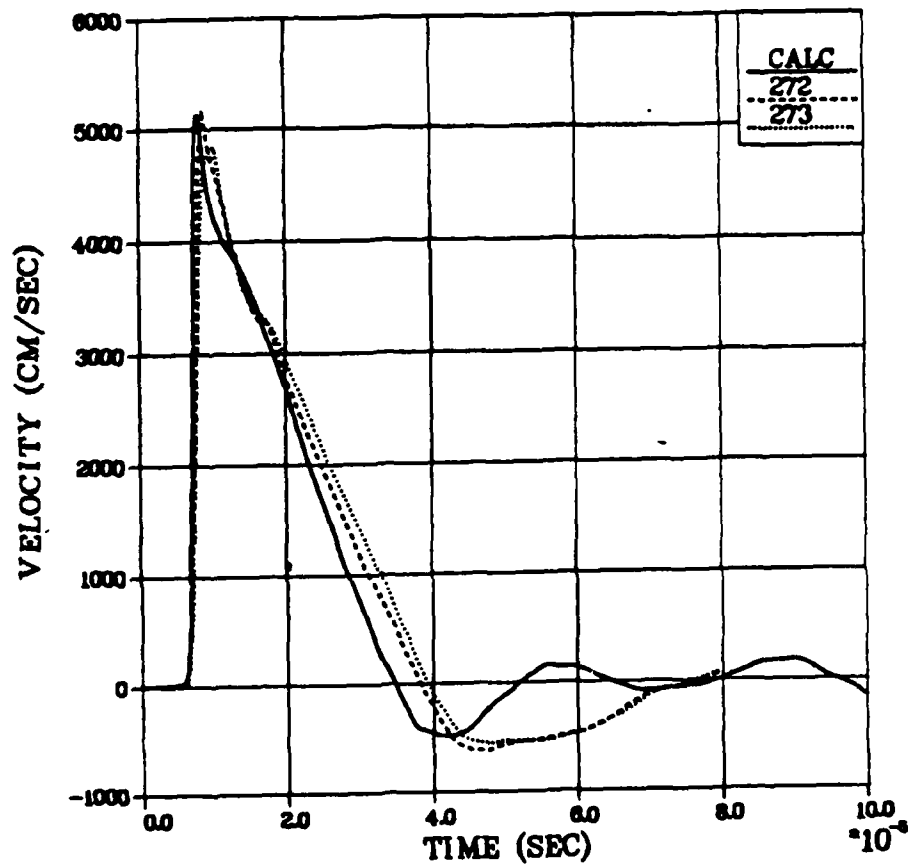


Figure 2.7. Comparison between measured particle velocities at 1.90 cm in 2C4 grout and a calculation using both strain rate dependent increases in strength and shock damage dependent decreases in strength.

value of 0.075 Kb. Another calculation with a minimum strength of 0.01 Kb gave a velocity pulse almost identical to Figure 2.7. In the two calculations, the minimum strength values, i.e., assumed maximum damage, occurred at peak stress levels of 6.5 and 7 Kb respectively for the quadratic interpolation-extrapolation parameters (in peak volume compression) chosen for the damage model.

More significant differences in the calculated velocity pulses happen when the damaged failure surface of Figure 2.3 is assumed to occur at lower peak pressure levels than the crush pressure of 3 Kb. Since material properties measurements have not been made for 2C4 samples cycled statically to lower confining pressures than 4 Kb, we do not know what damage (strength reduction) occurs at what stress level. In fact, strength reduction could be different under dynamic loading conditions than for the static laboratory loading conditions. Our calculations with the RDD model have shown that both positive and negative pulses are widened significantly when the same damage is assumed to occur at lower stress levels. Since shock loading takes place so rapidly in the 2C4 grout spheres, the calculated velocity pulses were found to be almost completely independent of whether strength reduction due to damage is assumed to occur immediately during shock loading or on subsequent unloading.

The laboratory triaxial compression tests at Terra Tek (Reference 15) at different confining pressures, summarized in Figure 2.4, were used by Patch (Reference 20) to estimate the reduction in shear modulus (increase in Poisson's ratio) during void crushup. He compared the increased values in Poisson's ratio at increased confining pressures (directly obtainable from axial and transverse strain) with the bulk moduli from the crush curve (similar to Figure 2.2) at the same confining pressures to obtain the value of shear moduli. An alternate procedure is to directly obtain  $G$  from Hooke's law for a given confining pressure by using the initial slopes of the two curves of Figure 2.4 to form the shear strain (the difference between axial and transverse strains).

We have used this procedure, which gives almost a factor of three reduction in shear modulus during loading to the crush pressure, in our grout spheres calculations. Here, the shear modulus reduction was made a linear function of the minimum specific volume of a computational element (the maximum volumetric compression). Figure 2.8 compares the measured velocities with those calculated using this shear damage model in conjunction with strain rate dependence and the shock damaged failure surface. The effects of shear damage are slightly wider positive pulses and almost 50 percent improved wider negative velocity pulses (compared to Figure 2.7) but still narrower than the data. Larger peak particle velocities (in worse agreement with the cylindrical data) are obtained at ranges outside the range of the spherical velocity data.

Further reductions in the strength of the damaged grout were needed to sufficiently widen the negative velocity pulse. Since the literature does not cover strain rate dependent strength increases for shock damaged rocks, we decided to model the damaged strength of the grout as before but not to allow strain rate effects for this material after shock loading. Simulations with this modeling change (see Figure 2.9) did widen the negative velocity pulse approximately 35 percent, but resulted in an unsatisfactory increase in positive pulse duration. Peak velocities were also higher than desired.

Strain rate dependence appeared to be necessary to narrow the positive velocity pulse. We next modeled a gradual decrease in strain rate dependence with increasing shock damage. Best results with this model (shown in Figure 2.10) occurred with a strain rate dependence prescription which decreased gradually (quadratically with peak volumetric compression) to zero at full void crushup. Peak particle velocity remained slightly high as did the positive pulse width. However the zero crossing and the negative velocity pulse were in far better agreement with the measurements than before.



PV3 272  
PV3 273

R = 1.90 (CM)

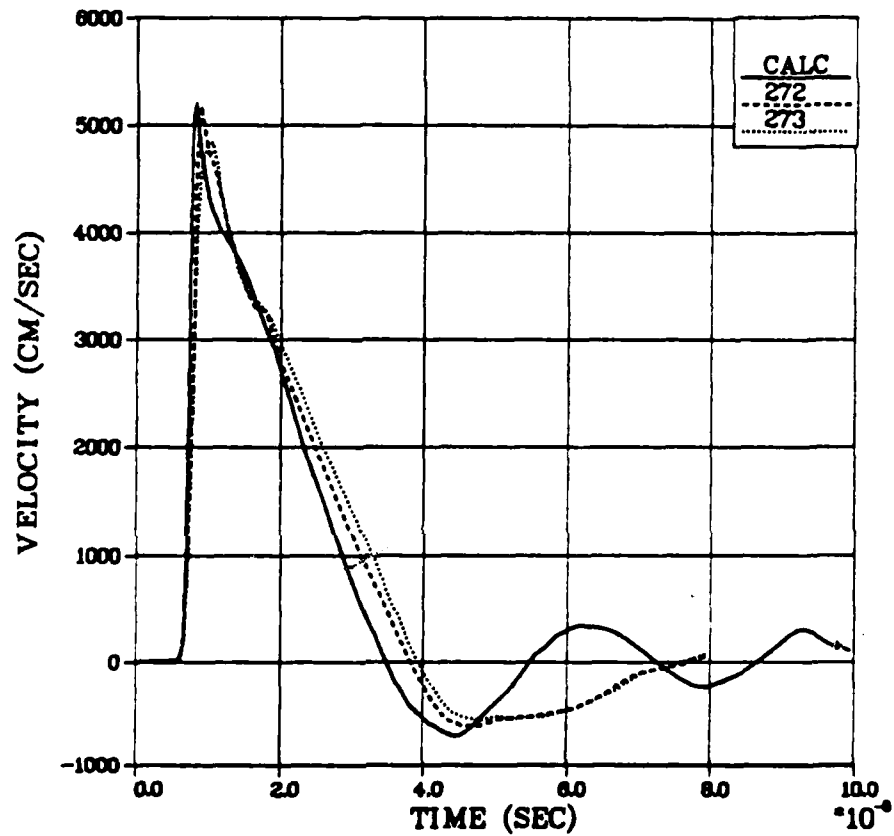


Figure 2.8. Comparison between measured particle velocities at 1.90 cm in 2C4 grout and a calculation including strain rate dependent increases in strength and shock damage dependent decreases in both strength and shear modulus.

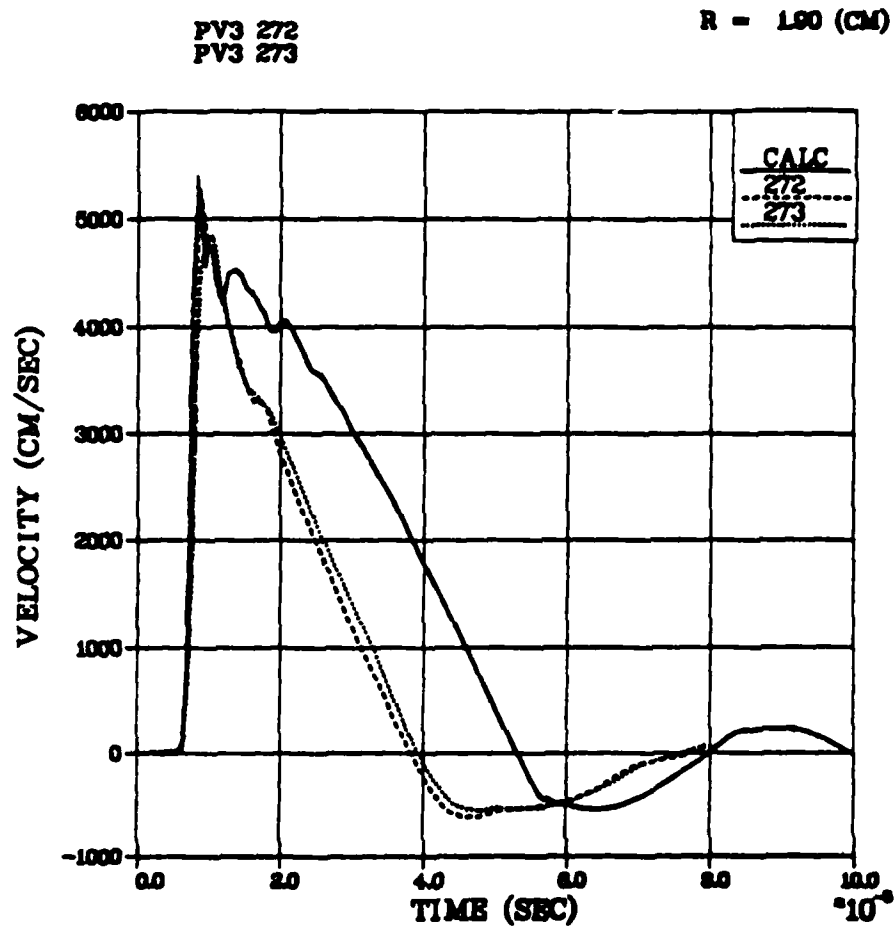


Figure 2.9. Comparison between measured particle velocities at a range of 1.90 cm in 2C4 grout and a calculation with strain rate dependent increases in strength but not for damaged grout.

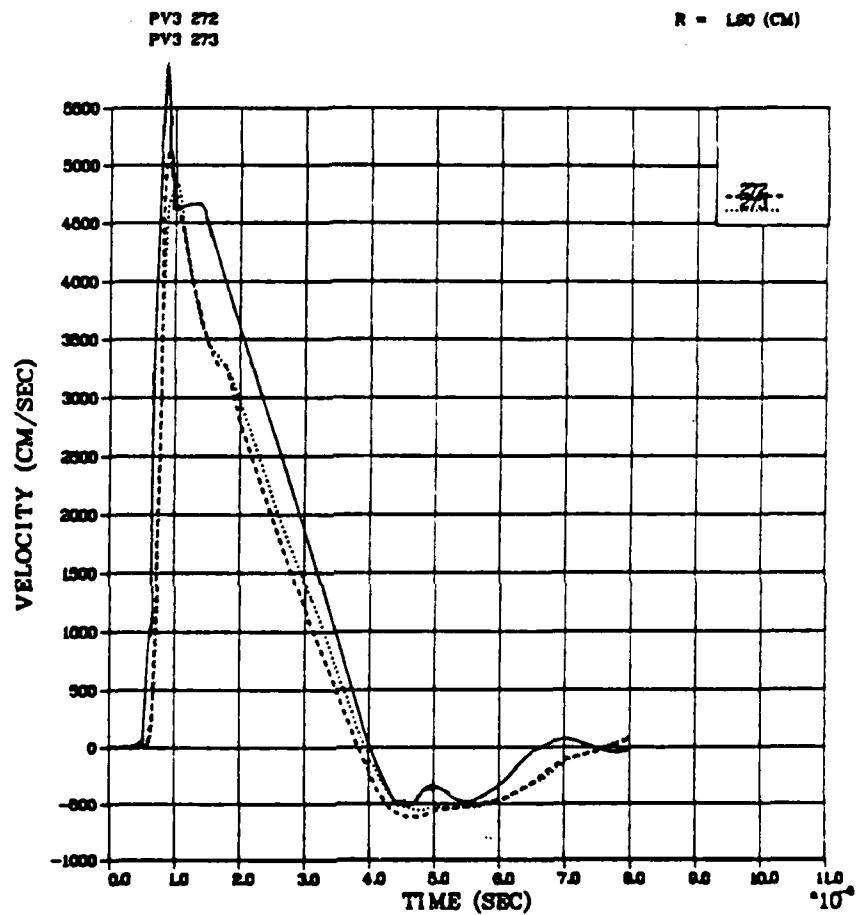


Figure 2.10. Comparison between measured velocities in 2C4 grout at a range of 1.90 cm and a calculation in which strain rate dependent increases in strength were gradually reduced to zero for increasing shock damage.

In effect, this empirical model keeps strength relatively high during shock loading and only decreases the strength later in time. We would like to have some physical basis for the decrease in strain rate dependence after shock passage. As a first try, the coefficients defining the strain rate dependence on strength were made functions of the inelastic (plastic) work in a grout element, more plastic work resulting in a gradually lower dependence of strength upon strain rate. At some prescribed value of plastic work, no strain rate dependence was allowed for the damaged grout. Several calculations were made to normalize this constitutive model to the grout spheres velocity data. Although the results were improved significantly over earlier models, we were unable to obtain results as good as those shown in Figure 2.10 with the empirical prescription for loss of strain rate dependence. Since most of the plastic work occurred quite early in the pulse, the strength was reduced too early to prevent a fat positive pulse.

Continued investigations led to the conclusion that time dependent stress relaxation was needed to give the high strength for the narrow positive velocity pulse and the low strengths at late times for the wide negative velocity pulse.

## 2.5 THE RATE AND DAMAGE DEPENDENT (RDD) CONSTITUTIVE MODELS

The RDD model was the logical culmination of our investigations, combining the most successful of the constitutive models discussed above with a time dependent relaxation of deviatoric stresses from the undamaged (strong) failure surface to the damaged (weak) failure surface. Stress relaxation is assumed to occur according to the simple Maxwell solid viscous model with a relaxation time dependent upon the amount of damage, i.e., the peak pressure or maximum compression seen by an element. The undamaged failure surface includes the strain rate dependent increases in strength needed to correctly simulate the final cavity radius and measured positive velocity pulses while the damaged failure surface, assumed to be independent of strain rate effects, is needed

to give the wide measured negative velocity pulses. Figures 1.1-1.4 show the excellent agreement between the measured particle velocities and the simulations using the RDD constitutive models. The calculated residual stress fields are shown in Figure 1.5. A cavity radius of 1.0 cm within 1 percent of the measurements was obtained.

Here we present the equations governing the constitutive models and indicate the sensitivity of the solutions to the choice of normalizing coefficients.

The Maxwell solid viscous model (Wilkins, Reference 21) assumes that the deviatoric strain rate  $\dot{\epsilon}$  can be written as the sum of an elastic component and a viscous component as follows:

$$\dot{\epsilon} = \frac{\dot{S}}{2G} + \frac{S}{2\eta}$$

where  $S$  is the deviatoric stress,  $G$  the shear modulus and  $\eta$  the coefficient of viscosity. Rewriting this equation, we obtain

$$\dot{S} = 2G \dot{\epsilon} - \frac{G}{\eta} S$$

where the first term is Hooke's law and the second represents the stress relaxation of a Maxwell solid.

Letting  $S_0$  be the stress calculated from Hooke's law, we obtain the expression for the relaxed deviatoric stress component  $S_R$

$$S_R = S_0 \left(1 - \frac{G \Delta t}{\eta}\right) \quad (1)$$

where  $\Delta t$  is the time interval and  $\eta$  is assumed to be dependent on  $S_R$ .

Cherry and Rimer (Reference 22) for a variety of NTS rocks, generalized Equation (1) to empirically represent stress relaxation

from a failure surface for a partially saturated porous material to a lower surface for the material saturated due to shock induced pore crushup according to effective stress concepts. They obtained the following expression

$$S_R = S_0 \left[ 1 - \frac{\Delta t}{\delta} \left( 1 - \frac{2}{3} \frac{Y_R}{S_0} \right) \right]$$

or more simply

$$S_R = S_0 - \frac{\Delta t}{\delta} \left( S_0 - \frac{2}{3} Y_R \right) \quad (2)$$

where  $\delta$  is a time dimensioned coefficient and  $Y_R$  represents a strength of saturated material but is given the sign of the stress deviator. (Relaxation does not occur when the magnitude of  $S_0$  is less than  $2/3 Y_R$ .)

The relaxation time,  $\delta_R$ , given by

$$\delta_R = \frac{\delta S_0}{S_0 - \frac{2}{3} Y_R} \quad (3)$$

increases as  $S_0$  approaches  $2/3 Y_R$ , thus giving a smooth transition between the Maxwell solid and elastic behavior (infinite  $\delta_R$ ). This model was calibrated to successfully simulate the particle velocity data from the Piledriver event in NTS granodiorite and has been applied to other NTS rocks including tuff, alluvium, and rhyolite (see Reference 22).

Here, the relaxation time was altered through the introduction of a function  $f_{Re}$ , to give very rapid stress relaxation where damage is greatest and very little relaxation where damage is small. Equation (2) becomes

$$S = S_0 - \frac{\Delta t f_{Re}}{\delta} \left( S_0 - \frac{2}{3} Y_R \right) \quad (4)$$

Equation (4) governs the deviatoric stress relaxation in the RDD model.  $Y_R$  may be considered the damaged strength of the element and itself is assumed to be a function of the amount of damage. The basic damage function  $f_R$  (used to define  $f_{Re}$ ) is related to the crush curve, Figure 2.2 and defined by

$$f_R = \frac{V_e - V_m}{V_e - V_c} \quad (5)$$

where  $V_e$  is the specific volume at the elastic pressure of 100 bars,  $V_m$  is the minimum specific volume seen by the element of mass (a measure of the peak pressure or maximum volumetric compression) and  $V_c$  is some reference specific volume at which the damaged failure surface of Figure 2.3 is assumed to apply. At peak pressures below the elastic pressure ( $V_m > V_e$ ),  $f_R$  is assumed to be zero while for high stresses ( $V_m < V_c$ )  $f_R$  can be greater than 1. The effect is to create a large damaged central core of grout too weak to resist the velocity rebound caused by the far stronger outer mass of grout, thus giving a large negative velocity pulse. The damage dependent relaxation time insures that the central core is weakened before rebound begins.

All damage and relaxation phenomena are normalized through the choice of  $V_c$  which determines the dependence of  $f_R$  upon peak pressure and the size of the damaged central core. The best match to the particle velocity data from 2C4 grout occurs when  $V_c$  corresponds to the 1.5 Kb pressure level in Figure 2.2 and using the following functional dependences:

1. Shear modulus is assumed to decrease linearly from 70.78 Kb to 24.5 Kb as  $f_R$  increases to 1.0. Continued reduction is allowed for larger  $f_R$  until a minimum shear modulus of 10 Kb is reached. Shear modulus reduction is allowed both on loading and unloading of an element. Calculated velocity pulses are relatively insensitive to this choice, to the choice of minimum shear modulus, and to whether linear or quadratic dependence on  $f_R$  is assumed.

2. The damaged strength,  $Y_R$ , at  $V_C$  is defined by the lower failure surface of Figure 2.3 which is described by

$$Y_R = 0.033 + 1.6 \bar{P} \text{ (Kb) .}$$

$$Y_{R_{\max}} = 0.18 \text{ (Kb) .}$$

At  $V_e$ ,  $Y_R$  is given by

$$Y_R = 0.055 + 1.6 \bar{P} \text{ (Kb)}$$

$$Y_{R_{\max}} = 0.30 \text{ (Kb)}$$

which is the upper (undamaged) failure surface of Figure 2.3 without strain rate dependent strength increases.

The reduction in  $Y_R$  is assumed to be quadratically dependent upon  $f_R$  and to continue until a minimum strength of 0.01 Kb is reached. The calculated negative velocity pulses depend only slightly upon the minimum strength and are somewhat narrower if linear dependence upon  $f_R$  is chosen.



3. Strain rate dependent strength increases are assumed to occur only for undamaged grout or during loading of an element. The failure surface is given by

$$Y = 0.055 f_1 + 1.6 f_2 \bar{P} \quad Kb$$

$$Y_{max} = 0.30 f_3 \quad Kb$$

where

$$f_1 = 1 + 0.32 \bar{\epsilon}$$

$$f_2 = 1 - 0.0287 \bar{\epsilon}$$

$$f_3 = 1 + 0.32 \bar{\epsilon}$$

and

$$\bar{\epsilon} = \log_{10} (\text{radial strain rate}/0.001)$$

4. The Maxwell solid deviatoric stress relaxation as given by Equation (4) is controlled both by the time relaxation coefficient  $\delta$ , set equal to 1.0  $\mu\text{sec}$ , and  $f_{Re}$  set equal to the square of the damage function,  $f_R$ . To avoid extremely rapid relaxation in the central core,  $f_{Re}$  is not allowed to be greater than 10. A numerical restriction is also imposed which limits  $f_{Re}$  to be less than the ratio  $\delta/\Delta t$  to prevent the deviator from changing sign for a large time step. The calculated velocity pulses are somewhat narrower when  $f_{Re}$  is not allowed to be greater than 1.0.

In the finite difference calculations, the time of shock loading is nonphysical, controlled by numerical artificial viscosity. To insure that stress relaxation is not dominated by these nonphysical effects, our model does not permit relaxation until shock loading has been completed. This restriction was put into the model for future simulations of larger scale events for which the numerical timestep may be comparable to or larger than  $\delta$ . (For the small scale grout spheres tests,  $\delta$  is equal to approximately 100 time steps.) Simulations of the velocity records for 2C4 grout were also made allowing stress relaxation on loading with no significant change in results. However, later simulations for the high porosity LD2C4 grout in which

loading times were much greater showed a dependence upon whether relaxation was or was not allowed on loading. Physically, the effect of not allowing relaxation on loading combined with the strain rate dependent increases in strength implies almost no shear failure during the rapid loading of the grout.

The calculations made using the RDD model as described above were normalized to the particle velocity data for 2C4 grout through the choice of  $\delta$  and  $V_c$ . We first attempted to match the particle velocities by equating  $V_c$  to the specific volume at which all air-filled porosity is crushed up (3-4 Kb pressure), the logical choice based on the static laboratory data of Figure 2.3, but were unable to obtain wide enough negative velocity pulses. A larger core of damaged material is needed. Figure 2.11 - 2.13 show the effects of variations in  $V_c$  and  $\delta$  on the calculated velocities at a range of 1.90 cm for early calculations made with the RDD models using 1.8 percent air-filled porosity. (The calculation for Figure 2.10 also used this slightly larger porosity). Figure 2.11, with  $V_c$  corresponding to the crush pressure and a  $\delta$  of 0.2  $\mu\text{sec}$ , shows an excellent agreement between measured and calculated positive pulses, far better than for Figure 2.10, for an earlier partially successful constitutive model, but still too narrow a negative pulse. Decreasing  $\delta$  will widen the negative pulse but will also increase the positive pulse width.

Figure 2.12 shows the effect, for the optimum  $\delta$  of 1.0  $\mu\text{sec}$ , of decreasing  $V_c$  to the 1.0 Kb pressure level of Figure 2.2. Now the damaged core is too wide giving a slightly wide positive pulse but too great a negative pulse. Figure 2.13 shows the excellent results for  $\delta$  equal to 1.0  $\mu\text{sec}$  and  $V_c$  corresponding to the 1.5 Kb level. Note that these results, for 1.8 percent porosity, differ only slightly from the best fit, for 1.5 percent porosity, shown in Figure 1.2.

Cavity radii for the three calculations shown in Figures 2.11-2.13 were within 2 percent of the best fit results and the measurements. Calculated peak residual hoop stresses for all three were

PV3 272  
PV3 273

R = 1.90 (CM)

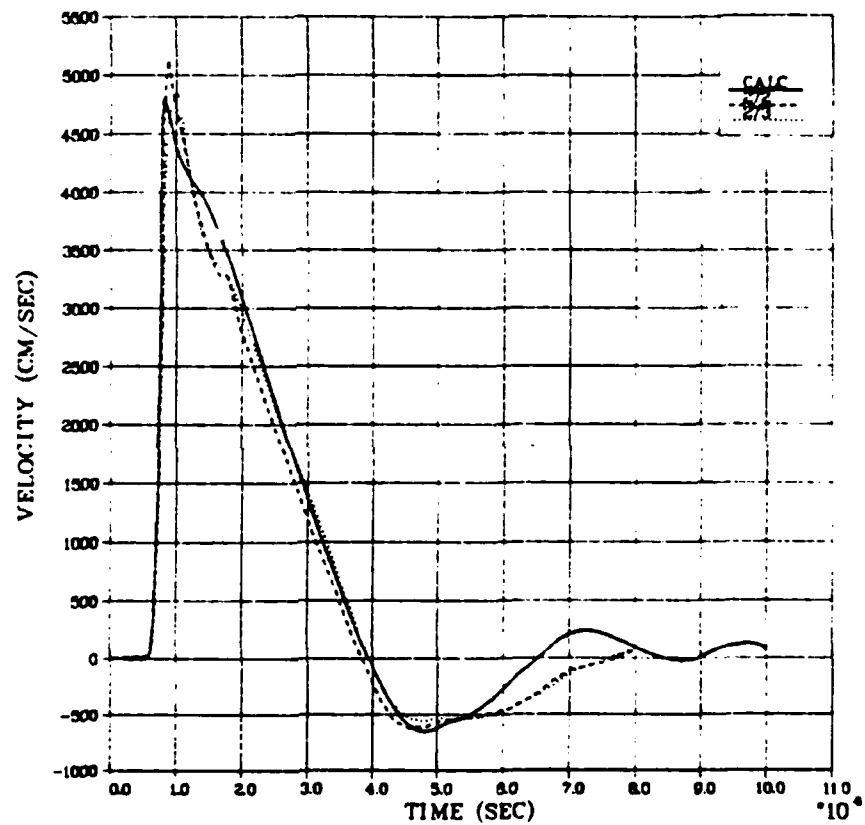


Figure 2.11. Comparison between measured velocities in 2C4 grout at a range of 1.90 cm and a calculation using the RDD constitutive models with  $V_c$  corresponding to the crush pressure,  $\delta$  equal to 0.2  $\mu$ sec, and 1.8 percent air-filled porosity.

PV3 272  
PV3 273

R = 1.90 (CM)

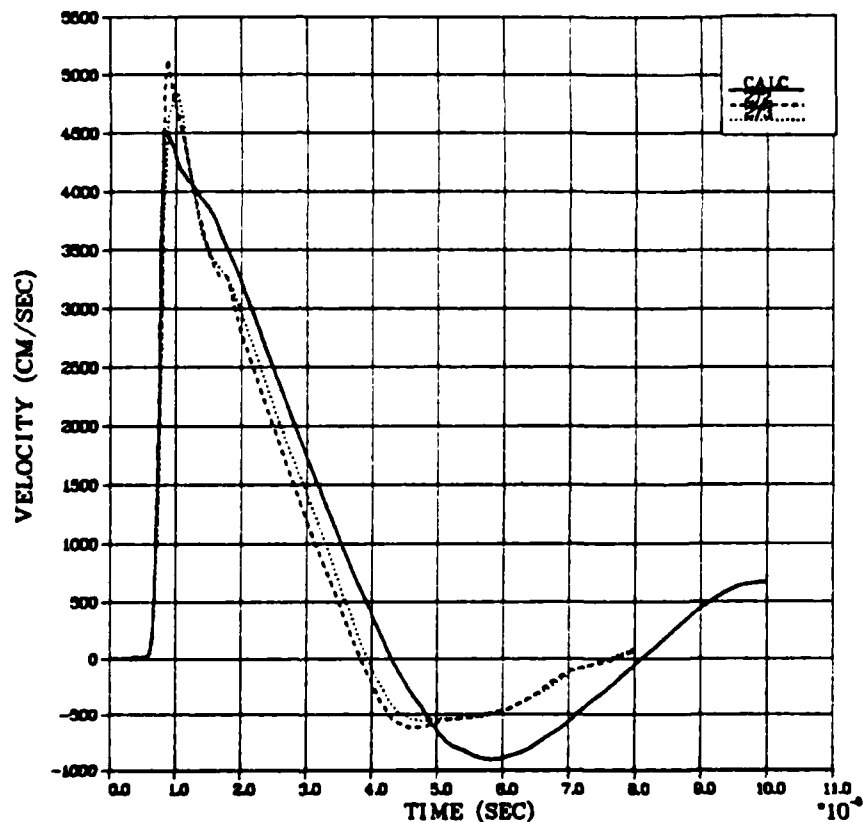


Figure 2.12. Comparison between measured velocities in 2C4 grout at a range of 1.90 cm, and a calculation using the RDD constitutive models with  $V_c$  corresponding to a pressure of 1.0 Kb,  $\delta$  equal to 1.0  $\mu$ sec, and 1.8 percent air-filled porosity.

PV3 272  
PV3 273

R = 1.90 (CM)

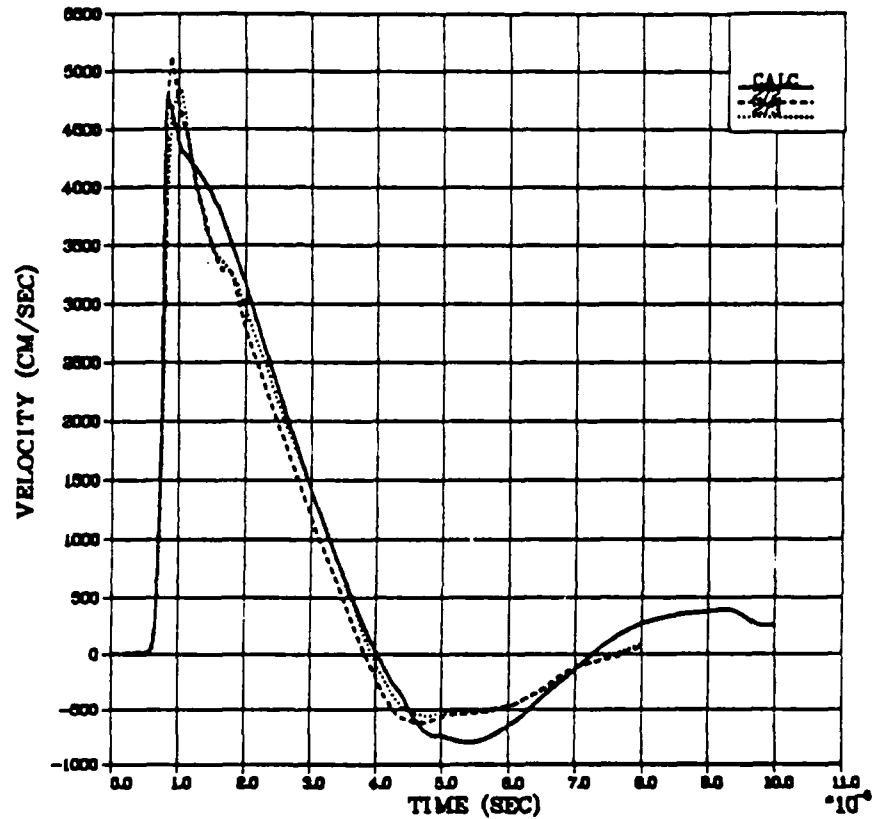


Figure 2.13. Comparison between measured velocities in 2C4 grout at a range of 1.90 cm and a calculation using the RDD constitutive models with  $V_c$  corresponding to a pressure of 1.5 Kb,  $\delta$  equal to 1.0  $\mu$ sec, and 1.8 percent air-filled porosity.

within 2 percent of the results of Figure 1.5, except for Figure 2.13, which was within 7 percent. It appears from these results that the residual stress peaks are less sensitive to modeling changes than are the velocity pulses.

## 2.6 UNIQUENESS?

The best fit results of Figures 1.1 - 1.5 were computed using the revised JWL coefficients for the PETN explosive, given in Table 2.1 and discussed in Section 2.1. As part of the study of the sensitivity of the results to choice of constants in the RDD constitutive models, we repeated our best calculation with the original JWL coefficients. The higher initial source gave slightly wider velocity pulses and higher peak velocities than the measurements. When this calculation was repeated with one significant change, a doubling of the coefficient  $\delta$  governing the relaxation time to 2.0  $\mu\text{sec}$ , the results shown in Figures 2.14-2.17 were obtained. Except for the higher peak velocities at the two closest ranges, the velocity results are as good as those in Figures 1.1-1.4. Figure 2.18 shows the calculated residual stresses which are quite similar to these shown in Figure 1.5. Thus, the RDD model gives a reasonable simulation of the particle velocity data for both descriptions of the HE source with only a change in the coefficient  $\delta$ . We chose to use the revised JWL coefficients due to the better match to in-close peak velocities shown in Figure 2.1.

The RDD models are a conglomeration of the more successful of previously tested constitutive models. We have attempted without success to attain as good agreements with the measured velocities as given in Figures 1.1 - 1.4 by making major changes in those constants of the RDD model which are not verifiable by laboratory material properties data. This, of course, does not prove the uniqueness of our models. We next considered removing some elements of the constitutive models to see whether successful simulations are still possible. Since the consequences of shear modulus reduction due to damage (wider positive and negative velocity pulses) are largely the same as those of stress relaxation, this was the obvious choice.

PV2 273

R = 127 (CM)

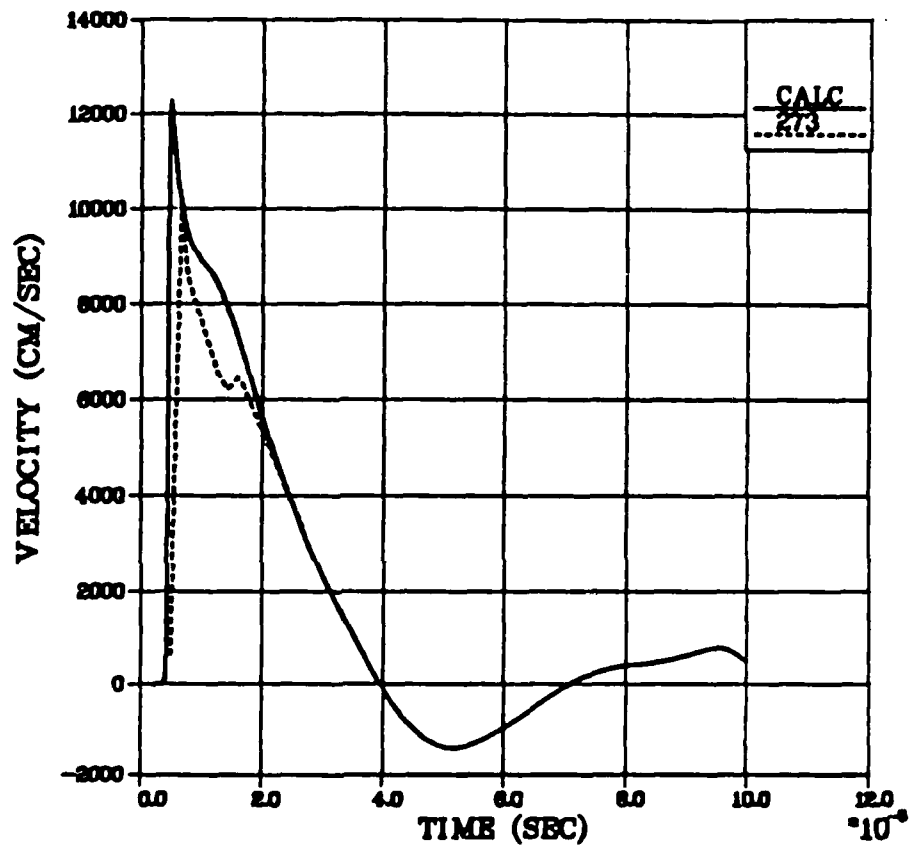


Figure 2.14. Comparison between measured velocities in 2C4 grout at 1.27 cm and a calculation using the RDD constitutive models with  $\delta$  equal to 2.0  $\mu$ sec and the original JWL coefficients for PETN.

PV3 272  
PV3 273

R = 1.90 (CM)

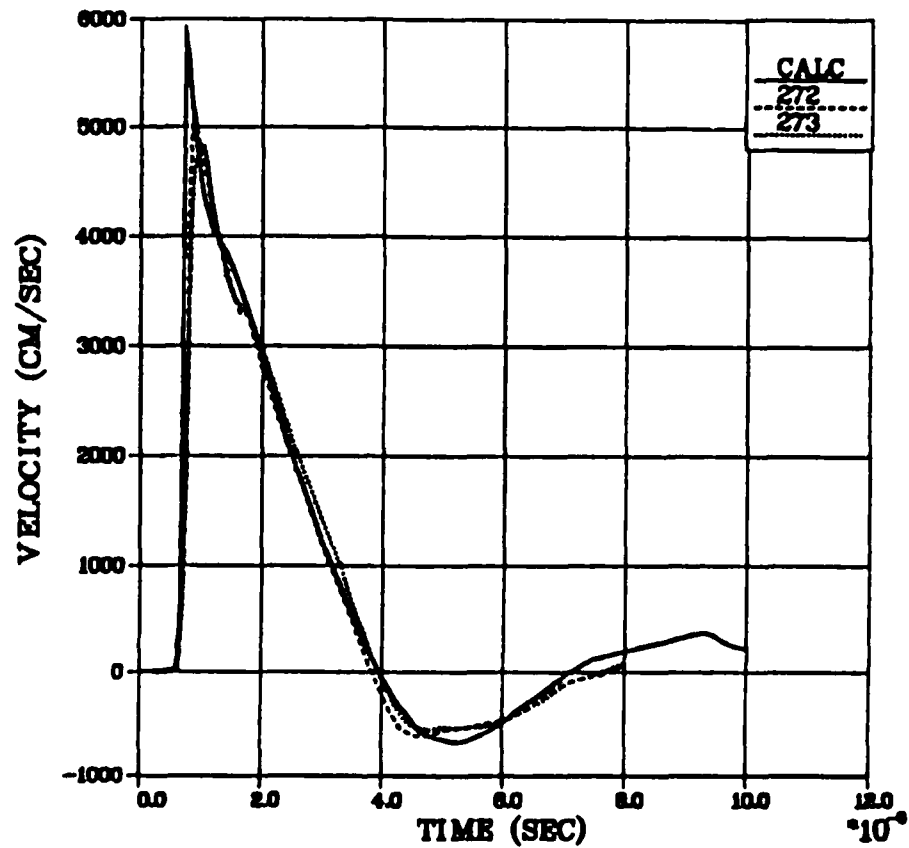


Figure 2.15. Comparison between measured velocities in 2C4 grout at 1.90 cm and a calculation using the RDD constitutive models with  $\delta$  equal to 2.0  $\mu$ sec and the original JWL coefficients for PETN.



PW 272  
PW 273

R = 2.54 (CM)

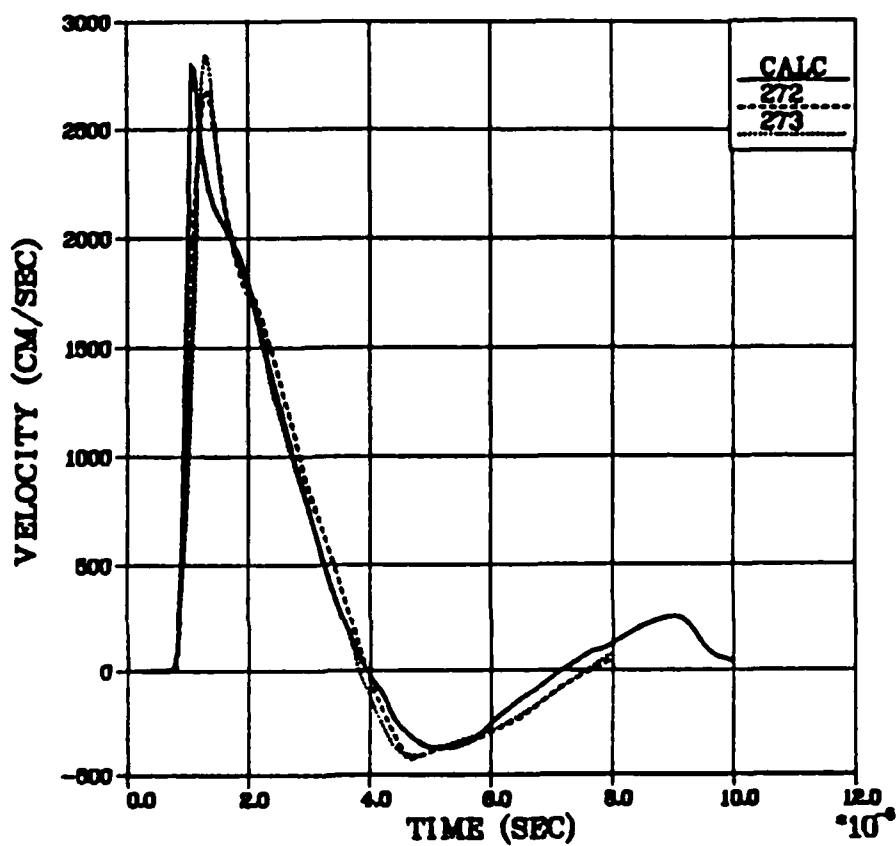


Figure 2.16. Comparison between measured velocities in 2C4 grout at 2.54 cm and a calculation using the RDD constitutive models with  $\delta$  equal to 2.0  $\mu$ sec and the original JWL coefficients for PETN.

PV5 272  
PV5 273

R = 4.00 (CM)

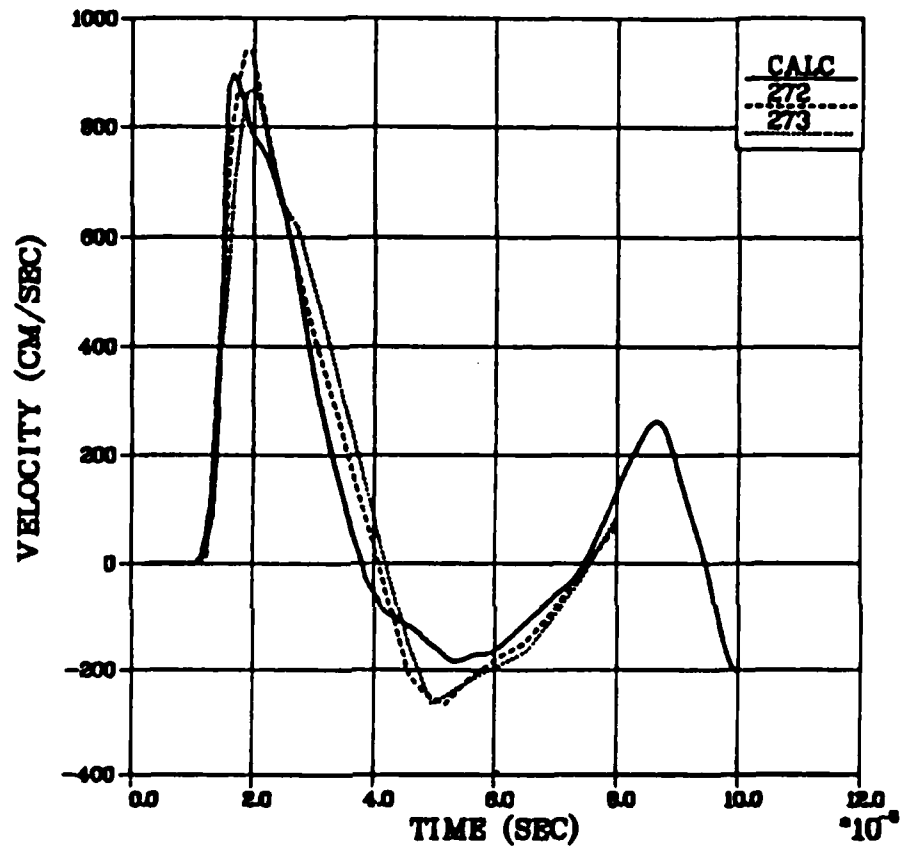


Figure 2.17. Comparison between measured velocities in 2C4 grout at 4.0 cm and a calculation using the RDD constitutive models with  $\delta$  equal to 2.0  $\mu$ sec and the original JWL coefficients for PETN.

# Skipper Stress Field 2C4 D45

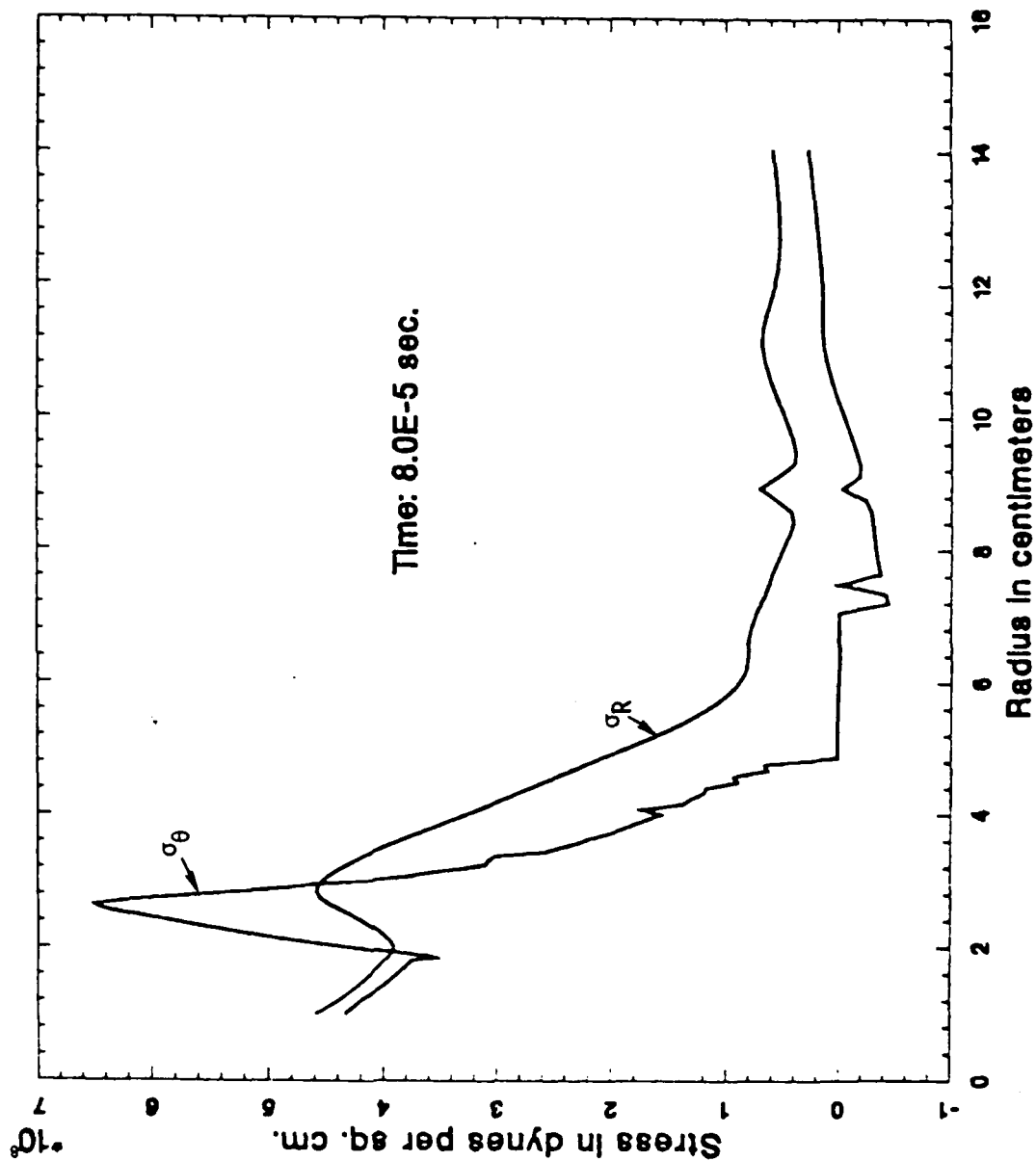


Figure 2.18. Calculated "residual" stresses for 2C4 grout at 80  $\mu$ sec using the RDD constitutive models with  $\delta$  equal to 2.0 sec and the original JWL coefficients for PETN.

Figure 2.19 shows the results of a calculation using the RDD constitutive models and constants without shear modulus reduction due to damage. Both positive and negative pulses are too narrow and the calculated cavity radius is 5 percent smaller than the measurements. This revised constitutive model was next normalized to the particle velocity data by reducing  $\delta$  from 1.0 to 0.4  $\mu\text{sec}$  in order to give a faster stress relaxation to lower stress states. Figures 2.20 - 2.23 show the results of this normalization. Figures 2.24 - 2.27 show the results of another calculation in which the particle velocities were normalized by reducing  $\delta$  to 0.6  $\mu\text{sec}$  and enlarging the damaged core with  $V_c$  corresponding to 1.0 Kbar peak pressure rather than the 1.5 Kbar peak pressure used previously.

Both solutions give a satisfactory match to the particle velocity data at 1.90 cm (Figures 2.21 and 2.15) although not as good as our best fit using the complete RDD model. Agreement is worse at the two larger ranges. Both solutions give the measured cavity radius within 1 percent. Calculated peak residual hoop stresses are almost the same in the two solutions and both are only 8 percent higher than the peaks in our best fit calculation with the complete RDD model.

Although we did not obtain the superb agreement shown in Figures 1.1 - 1.4, the solutions without shear modulus reduction may be considered acceptable simulations of the particle velocity data. Thus we have shown that the particle velocity data does not uniquely specify a constitutive model for 2C4 grout. To uniquely specify a model, stress data is required in addition to velocity data. What then is the significance of the modeling exercise described in this chapter. Of first importance, the particle velocity data has placed severe constraints on the choice of constitutive models (and material properties), eliminating many models including the simple constitutive models used to predict peak velocities and stresses in tuff. Also, we have determined the features of the constitutive models which are essential to a successful simulation of the particle velocity data for 2C4 grout and inferentially for real earth materials. These are: (1) A strength higher than given by the laboratory static failure measurements, needed

PV3 272  
PV3 273

R = 1.80 (CM)

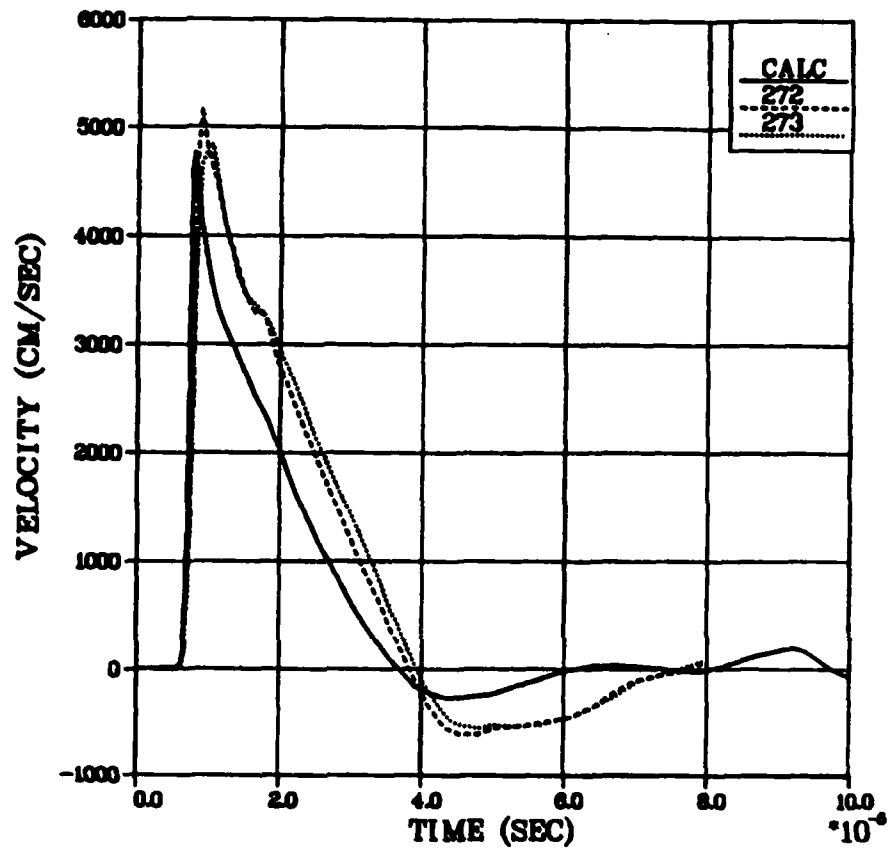


Figure 2.19. Comparisons between measured velocities in 2C4 grout at a range of 1.90 cm and a calculation using the RDD constitutive models ( $\delta$  equal to 1  $\mu$ sec and  $V_0$  corresponding to a pressure of 1.5 Kb) without shear modulus reduction due to damage.

PV2 273

R = 127 (CM)

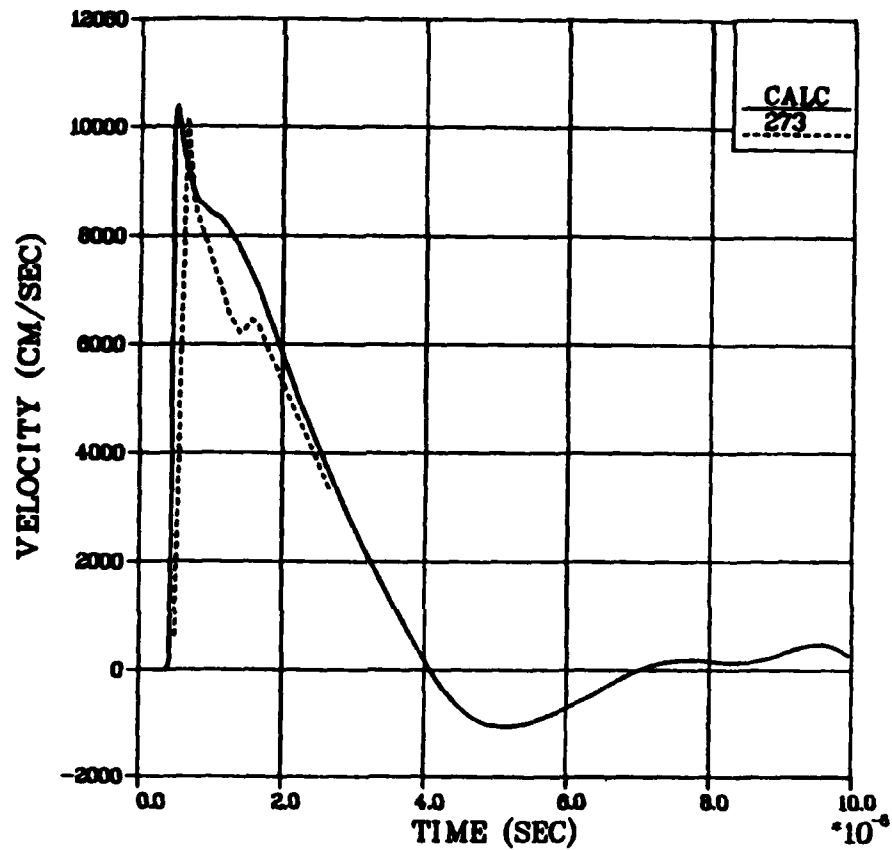


Figure 2.20. Comparison between measured velocities in 2C4 grout at a range of 1.27 cm and a calculation using the RDD constitutive models without shear modulus reduction due to damage,  $\delta$  equal to 0.4  $\mu$ sec and  $V_c$  corresponding to 1.5 Kb pressure.

PV3 272  
PV3 273

R = 1.90 (CM)

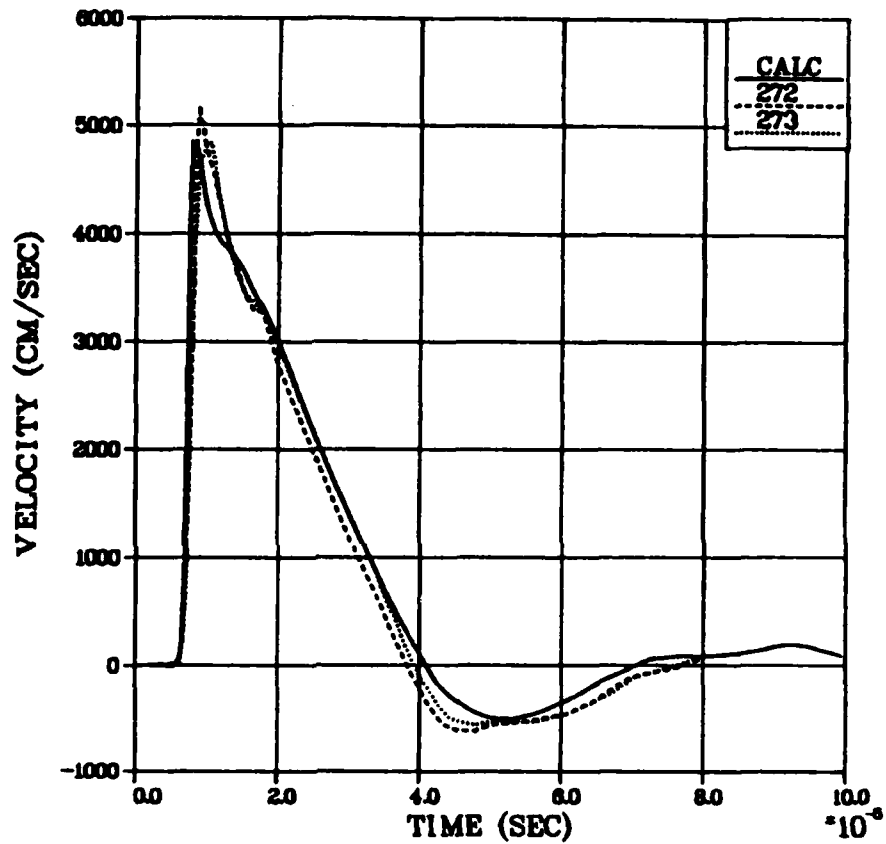


Figure 2.21. Comparison between measured velocities in 2C4 grout at a range of 1.90 cm and a calculation using the RDD constitutive models without shear modulus reduction due to damage,  $\delta$  equal to 0.4  $\mu$ sec and  $V_c$  corresponding to 1.5 Kb pressure.

PW 272  
PW 273

R = 2.54 (CM)

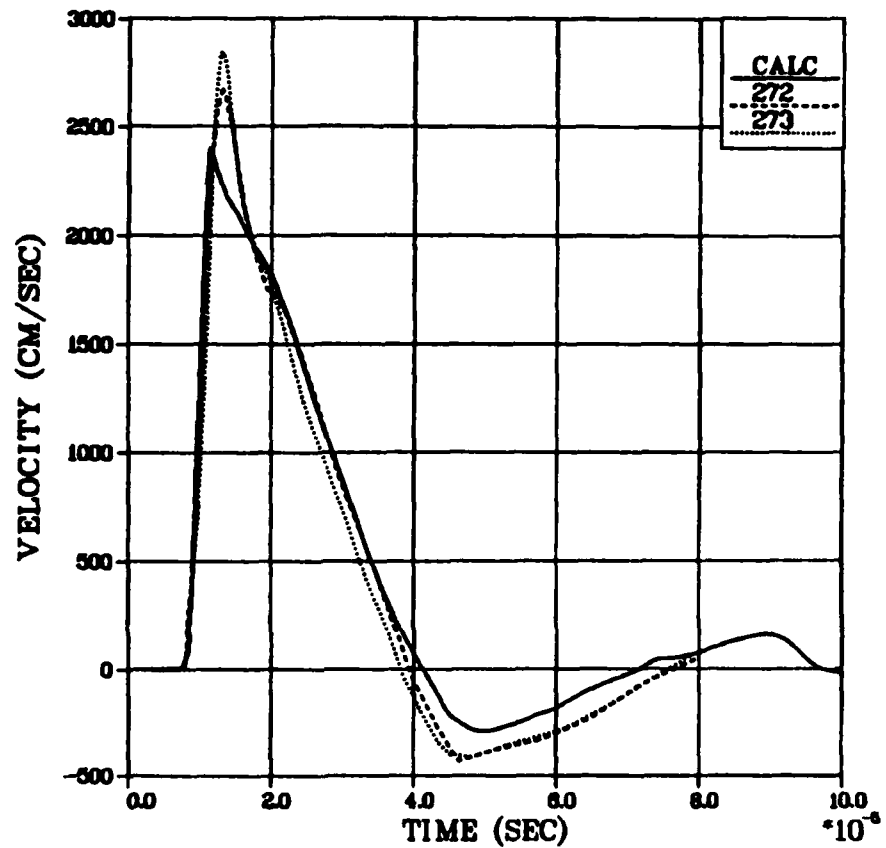


Figure 2.22. Comparison between measured velocities in 2C4 grout at a range of 2.54 cm and a calculation using the RDD constitutive models without shear modulus reduction due to damage,  $\delta$  equal to 0.4  $\mu$ sec and  $V_c$  corresponding to 1.5 Kb pressure.



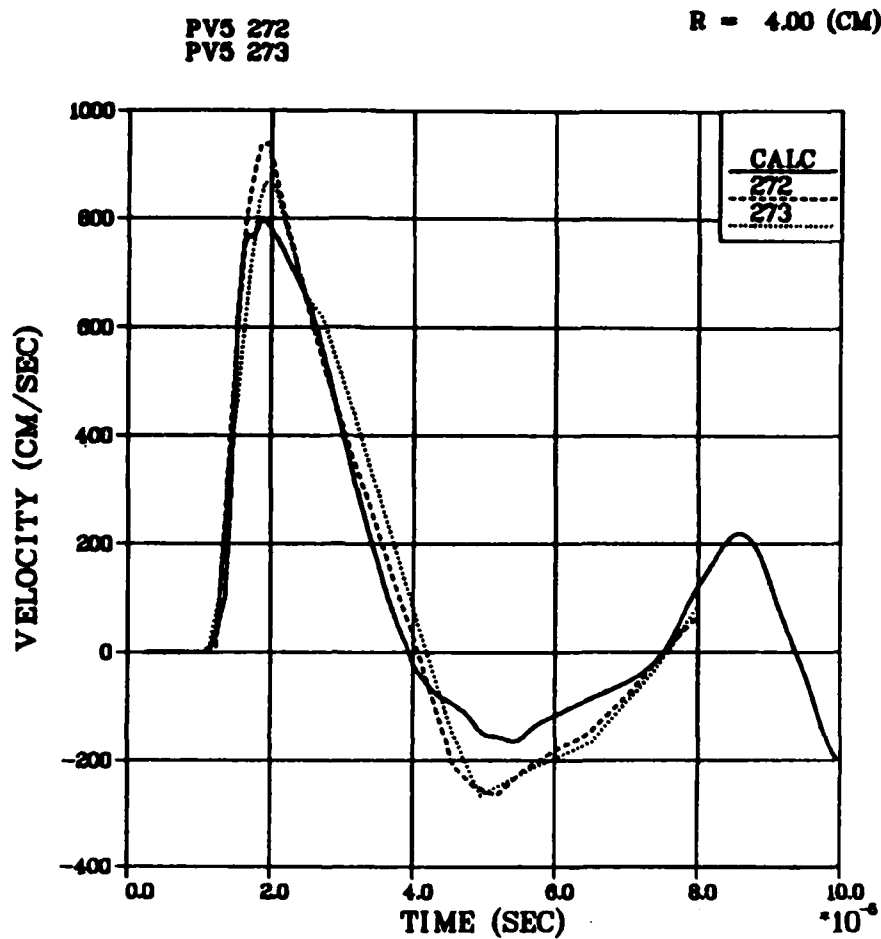


Figure 2.23. Comparison between measured velocities in 2C4 grout at a range of 4.0 cm and a calculation using the RDD constitutive models without shear modulus reduction due to damage,  $\delta$  equal to 0.4  $\mu$ sec and  $V_c$  corresponding to 1.5 Kb pressure.

PV2 273

R = 127 (CM)

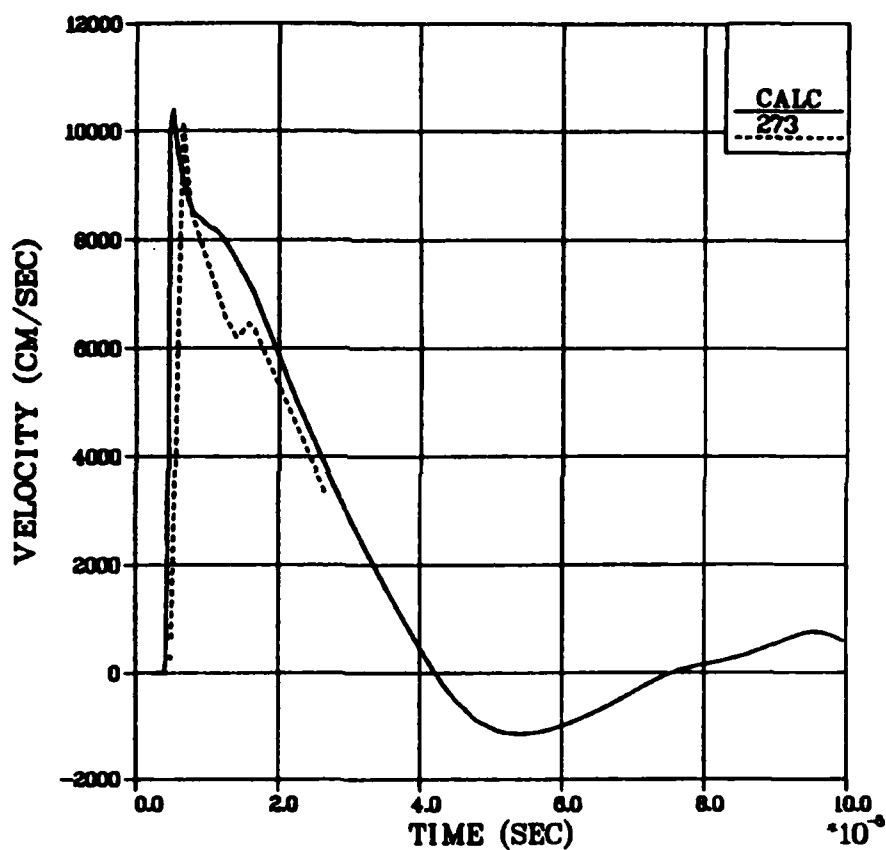


Figure 2.24. Comparison between measured velocities in 2C4 grout at a range of 1.27 cm and a calculation using the RDD constitutive models without shear modulus reduction due to damage,  $\delta$  equal to 0.6  $\mu$ sec and  $V_c$  corresponding to 1.0 Kb peak pressure.

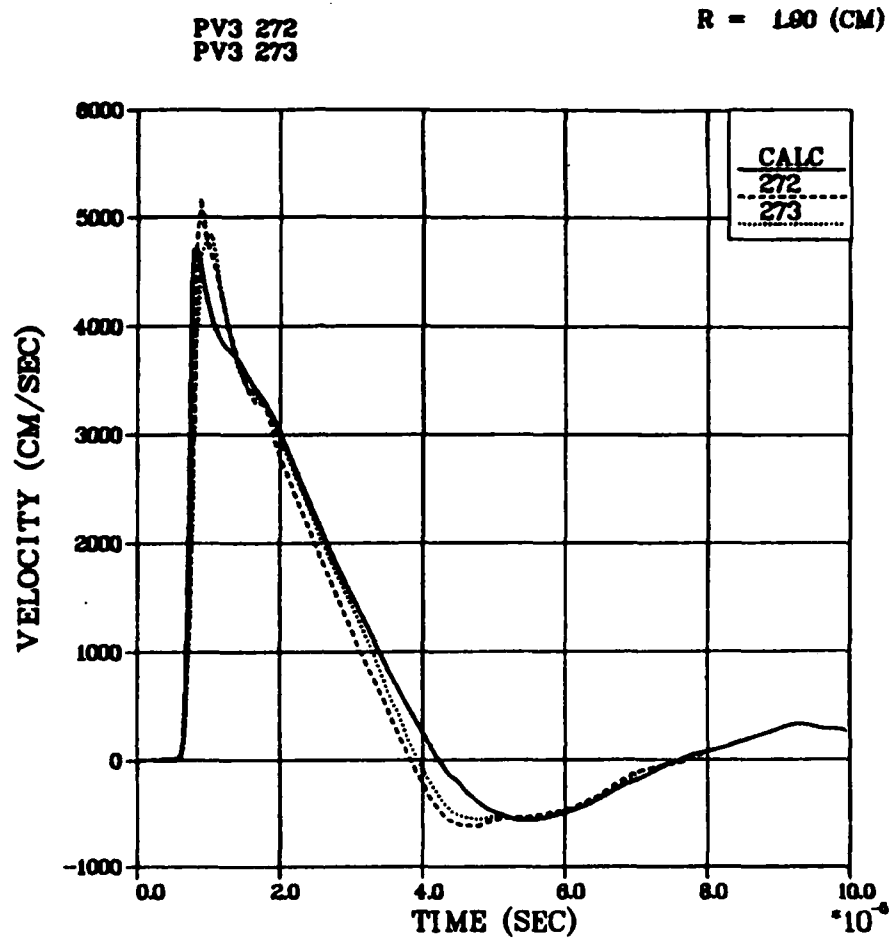


Figure 2.25. Comparison between measured velocities in 2C4 grout at a range of 1.90 cm and a calculation using the RDD constitutive models without shear modulus reduction due to damage,  $\delta$  equal to 0.6  $\mu$ sec and  $V_c$  corresponding to 1.0 Kb peak pressure.

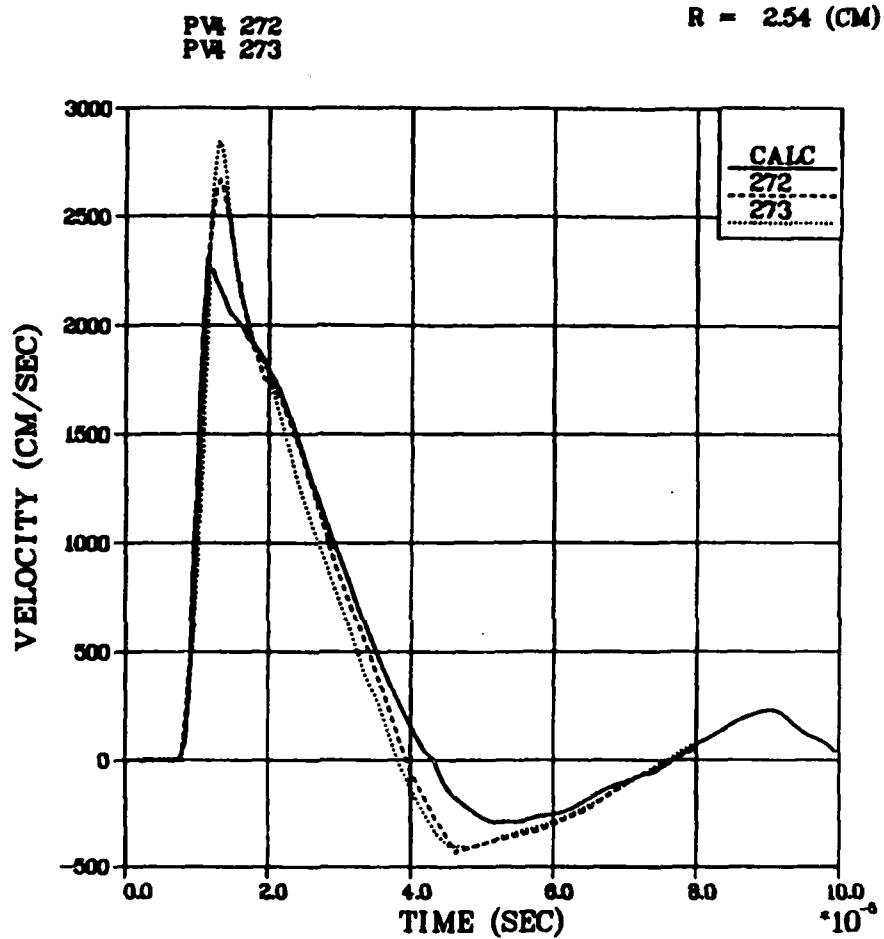


Figure 2.26. Comparison between measured velocities in 2C4 grout at a range of 2.54 cm and a calculation using the RDD constitutive models without shear modulus reduction due to damage,  $\delta$  equal to 0.6  $\mu$ sec and  $V_c$  corresponding to 1.0 Kb peak pressure.

PV5 272  
PV5 273

R = 4.00 (CM)

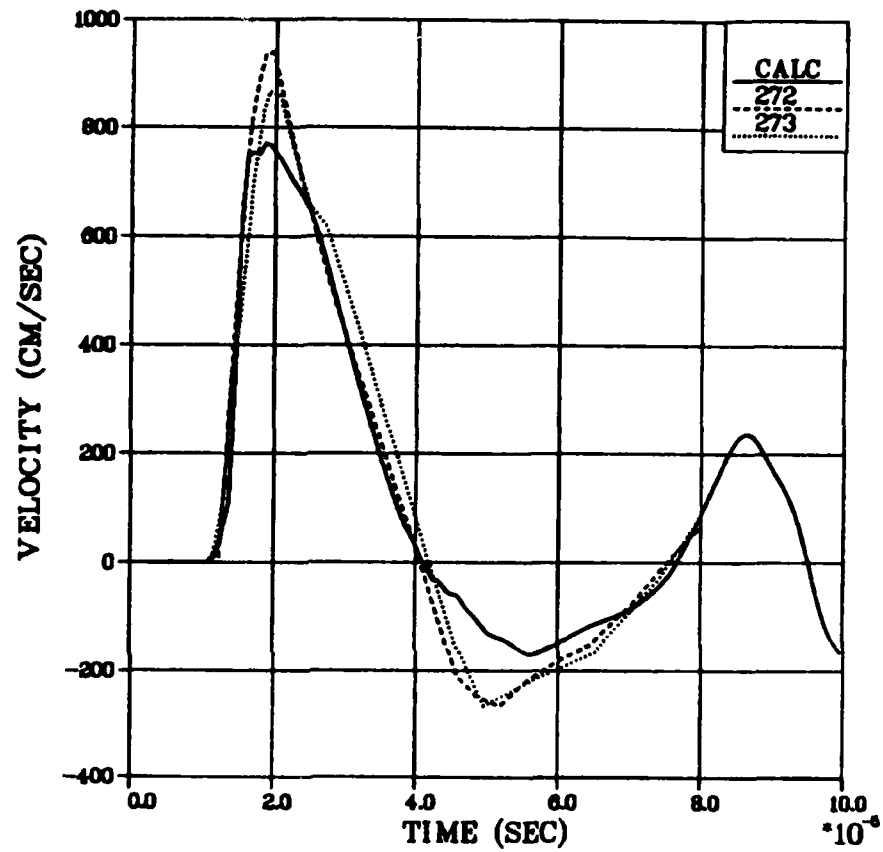


Figure 2.27. Comparison between measured velocities in 2C4 grout at a range of 4.0 cm and a calculation using the RDD constitutive models without shear modulus reduction due to damage,  $\delta$  equal to 0.6  $\mu$ sec and  $V_c$  corresponding to 1.0 Kb peak pressure.

to retard cavity growth and sufficiently narrow the positive velocity pulse, (2) A much lower strength after shock passage (pore crushup) to provide a weaker central core of grout, and therefore a wide negative velocity pulse, and (3) a prescription for the reduction in strength from (1) to (2).

We have also found that the different models and "material properties" which successfully simulate the particle velocity data in 2C4 grout all give approximately the same cavity radius and residual stress fields. Thus the primary features of interest to containment may be calculated with any of the successful models.

The RDD constitutive models, since they include rate dependent effects (both strain rate dependent strength increases and time dependent stress relaxation), introduce "size" effects into the calculations that were not present with the constitutive models used in the past. Computational results at one explosive yield may not now be simply scaled (cube root of yield scaling of linear dimensions and times) to give results at a different yield unless we make the unwarranted assumption that "material properties" of the grout such as  $\delta$  or the coefficients of the strain rate increases in strength,  $f_1$ ,  $f_2$  and  $f_3$ , depend upon the magnitude of the explosive. At nuclear yields, since strain rates are much lower (at a scaled range from the explosive) than for the grout spheres experiments, increases in strength may be negligible. Also, since shock loading times in a nuclear event are very large compared to  $\delta$  (a few microseconds), the stress relaxation to the damaged failure surface could be considered to occur instantaneously. Thus some of the simple models used in the past may still be relevant to nuclear events once some form of stress relaxation is included.

In the next chapter, we introduce yet another constitutive model, the effective stress model, which also has the essential features (1) - (3) needed to simulate the particle velocity data for 2C4 grout. This model gives excellent agreement with the measured velocities and since it is rate independent, can be simply scaled from one explosive yield to another.

## SECTION 3

### EFFECTIVE STRESS MODELS FOR 2C4 GROUT

Here, we discuss numerical simulations of the particle velocity data from the 2C4 grout experiments using yet another constitutive model, the effective stress model developed by Cherry and Rimer. A purely experimental test is proposed to determine the validity of the effective stress model versus the RDD model for the grout spheres tests.

#### 3.1 THE EFFECTIVE STRESS MODEL

In porous, permeable, partially saturated rocks, an increase of pore fluid pressure has been shown by many experimenters (see Heard, Reference 23) to drastically lower the failure strength. Garg and Nur (Reference 24) used this result to express the strength as a function of the "effective" stress applied to the sample, i.e.,

$$Y = F(\sigma_{ij} - P_f \delta_{ij})$$

where  $\sigma_{ij}$  represents the externally applied stress,  $P_f$  the pore fluid pressure and  $\delta_{ij}$  is the Kronecker Delta. In this "effective stress law" formulation, the increases in strength due to external stresses (confining pressure) are ameliorated by the buildup in pore fluid pressure when fluid is present in the rock.

Cherry and Peterson (Reference 25) first used the effective stress concept to successfully match explosively induced ground motion in blocks of grout. They assumed that during shock passage the correct strength was the dry strength of the grout (to which a strain rate dependent strength increase was added) and used a Maxwell solid formulation to relax between the dry strength and the much lower wet strength obtained from an effective stress law. Cherry and Rimer (Reference 22) later coupled the rate dependent Maxwell solid stress relaxation from the dry to the saturated strength with the removal of

all air-filled porosity for NTS rocks such as granodiorite, rhyolite, tuff, and alluvium.

More recently, Cherry and Rimer (Reference 5) have removed the rate dependence from their model by replacing the Maxwell solid formulation with a direct estimate of the pore fluid pressure, based on the amount of irreversible crushup of air-filled porosity. The resulting effective stress model thus allows simple scaling with the cube root of yield. In this model, the maximum stress difference  $Y$  remains a function of  $\bar{P}$ , (see Section 2.2), now defined as an effective  $P$  by

$$\bar{P} = P_{\text{eff}} - 1/2(J_3/2)^{1/3}$$

where

$$P_{\text{eff}} = P - P_f$$

is the effective pressure. The effective pressure is defined as a function of the parameter  $\alpha$  from the  $P$ - $\alpha$  void crushup model. The distension ratio  $\alpha$  is a function of the air-filled porosity  $\phi_A$  given by

$$\alpha = \frac{1}{1 - \phi_A}$$

and decreases from some initial value (greater than 1) down to 1.0 when all air-filled porosity has been irreversibly crushed up.

At the crush pressure ( $\alpha = 1.0$ ),  $P_{\text{eff}}$  is set to zero or equivalently, the pore fluid pressure  $P_f$  is assumed to be in equilibrium with the mean stress in the rock. Through the dependence of the strength  $Y$  upon  $\bar{P}$ , this directly gives the saturated strength of the rock.

Below some peak elastic pressure  $P_e$  (100 bars in Figure 2.2) where  $\alpha$  is greater than  $\alpha_e$ , pore fluid pressure is assumed to be



negligible so that  $P_{eff}$  is set to the mean stress  $P$ , thus giving the dry strength of the rock.

At intermediate states ( $1 < \alpha < \alpha_e$ ) the effective stress is defined by

$$P_{eff} = P - P_f = \left( \frac{1 - \alpha}{1 - \alpha_e} \right) P$$

to give failure surfaces intermediate between the dry and saturated surfaces.

The effective stress model as described above requires much less additional material properties data than the complicated RDD model. Only a determination of the dry failure surface ( $P_f = 0$  inside the sample) is needed. In the next section, we present numerical results for 2C4 grout made using the effective stress model.

### 3.2 RESULTS FOR 2C4 GROUT

Cherry and Rimer (Reference 5) first applied the effective stress model to successfully match the particle velocity data and measured cavity radius from the Piledriver event in NTS granodiorite. They next applied this model to successfully simulate the velocity data and cavity radii from the 2C4 grout spheres experiments. Best results were obtained using a dry failure surface slightly greater than the sloped surface of Section 2.2 and given by

$$Y = 0.09 + 1.6 \bar{P} \quad (Kb)$$

The maximum dry strength was set to 1.0 Kb, much greater than given by the laboratory measurements (shown in Figure 2.3) at some unspecified (non-zero) pore pressure. The effective stress law was applied during shock loading as well as on unload.

Figure 3.1 shows the agreement between the velocity measurement at 1.90 cm and this effective stress law calculation. Except for the larger peak velocity and slightly narrower negative pulse, these results are as good as those in Figure 1.2 using the RDD model. The larger peak velocity may indicate the need for some rate dependence under the very rapid loading conditions of these small scale tests.

For the RDD models, stress relaxation was not permitted during the time of shock loading which is controlled by non-physical numerical effects such as artificial viscosity. For 2C4 grout, the velocity results using the RDD models were largely insensitive to whether stress relaxation was permitted on loading. (This was not true for the high porosity LD2C4 grout in which loading times were much greater).

A simulation was made with the identical models to Reference 5 except that the pore pressure was allowed to increase only after shock loading was complete. The calculated particle velocities, shown in Figure 3.2, are similar to those of Figure 3.1 but with slightly narrower pulses and significantly smaller peak velocities in better agreement with the measurements. Without the pore fluid pressure buildup during loading, the grout elements had experienced the larger dry strength and therefore did not yield. We next repeated this calculation (no pore pressure buildup on loading) with a slightly lower dry strength given by

$$Y = 0.055 + 1.6 \bar{P} \quad (\text{Kb})$$

with the same maximum dry strength of 1.0 Kb. The straight line portion of this failure surface is identically that used for 2C4 grout in the RDD calculations. Although the dry strength is only slightly lower than from Reference 5, the wet (saturated) strength at zero  $\bar{P}$  is 40 percent lower. Figure 3.3 shows the wider negative velocity pulse at 1.90 cm in much better agreement with the measurements. Figures 3.4, 3.5, and 3.6 show the agreements at 1.27, 2.54 and 4.0 cm respectively. Overall these agreements are about as good as our best simulation for 2C4 grout using the RDD constitutive models.

PV3 272  
PV3 273

R = 1.90 (CM)

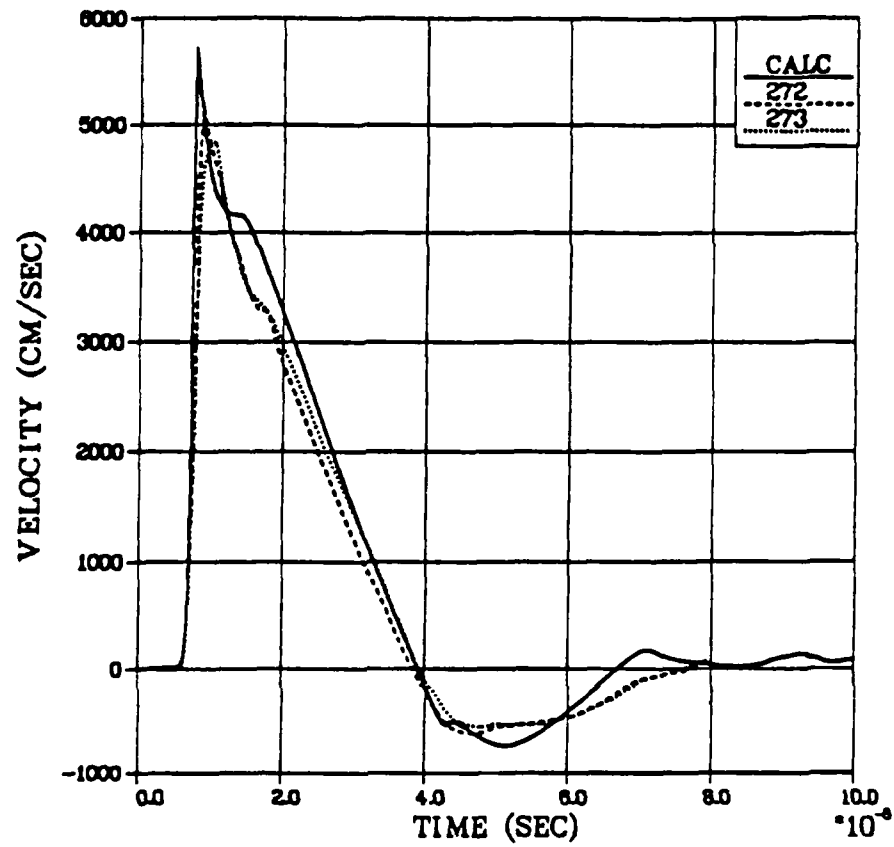


Figure 3.1. Comparison between measured velocities in 2C4 grout and effective stress law simulation at 1.90 cm (from Cherry and Rimer, Reference 25).

PV3 272  
PV3 273

R = 1.90 (CM)

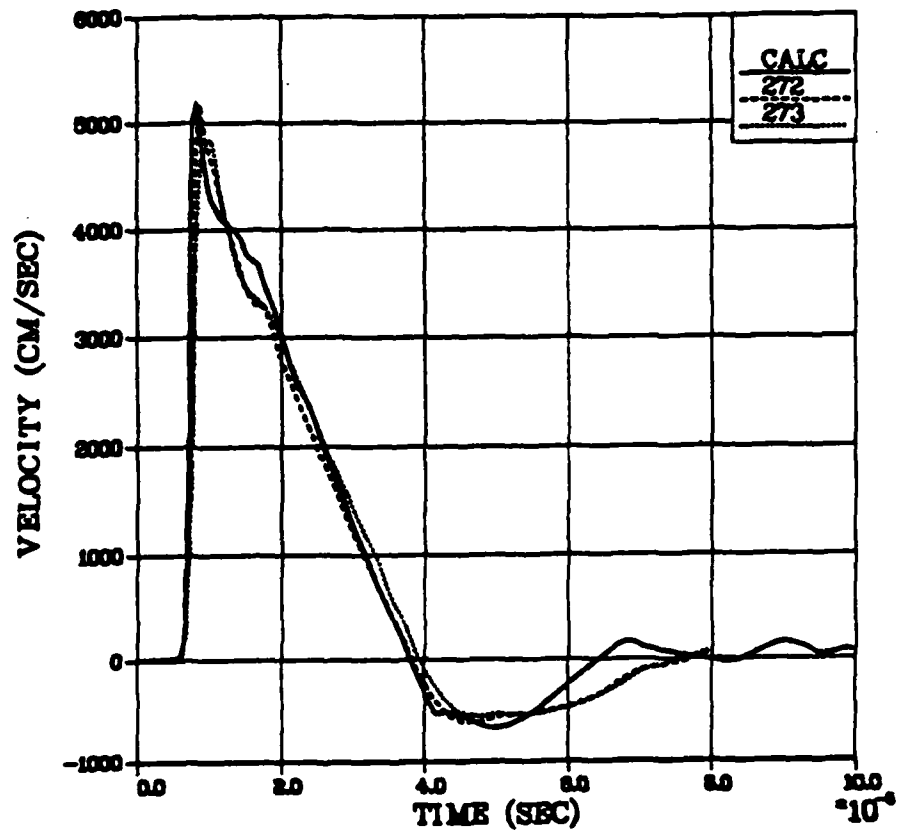


Figure 3.2. Comparison between measured velocities in 2C4 grout and effective stress law calculation at 1.90 cm (no pore pressure buildup on loading).

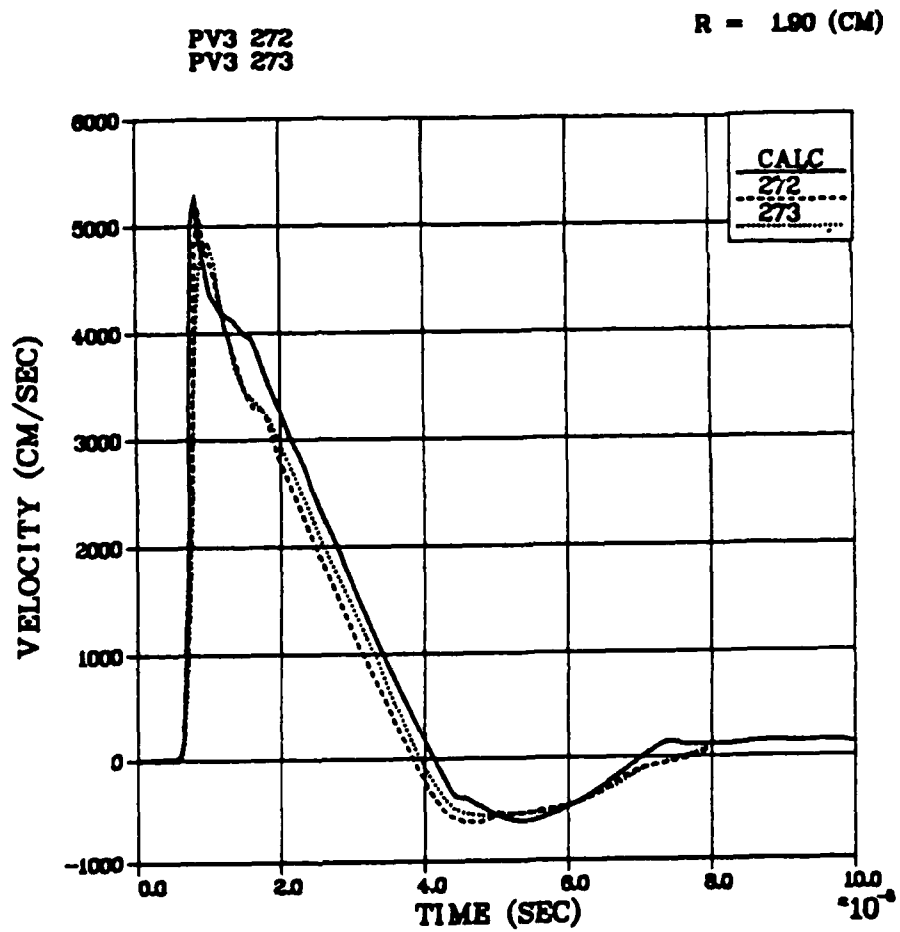


Figure 3.3. Comparison between measured velocities in 2C4 grout and best fit effective stress law calculation at 1.90 cm (no pore pressure buildup on loading).

PV2 273

R = 127 (CM)

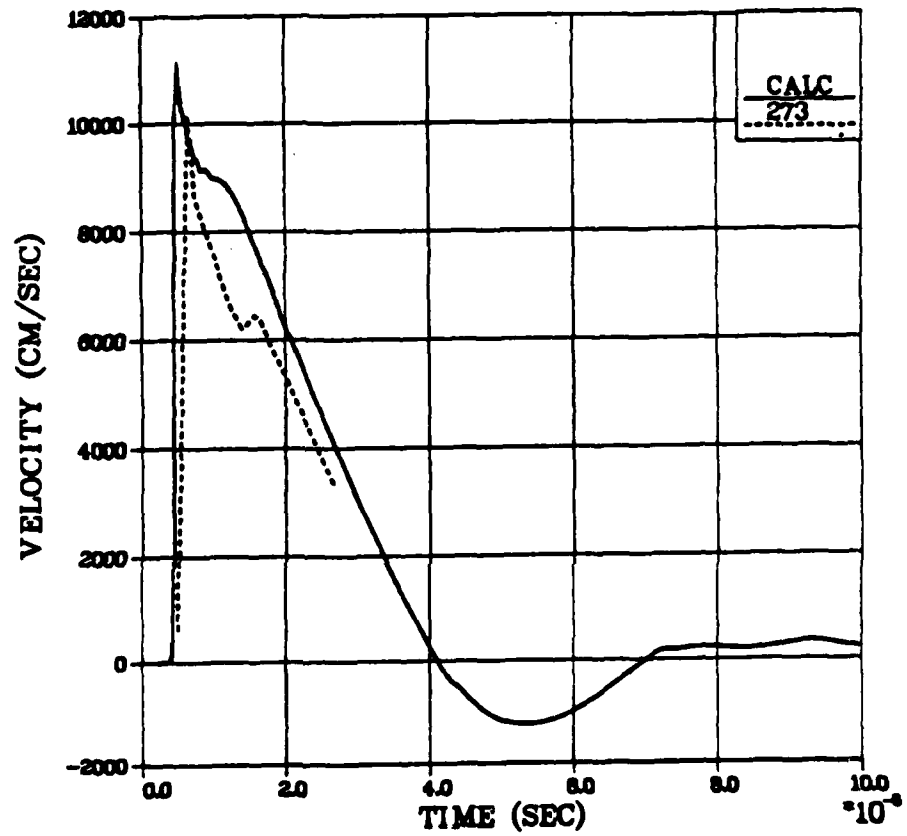


Figure 3.4. Comparison between measured velocities in 204 grout and best fit effective stress law calculation at 1.27 cm.

PW 272  
PW 273

R = 2.54 (CM)

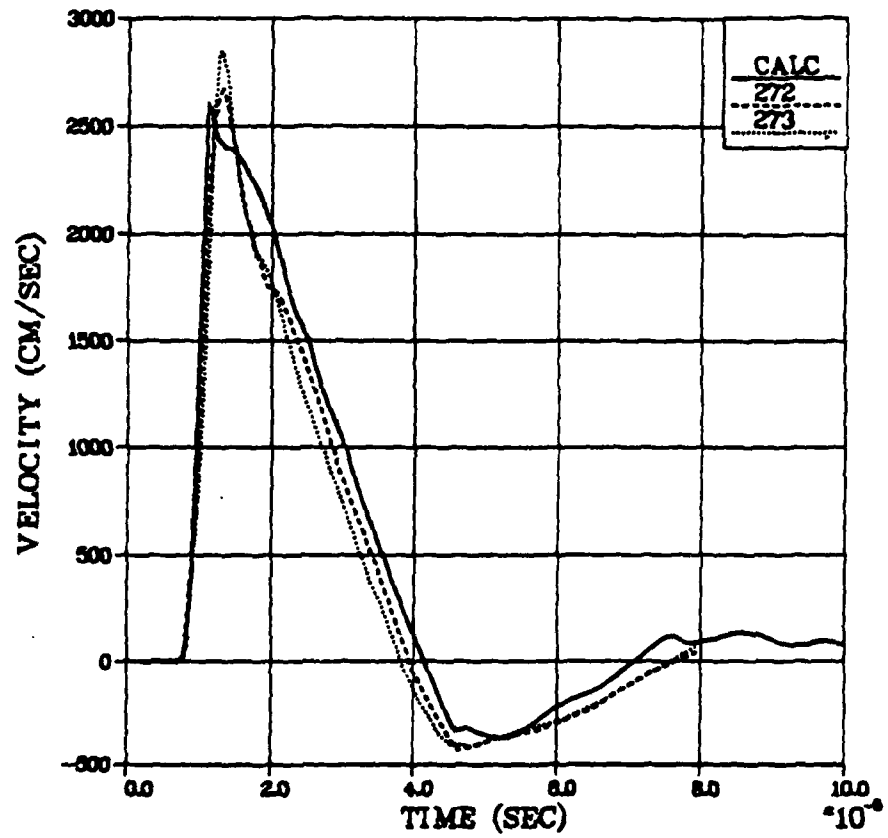


Figure 3.5. Comparison between measured velocities in 2C4 grout and best fit effective stress law calculation at 2.54 cm.

PV5 272  
PV5 273

R = 4.00 (CM)

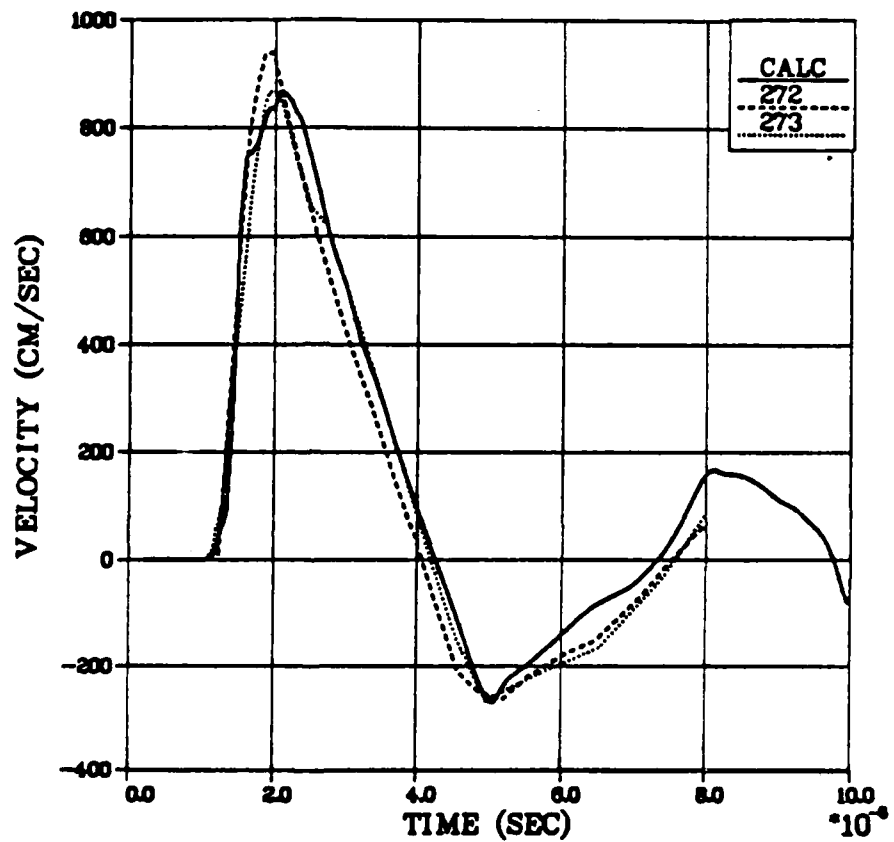


Figure 3.6. Comparison between measured velocities in 2C4 grout and best fit effective stress law calculation at 4.0 cm.



Figure 3.7 shows the residual stresses calculated using the effective stress model. These should be compared with the residual stresses calculated using the RDD models and shown in Figure 1.5. Peak hoop stresses occur at nearly the same radius and differ in magnitude by only 10 percent. In fact the major difference between the two is in the much smaller separation between hoop stress and radial stress near the cavity from the RDD calculation, due to the very low minimum damaged strength of 10 bars there.

It is gratifying that, although two very different constitutive models may be employed to match the particle velocity data, both give similar containment features such as residual stress fields and cavity radii. We believe that this shows the value of good particle velocity data as a discriminant of constitutive models for containment calculations. This velocity data led us to constitutive models which have three important features in common;

- (1) A strength higher than given by the laboratory static failure measurements needed to retard cavity growth and sufficiently narrow the positive velocity pulses. This is accomplished in the RDD constitutive models using strain rate dependent increases in strength and in the effective stress model by using a dry strength (zero pore fluid pressure).
- (2) A much lower strength after shock passage (pore crushup - shock damage) to provide a weaker central core of grout and therefore a wide negative pulse, accomplished using a damaged strength in the RDD models and a wet strength in the effective stress law.
- (3) A prescription for the reduction in strength from (1) to (2), i.e., the rate dependent Maxwell solid stress relaxation in the RDD models or the pore fluid buildup in the effective stress law.

## Skipper Stress Field 2C4

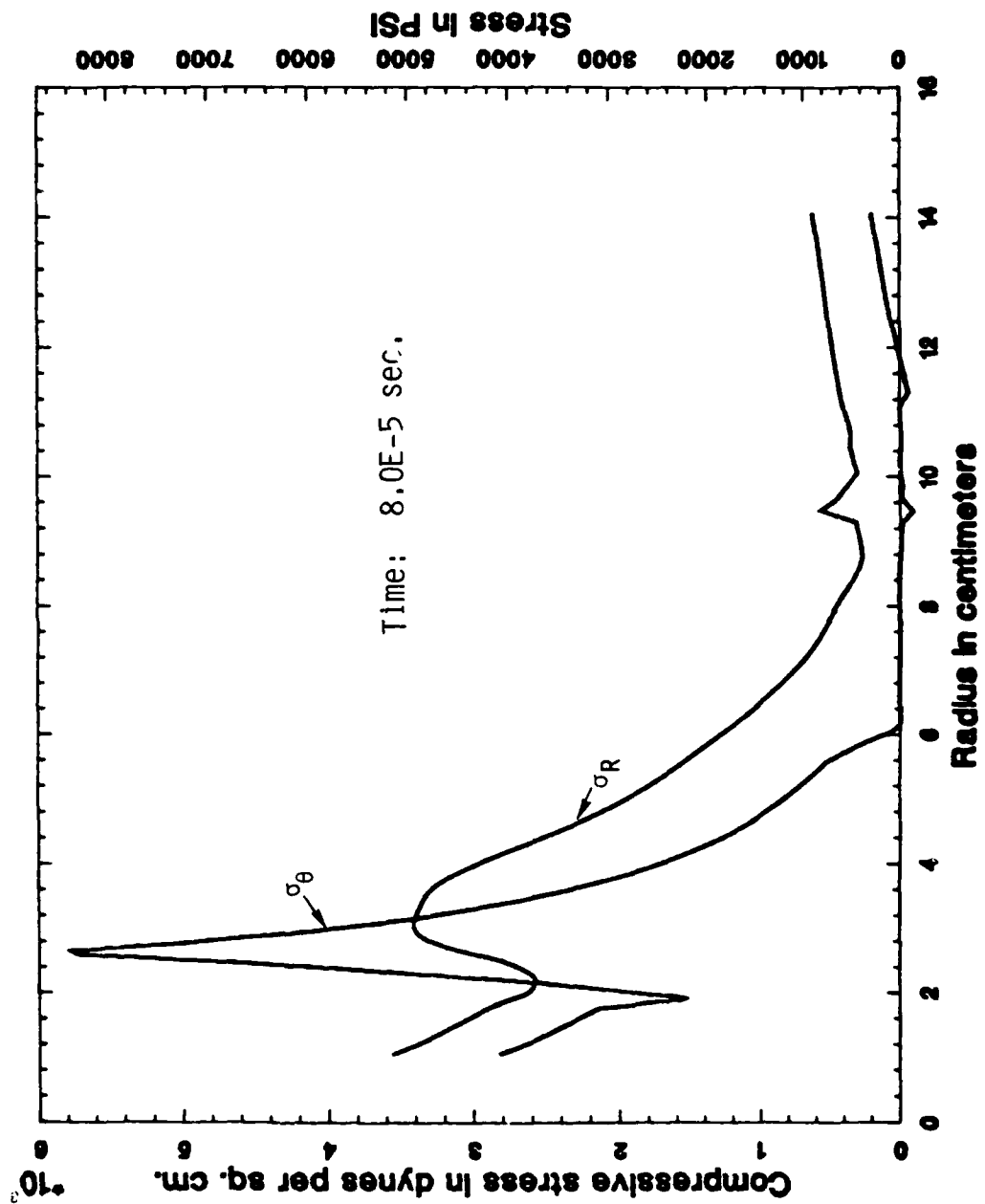


Figure 3.7. Calculated residual stresses in 2C4 grout at 80  $\mu\text{sec}$  using effective stress model.

NUMERICAL SIMULATION OF THE VELOCITY RECORDS FROM THE  
SRI GROUT SPHERES EXPERIMENTS(U) S-CUBED LA JOLLA CA  
N RIMER ET AL. 01 SEP 82 SSS-R-82-5580 DNA-TR-82-54  
DNA 0041-08-00000

2/2

DNA001-82-C-0043

F/G 20/11

NL

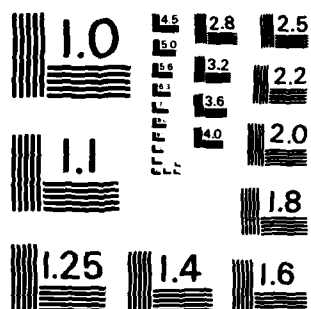
FND

DATE \_\_\_\_\_

6-01, 100-10

• • • • •

OTIC



MICROCOPY RESOLUTION TEST CHART  
NATIONAL BUREAU OF STANDARDS-1963-A

In the final analysis, the only way to develop a unique constitutive model is to obtain both stress and particle velocity measurements in the experiments. Nevertheless, a purely experimental test, based on the very different scaling properties of the two constitutive models presented here, can be made to determine the validity of one of the two models for the small scale grout spheres experiments. We propose such an experimental test in the next section.

### 3.3 A PROPOSED GROUT SPHERES SCALING EXPERIMENT

Since the effective stress model is rate independent, calculational results at one explosive yield (in spherical symmetry) may be simply scaled to any other yield using cube root of yield scaling of all distances and times. Therefore, a 2C4 grout test using a 3 gm charge of PETN (a factor of eight in yield) should give, for example, a particle velocity pulse at a range of 8.0 cm identical to the pulse at 4.0 cm from the 3/8 gm charge. Of course, all time durations in the velocity pulse for the larger yield should be stretched out a factor of two relative to the smaller yield.

For the rate dependent RDD models, however, simple scaling does not apply unless some of the "material properties" of the grout needed for these constitutive models are scaled as well. The relaxation time related  $\delta$  of 1.0  $\mu\text{sec}$  must be changed to 2  $\mu\text{sec}$  to scale for the example given above. Also, the strain rates for the larger charge would be expected to be a factor of two lower so that the coefficients defining the strain rate dependent increases in strength must be changed. Since it is totally unrealistic to have constitutive models with material properties which are dependent upon the external loading (excluding size effects, jointing, etc. for an inhomogeneous material macroscopically), we may assume that the calculational results using the RDD models do not simply scale.

An experimental test of the importance of these rate effects in the small scale grout spheres may allow us to choose between the two constitutive models. Therefore, we propose several 3 gm charge tests in 2C4 grout in the standard SRI configuration (to attain reproducible data). To insure scaling of the source, the thickness of the lucite (and homolite) shell should be made a factor of two larger as well. Particle velocity gauges should be emplaced at scaled ranges of 2.54, 3.80, 5.08, and 8.0 cm so that comparisons may be made with the standard 3/8 gm tests, one of which should be repeated with the same 2C4 grout batch as used in the 3 gm tests. If the scaled velocity pulses are the same, then rate dependent effects are not significant even for the high strain rates of these small scale tests. If these effects are not important here, they certainly should not matter at the much lower strain rates at the same scaled ranges in a nuclear test. However, if the experiments do not simply scale, this has important consequences for the future SRI tests on samples of Sandia ONE TON tuff.

Note that the proposed test is a purely experimental test of the importance of rate effects, requiring no assumptions about the validity of any particular constitutive model. We have, however, used the RDD constitutive models to predict the particle velocities at the scaled ranges listed above and so determined that the factor of eight in yield is sufficient to clearly see the rate effects as given by the model. Four finite difference calculations were made, investigating the effects of lucite thickness and calculational zone size on the scaling.

Figures 3.8-3.11 are our predicted particle velocities for the 3 gm test using the RDD constitutive models shown together with the measured velocities from the 3/8 gm tests simply scaled to 3 gm. We assumed that the proposed 3 gm tests would be detonated in the standard water tank so that arrivals from the water and the walls of the tank would contaminate the particle velocities much earlier in the pulse at the same scaled ranges. At the largest range of 8.0 cm, (Figure 3.8)

PV5 272  
PV5 273

R = 8.00 (CM)

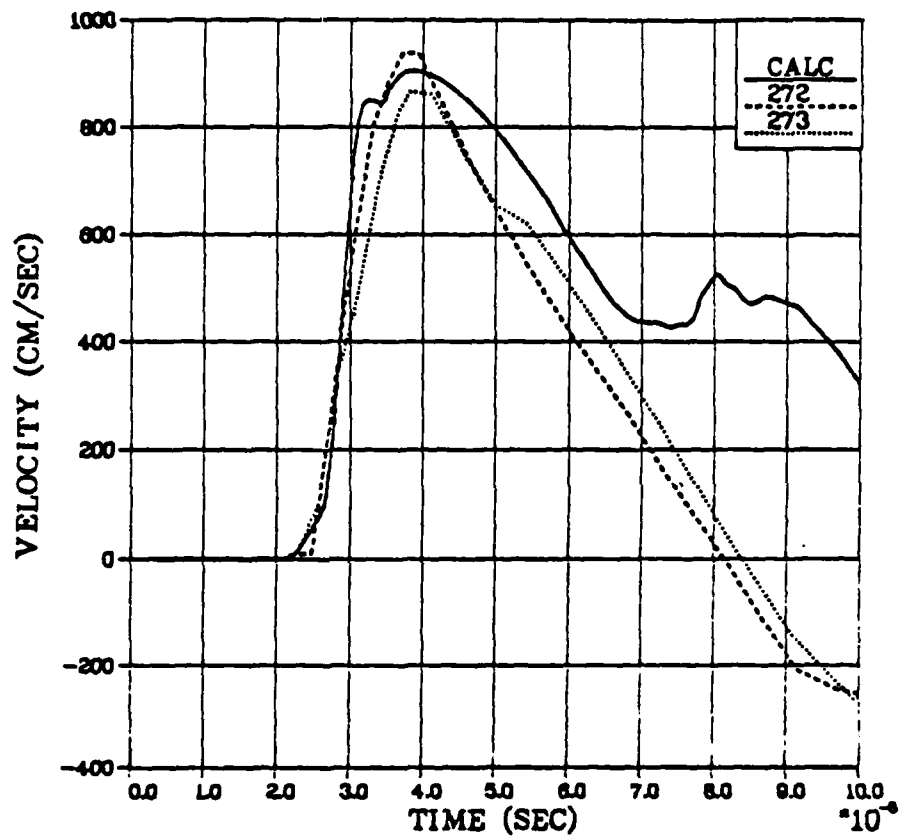


Figure 3.8. Predicted particle velocities at 8.0 cm for the proposed 3 gm charge test in 2C4 grout using the RDD models together with the measured velocities from the standard tests scaled to 3 gm.

PV 272  
PV 273

R = 5.08 (CM)

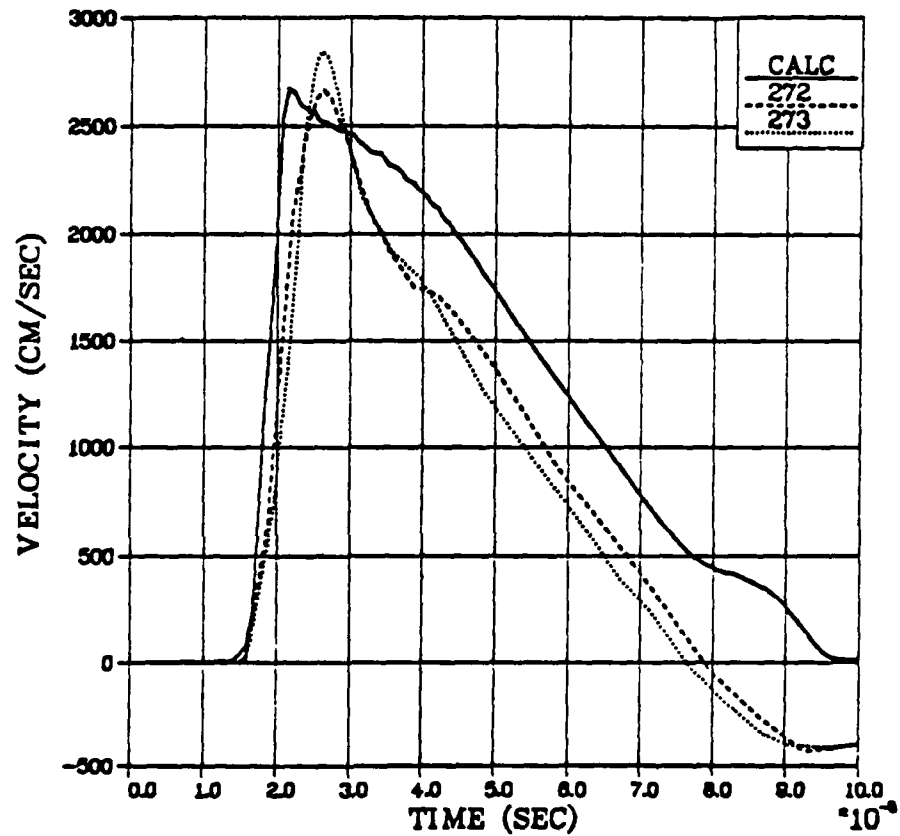


Figure 3.9. Predicted particle velocities at 5.08 cm for the proposed 3 gm charge test in 2C4 grout using the RDD models together with the measured velocities from the standard tests scaled to 3 gm.



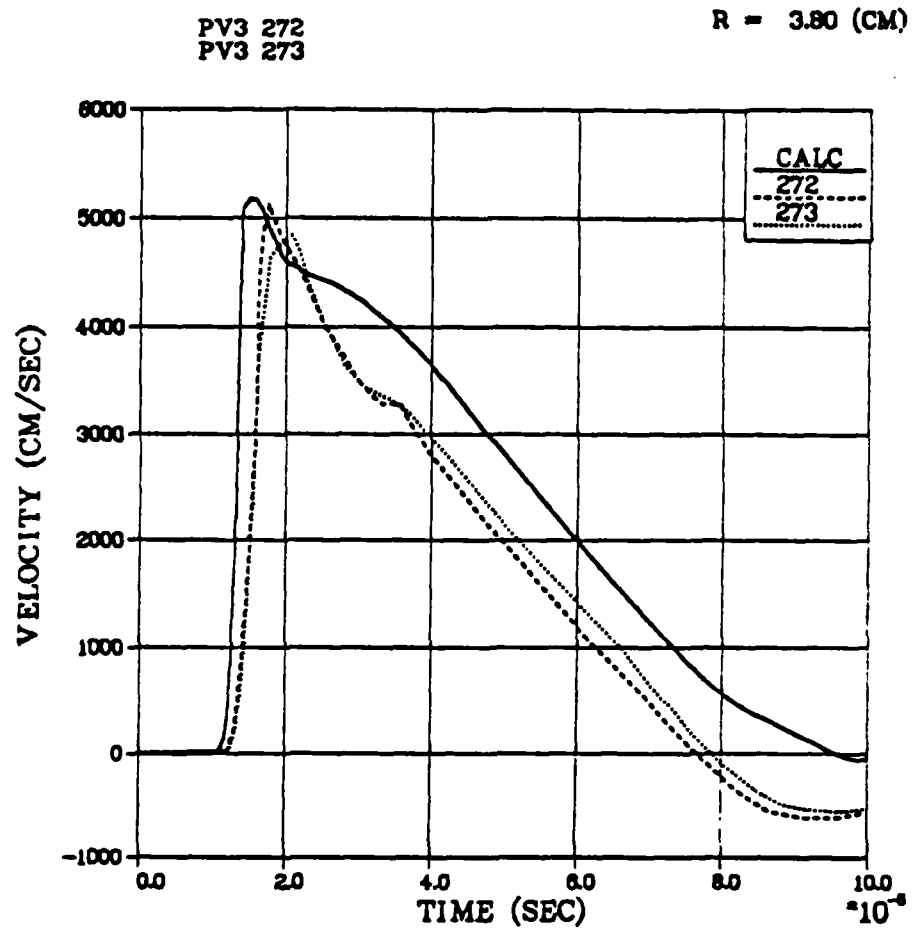


Figure 3.10. Predicted particle velocities at 3.80 cm for the proposed 3 gm charge test in 2C4 grout using the RDD models together with the measured velocities from the standard tests scaled to 3 gm.

PV2 273

R = 2.54 (CM)

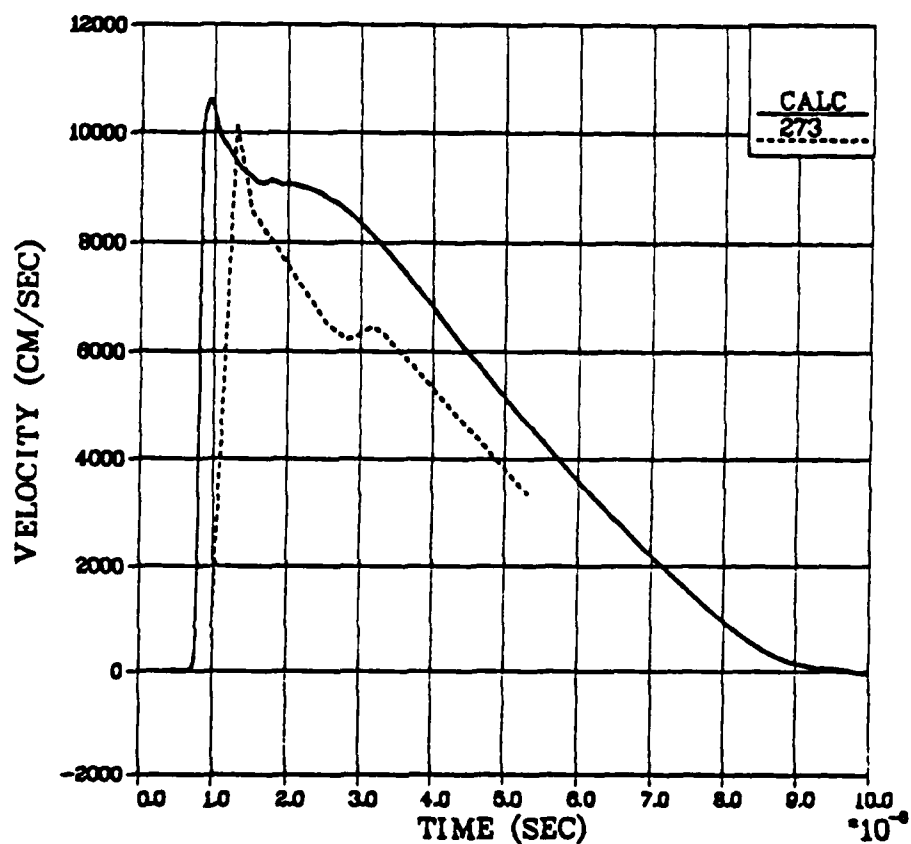


Figure 3.11. Predicted particle velocities at 2.54 cm for the proposed 3 gm charge test in 2C4 grout using the RDD models together with the measured velocities from the standard tests scaled to 3 gm.

the pulse is useful for comparison with the scaled measurements only to about 70  $\mu$ sec, while in closer the useful pulses last somewhat longer in time. Nevertheless, the calculated pulses certainly show the influence of rate effects when compared to either the measurements or to the RDD model calculations shown in Figures 1.1-1.4. Figures 3.9-3.10 in particular show calculated velocities that clearly differ from the simply scaled measurements by much more than the scatter of the measurements.

Tensile failure was noted in this calculation at a radius of 10-11 cm at approximately 50  $\mu$ sec, a result which very nearly scales from the standard 3/8 gm charge calculations. However, for the 3 gm charge, (unlike the standard configuration) tensile fractures propagated out to the outer radius of the grout sphere by a time of 60  $\mu$ sec. Thus, the sphere is unlikely to survive intact long enough for hydrofracture measurements to be made.

This finite difference calculation was made assuming that the thickness of the lucite and homolite shell around the charge was doubled from the standard configuration. Grid zone sizes in the grout for this calculation were not scaled from the standard configuration but rather were replaced if they were within the larger initial radius of the lucite. We repeated this calculation, simply scaling up the rate dependent material properties so that the results should scale from the best fit simulations of Figure 1.1-1.4 if the different grid zoning had no influence. Figures 3.12-3.15 show the results of this calculation with scaled material properties. Except for a slight increase in peak velocities, the results agree well with Figures 1.1-1.4 (scaled) until arrivals from the water tank contaminate the pulses.

The lucite thickness does significantly effect the velocity pulses. Figure 3.16 shows the results of a calculation again scaling material properties to remove rate dependence but using the original lucite thickness. Comparison with Figure 3.13 at the same range shows

PV2 273

R = 2.54 (CM)

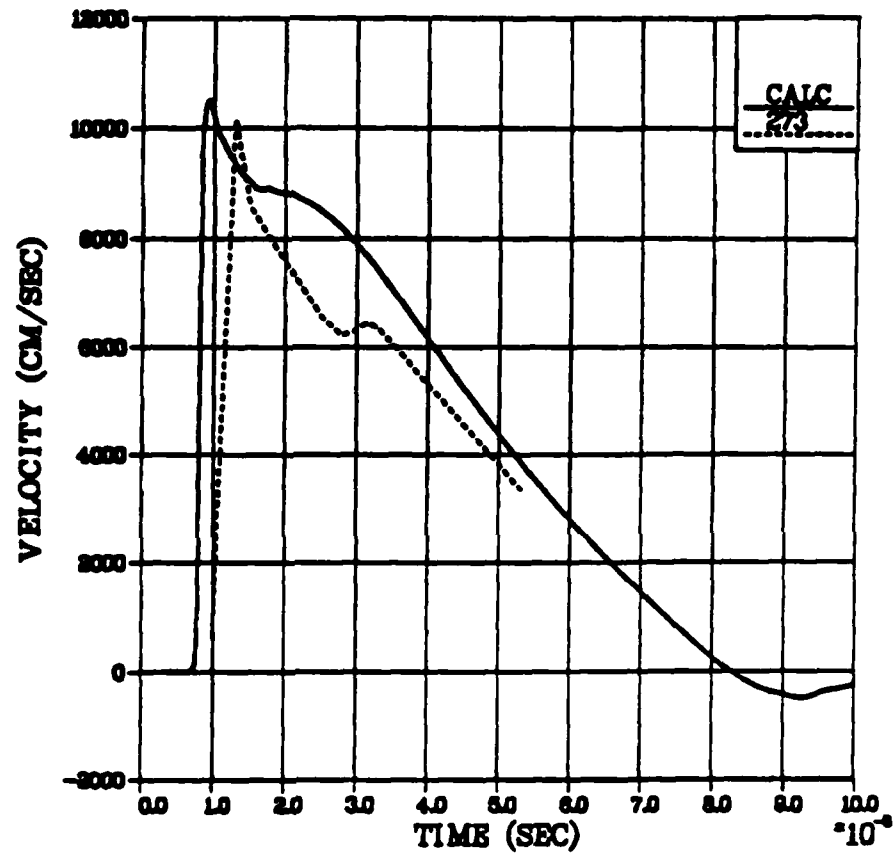


Figure 3.12. Calculated particle velocities at 2.54 cm for the proposed 3 gm charge in 2C4 grout using the RDD constitutive models with scaled material properties. Measured velocities from the standard 3/8 gm tests are shown scaled to 3 gms for comparison.

PV3 272  
PV3 273

R = 3.80 (CM)

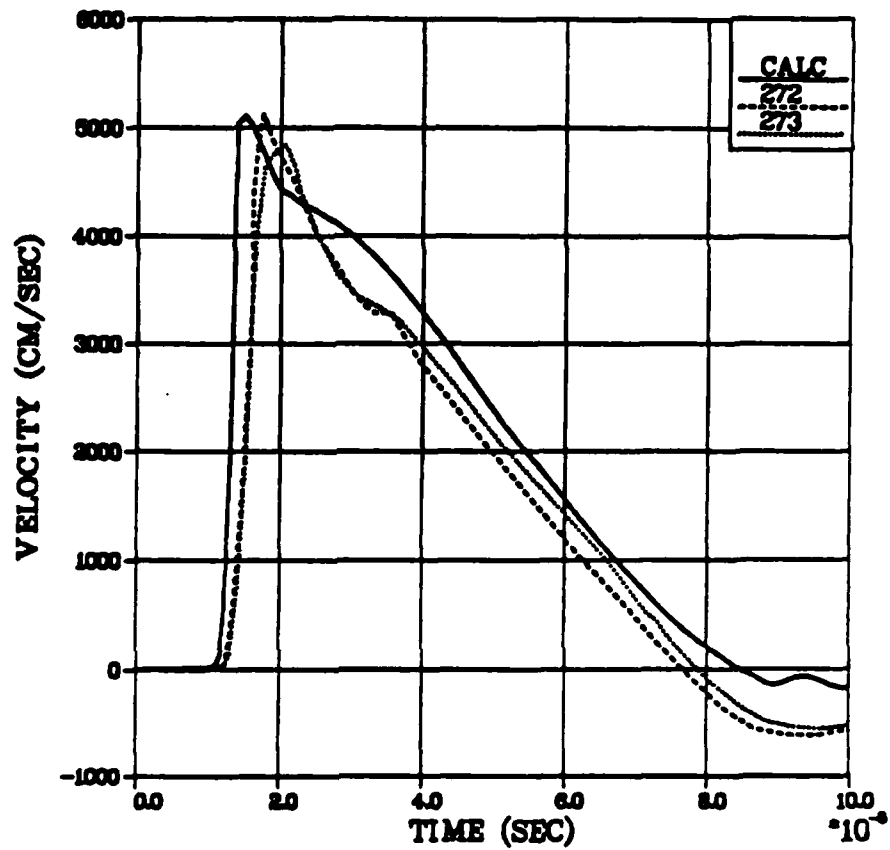


Figure 3.13. Calculated particle velocities at 3.80 cm for the proposed 3 gm charge in 2C4 grout using the RDD constitutive models with scaled material properties. Measured velocities from the standard 3/8 gm tests are shown scaled to 3 gms for comparison.

PW 272  
PW 273

R = 5.08 (CM)

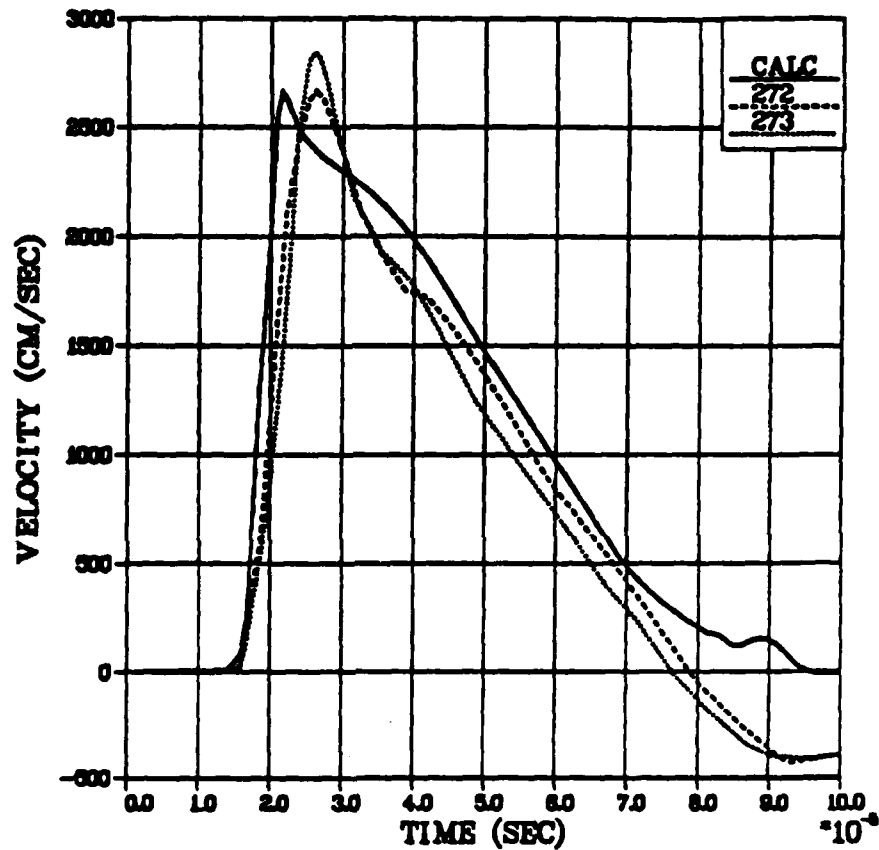


Figure 3.14. Calculated particle velocities at 5.08 cm for the proposed 3 gm charge in 2C4 grout using the RDD constitutive models with scaled material properties. Measured velocities from the standard 3/8 gm tests are shown scaled to 3 gms for comparison.

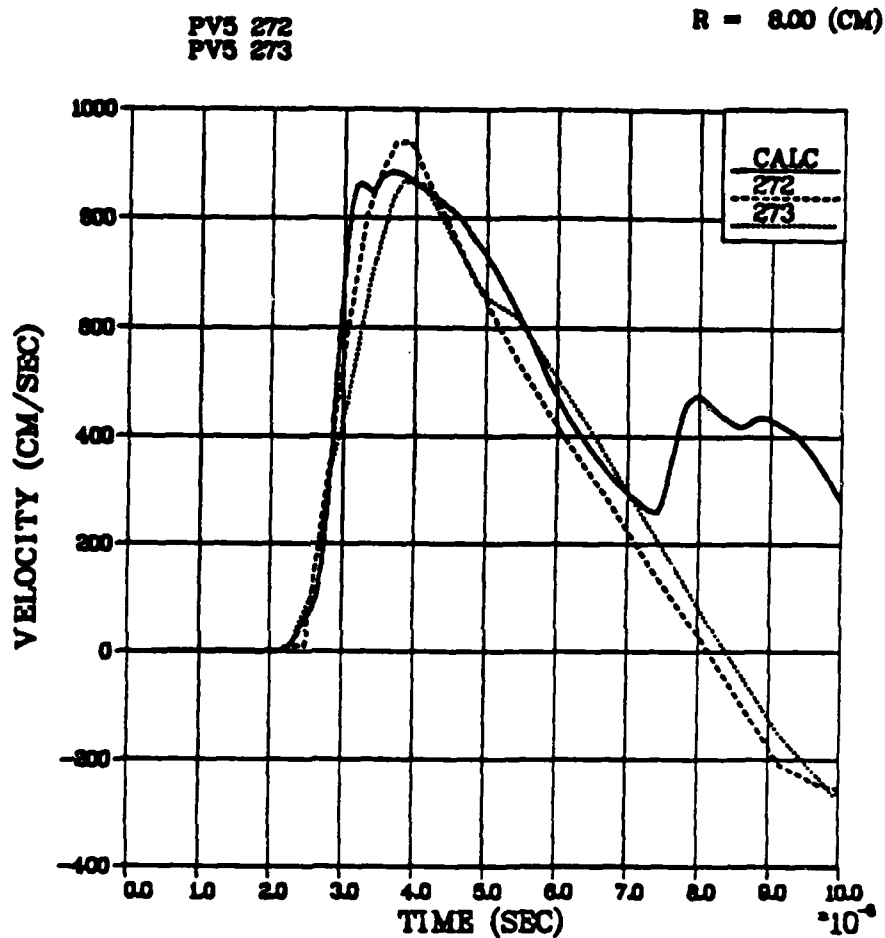


Figure 3.15. Calculated particle velocities at 8.0 cm for the proposed 3 gm charge in 2C4 grout using the RDD constitutive models with scaled material properties. Measured velocities from the standard 3/8 gm tests are shown scaled to 3 gms for comparison.

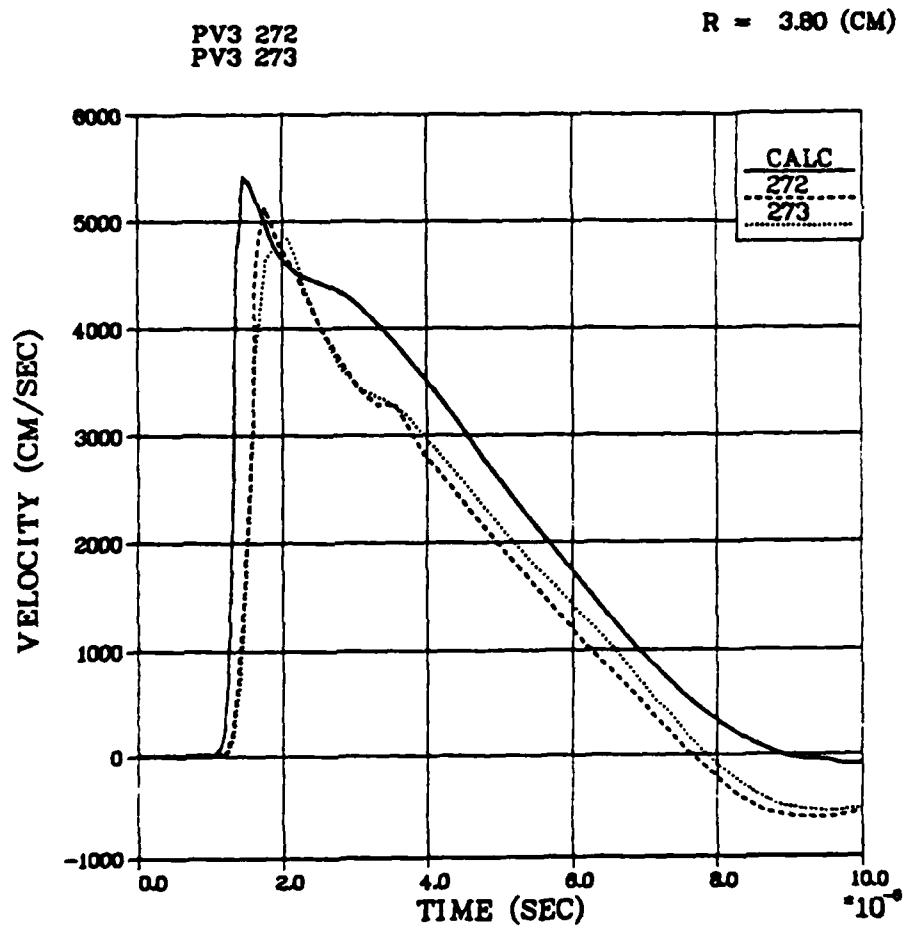


Figure 3.16. Calculated particle velocities at 3.80 cm for the 3 gm charge in 2C4 grout using the RDD constitutive models with scaled material properties and the same lucite thickness as the standard 3/8 gm tests.



higher peak velocity and a wider pulse when less lucite is available to attenuate the explosive. Figure 3.17 shows calculated velocities at the same range for the thin lucite case, this time without scaling up material properties. Comparison with Figure 3.10 (the predicted velocities for the proposed test) again indicates larger peak velocity and a wider pulse. We therefore recommend that the lucite case and surrounding epoxy should be exactly doubled in thickness for the proposed 3 gm tests.

PV3 272  
PV3 273

R = 3.80 (CM)

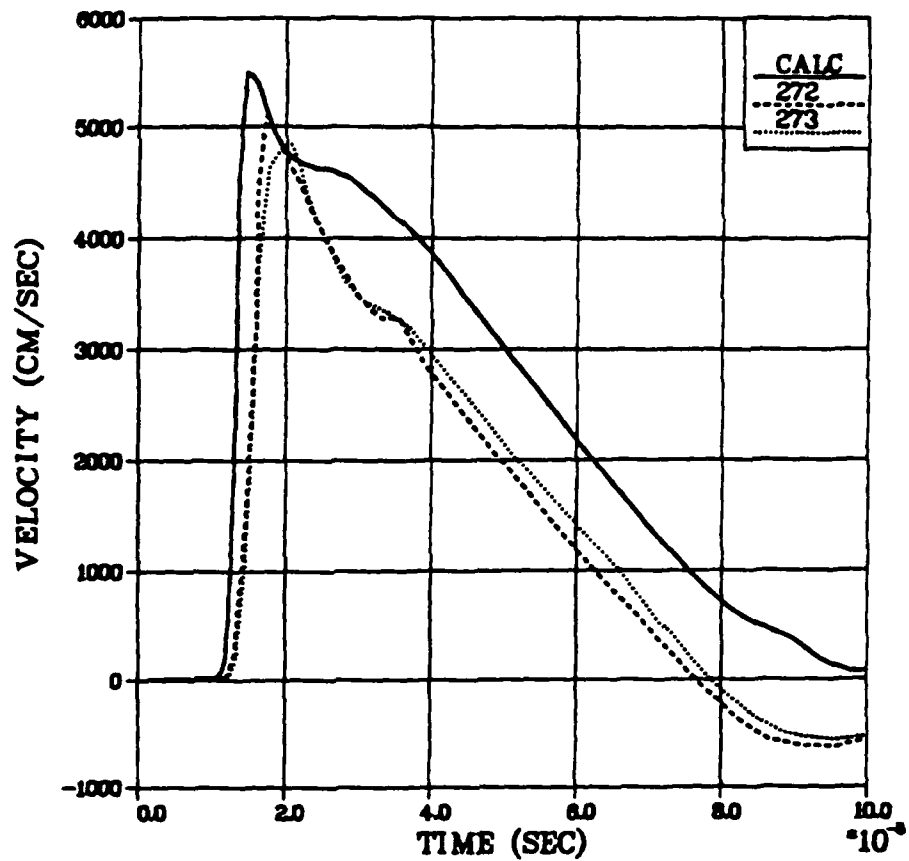


Figure 3.17. Calculated particle velocities at 3.80 cm for the 3 gm charge in 2C4 grout using the RDD constitutive models and the same lucite thickness as the standard 3/8 gm tests.

#### SECTION 4

##### CONSTITUTIVE MODELS FOR HIGH POROSITY LD2C4 GROUT

The low density, high air-filled porosity grout (LD2C4), intended to simulate porous alluvium, was made at SRI by blending approximately the standard 2C4 rock-matching grout mix with a specified amount of Q-CEL microspheres which encapsulate air in hollow spherical shells derived from inorganic silicate. Cizek and Florence (Reference 13) reported physical properties measurements for this grout which indicate 13.4 percent air-filled porosity and slightly lower unconfined strength and wave speeds than for 2C4 grout.

The LD2C4 grout was hydrofractured from the explosively formed cavities as well as from unexploded (cast) spherical cavities. The measured fracture initiation pressures from the exploded configuration showed no increase when compared with fracture initiation pressures from the unexploded configuration, indicating that the compressive residual stress fields around the dynamically formed cavities were negligible at the time of hydrofracture. This result may be interpreted either as indicating that no significant compressive residual stress fields are explosively formed in this high porosity material or that the residual stress fields formed around the cavity decay rapidly with time. In either case, the experimental result brings into question the residual stress concept as a containment mechanism for the hot cavity gases from nuclear events in high porosity materials such as alluvium, with the caveat that the peculiar structure of the air-voids in LD2C4 grout may make this material a poor simulant of alluvium.

In order to provide reproducible data so that a numerical constitutive model for LD2C4 grout may be validated to calculate residual stress fields around the explosively formed cavities for comparison with the hydrofracture results, Cizek and Florence (Reference 6) have measured particle velocities in LD2C4 from standard 3/8 gm PETN explosive charges. Here we discuss successful simulations of the LD2C4

particle velocity data using both the RDD and effective stress constitutive models. We begin with a description of the laboratory material properties data for LD2C4 and of the detailed material properties needed for the calculation of particle velocities and residual stress fields using the RDD models. (The simulated velocities have been shown in Figures 1.6-1.10.)

Laboratory measurements of the pressure-volume response of LD2C4 (the crush curve) were not available until later so that a dynamic crush curve was backed out from the particle velocity data. The sensitivity of the calculated particle velocity records to not easily measured details of the crush curve is discussed in detail. Subsequent laboratory measurements of the air void crush-up at Terra Tek (Reference 7) are described which are in excellent agreement with the crush curve derived from the particle velocity data.

#### 4.1 MATERIAL PROPERTIES FOR LD2C4 GROUT

The rate and damage dependent (RDD) constitutive models described in Section 2.5 require a number of "material properties" (relaxation times, damage parameters, strain rate dependent strength increases, etc.) not easily measured in the laboratory in addition to the usual set of material properties (physical properties, air void crushup, wave speeds, strength). Table 4.1 gives the more standard material properties used for the "best fit" RDD model simulation of the LD2C4 particle velocity data (Figures 1.6-1.10), together with the SRI material properties measurements from which they were derived. Also given in Table 4.1 are the material properties measurements at Terra Tek (Reference 7), made available after the numerical simulations had been completed. The only major difference between the SRI measurements and the material properties used in the calculations is in the choice of Poisson's ratio which impacts the bulk and shear moduli and the shear wave speed. This will be discussed later.

The P- $\alpha$  porous rock crushup model discussed in Section 2.3 with a polynomial equation of state was used to describe the pressure-

TABLE 4.1. MATERIAL PROPERTIES FOR LD2C4 GROUT

Property	Calculation	Measurements	
	RDD Model (Best Fit)	SRI	Terra Tek
Density (gm/cc)	1.921	1.9	1.86
Air-filled porosity (%)	13.4	13.4	13
Bulk Modulus (Kb)	120	104	117
Shear Modulus (Kb)	51	59	55
Longitudinal Wave Speed (m/s)	3129	3130	3210
Shear Wave Speed (m/s)	1629	1780	1730
Poisson's ratio	0.314	0.26	0.295
Maximum stress difference (Kb)	0.22	-	0.25-0.28
Unconfined compressive strength (Kb)			
Static	0.22	0.218	0.22-0.23
At strain rate of 0.15 sec <sup>-1</sup>	0.29	0.34	-
Tensile strength from Brazil Test (Kb)			
Static	0.031	0.031	-
At strain rate of 0.15 sec <sup>-1</sup>	0.06	0.053	

volume behavior of a rock element. In the absence of laboratory load-unload data to characterize the void crushup of LD2C4 grout a parameter study was made to examine the influence of the shape of the crush curve on the particle velocity pulses. This resulted in the crush curve shown in Figure 1.11 (the solid curve) in which the pressure of the material without voids (the unload curve) is given by

$$P_n = 202 \mu + 288 \mu^2 \text{ (Kb)}$$

which is the identical expression used for 2C4 grout. The later uniaxial strain load-unload data from Terra Tek (Reference 7) shown dotted in Figure 1.11 agreed very well with our derived crush curve.

For the RDD model calculation, the static failure surface for undamaged LD2C4 grout was chosen to give good agreement with the measured unconfined compressive strength and tensile strengths. A maximum stress difference of 0.22 Kb, equal to the unconfined strength, was used in the absence of laboratory data. Later measurements at Terra Tek indicated that 10 to 25 percent higher values are more appropriate.

As for 2C4 grout, for strain rates greater than  $0.001 \text{ sec}^{-1}$  strain rate dependent increases in strength are imposed upon the static failure surface, giving

$$Y = 0.055 f_1 + 1.5 f_2 \bar{P} \text{ (Kb)}$$

$$Y_{\max} = 0.22 f_3 \text{ (Kb)}$$

where

$$\begin{aligned} f_1 &= 1 + 0.20 \bar{\epsilon} \\ f_2 &= 1 - 0.424 \bar{\epsilon} \\ f_3 &= 1 + 0.20 \bar{\epsilon} \end{aligned}$$

and

$$\bar{\epsilon} = \log_{10} (\text{radial strain rate}/0.001)$$

All damage and relaxation phenomena are normalized through the choice of  $V_c$ , the reference specific volume, which, as described in Section 2.5, determines the dependence of the damage function  $f_R$  upon peak pressure and therefore the size of the damaged central core. The best match to the particle velocity data from LD2C4 grout occurs when  $V_c$  corresponds to the 0.6 Kb pressure level in the solid crush curve of Figure 1.11.

The damaged strength,  $Y_R$ , at  $V_c$  is defined by

$$Y_R = 0.022 + 1.5 \bar{P} \quad (\text{Kb})$$

$$Y_{R_{\max}} = 0.10 \quad (\text{Kb})$$

Further reduction in  $Y_R$  is allowed until a minimum strength of 0.01 Kb is reached. Maxwell solid deviatoric stress relaxation to the damaged strength  $Y_R$  is controlled by the time relaxation coefficient  $\delta$ , set equal to 0.5  $\mu\text{sec}$ . Use of a higher  $Y_{\max}$ , as given by the Terra Tek measurements of Table 2.1 would necessitate a slightly smaller  $\delta$  to match the velocity pulse widths for LD2C4. Once again, deviatoric stress relaxation is not permitted until shock loading has been completed.

Shear modulus is assumed to decrease linearly with damage from 51 Kb down to 10 Kb as  $f_R$  increases to 1.0 (at  $V_c$ ). Continued reduction is allowed for larger  $f_R$  until a minimum shear modulus of 5 Kb is reached.

The "best fit" results of Figures 1.6-1.10 are relatively insensitive to small changes in some of the above material properties. In particular, shape of the velocity pulses is not changed by strength variations ( $Y_{\max}$ ,  $\delta$ ). However increased strength (or increased  $\delta$ ) does narrow the pulses and reduces peak velocities slightly. Once the reference specific volume  $V_c$  was normalized, the velocity pulses were found to be most sensitive to small details of the crush curve.

#### 4.2 THE INFLUENCE OF CRUSH CURVE UPON PARTICLE VELOCITY

Figure 1.11, the crush curve for LD2C4 grout developed using the RDD constitutive models, has the characteristic shape expected for dry, porous alluvium, i.e., a flat portion in which the bulk of the air-filled porosity is crushed up at relatively low pressures and a steeper position in which the spherical pores of the matrix material (tuff, paleozoic, etc.) are removed. For LD2C4, there is photographic evidence of some uncrushed microballoons posttest. However, we believe that the bulk of the microballoons are crushed up by 0.6–1.0 Kb. Contrast the LD2C4 crush curve with that of the 2C4 grout (Figure 2.2), characteristic of saturated tuff, in which the flat portion is probably not present under overburden pressure. (Some laboratory core samples do show a flat portion at low pressures which probably represents easily crushed crack porosity due to removal of the overburden). Velocity pulses in the high porosity grout are characterized by a precursor shape which is very sensitive to details of the low pressure crushup.

The major difference between 2C4 and LD2C4 is in the more rapid attenuation of peak velocity and stress with range for the high porosity grout. In Figure 1.11, arrows indicate the approximate values of peak pressure calculated at the four gauge locations (1.27, 1.90, 2.54, and 4.0 cm.) At station 1 (1.27 cm), where peak pressure is greater than 2.0 Kb, the velocity pulse does not depend on the shape of the crush curve at low pressures. In this respect, the results at station 1 for LD2C4 are similar to the results for 2C4 grout at all four stations. (At station 4 for 2C4 grout, where peak stress is 0.55 Kb, and peak pressure is 0.25 Kb, peak velocity may be changed slightly by altering the shape of the crush curve of Figure 2.2). The peak stress at station 1 for 2C4 is calculated to be about 6 Kb. However, the peak velocity at station 1 for LD2C4 is greater than for 2C4 due to the lower dynamic strength used for LD2C4. At all other stations, peak velocity is much lower for LD2C4 and occurs along the relative flat portion of the crush curve. At station 4, the peak velocity occurs at a pressure of only 110 bars, just above the assumed elastic knee of the crush curve at 100 bars. The assumption of



an elastic pressure, slightly greater than the applied overburden of 69 bars, is a calculational convenience that may not be realistic.

At stations 2-4, the velocity pulses for LD2C4 are very dependent upon the shape of the crush curve, particularly the shape near where peak loading occurs for the station. As an example, consider the dotted curve of Figure 1.11, approximating the Terra Tek uniaxial strain load-unload (Reference 7), which differed significantly from the crush curve derived from the velocity data only between 0.4 and 0.8 Kb. Figures 4.1-4.4 show the particle velocities calculated with the RDD models using the measured crush curve. For these calculations, the reference specific volume  $V_c$  which controls damage and stress relaxation was not changed. However it is reached at 0.46 Kb rather than 0.6 Kb for the "best fit" simulation shown in Figure 1.6-1.9.

At 1.27 cm, the velocity pulse is almost identical to Figure 1.6. However, at 1.90 cm (station 2), peak velocity is 6 percent lower due to the greater attenuation at these stress levels. At 2.54 cm, (station 3), peak velocity is about 6 percent lower because of the closer-in attenuations, even though the crush curve is unchanged at these stress levels. The simulations using this measured crush curve are overall in slightly better agreement with the measured velocities. Note that the precursors at all four stations, which are controlled by details of the low pressure portion of the crush curve, are the same for both simulations. At station 4, the peak velocity is at the precursor.

For our numerical simulations, the crush (loading) curve is represented by a series of data points (pressure vs. specific volume) with corresponding values of  $\alpha$ . Linear interpolation is used to determine loading states between data points. The smoothness of the calculated velocity pulses is somewhat dependent upon the number of data points chosen. Table 4.2 lists the crush curve points used for the "best fit" simulation of Figures 1.6-1.9 and the two changes in this data set made to represent the later laboratory measurements at Terra Tek in the simulation of Figures 4.1-4.4.

TABLE 4.2. CRUSH CURVES FOR LD2C4 GROUT

<u>Best Fit</u>					
Point	Pressure (Kb)	Specific Volume (cc/gm)			
1	4.0	0.44253134			
2	3.5	0.44375			
3	3.0	0.4450			
4	2.5	0.4463			
5	2.0	0.4478			
6	1.5	0.4494			
7	1.0	0.4511	Changes for Measured Curve		
8	0.8	0.4530	<u>Pt.</u>	<u>P</u>	<u>V</u>
9	0.6	0.4650 ( $V_c$ )	{	9	0.6 0.4552
10	0.4	0.4800		9a	0.46 0.4650 ( $V_c$ )
11	0.21	0.5180			
12	0.15	0.5201			
13	0.10	0.52042045 ( $V_e$ )			
14	0.0	0.5208545 ( $V_o$ )			

PV2 297  
PV2 288

R = 1.27 (CM)

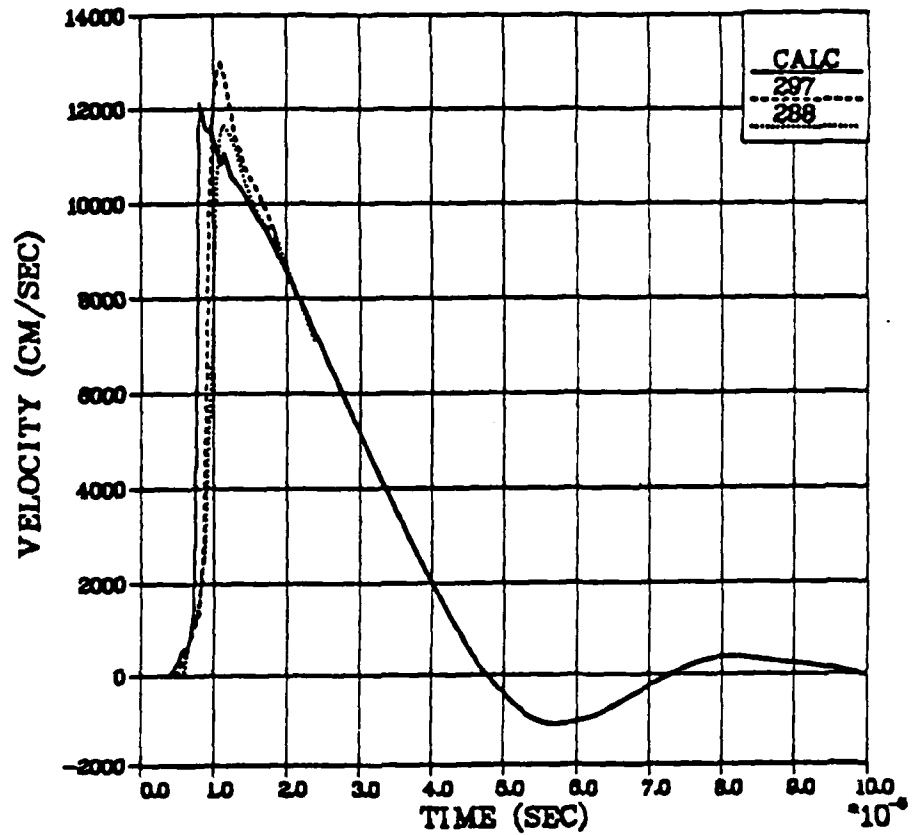


Figure 4.1. Comparison between measured particle velocities at 1.27 cm in LD2C4 grout and a calculation using the RDD constitutive models and the measured crush curve.

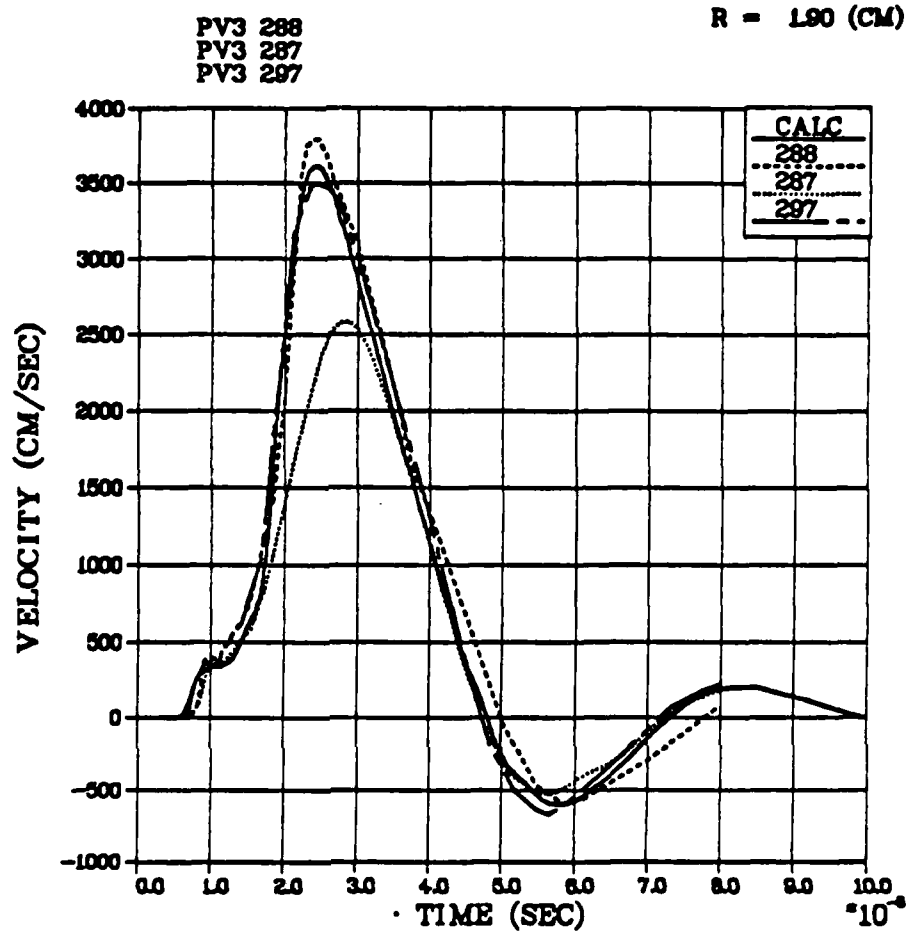


Figure 4.2. Comparison between measured particle velocities at 1.90 cm in LD2C4 grout and a calculation using the RDD constitutive models and the measured crush curve.

PW 288  
PW 297

R = 2.54 (CM)

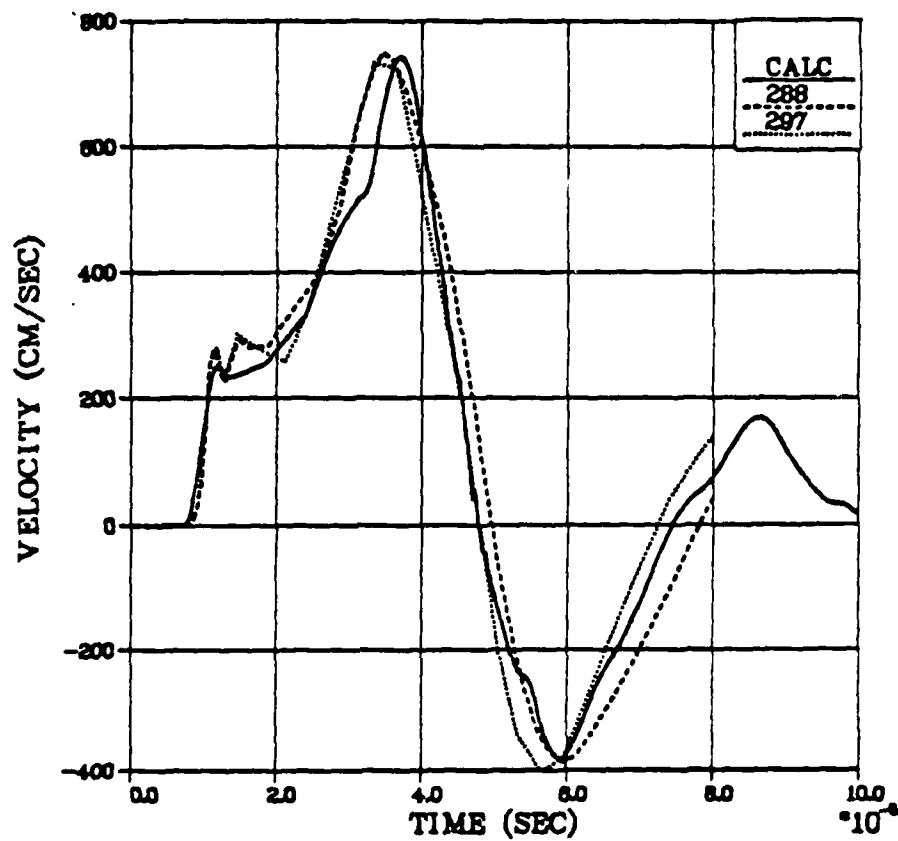


Figure 4.3. Comparison between measured particle velocities at 2.54 cm in LD2C4 grout and a calculation using the RDD constitutive models and the measured crush curve.

PV5 287  
PV5 297

R = 4.00 (CM)

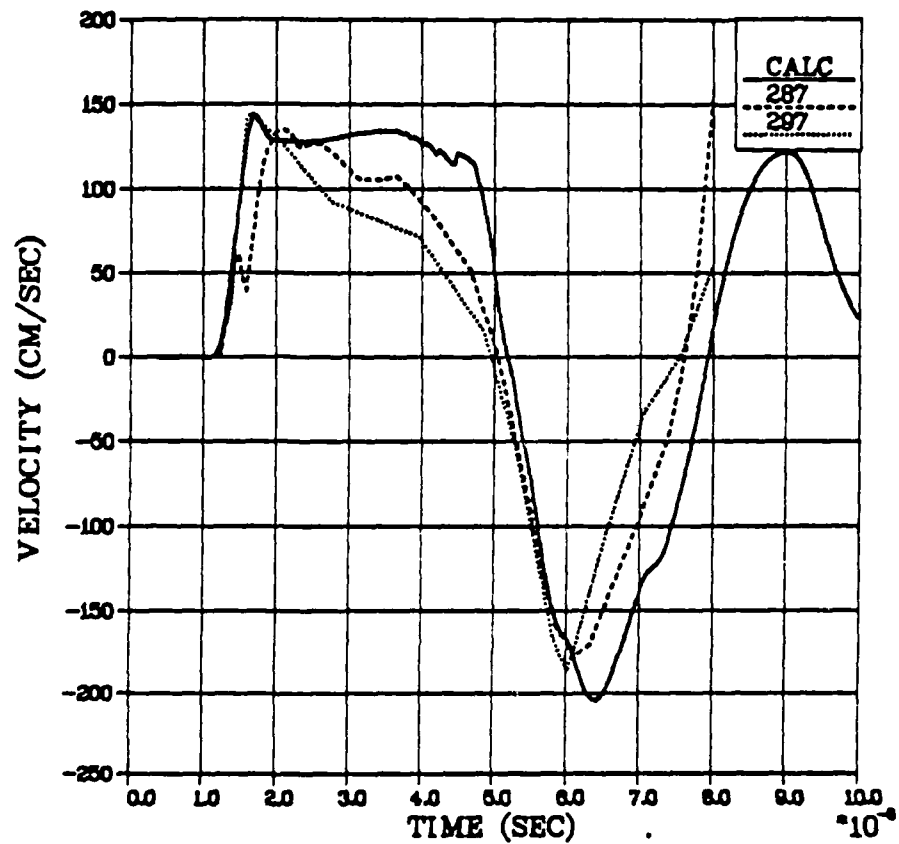


Figure 4.4. Comparison between measured particle velocities at 4.0 cm in LD2C4 grout and a calculation using the RDD constitutive models and the measured crush curve.

Table 4.2 will be used to show the influence of crush curve shape and, in particular, the low pressure end of the crush curve, upon different features of the particle velocity pulses. We have already given an example of how a change in shape at higher pressures (specifically a lowering of the crush curve to give more void crush up at 0.6 Kb) can influence peak velocities behind the precursor. In this discussion, we will concentrate on the velocity pulse at 2.54 cm where because of their relative magnitudes, changes in both the precursor and velocity peak are easily visible.

Figure 4.5 shows the particle velocity at 2.54 cm from a calculation using the "best fit" crush curve of Table 4.2, but with 20 percent higher strain rate dependent increases in strength. When compared with Figure 1.8, we note the narrower positive pulse and slightly higher peak velocity and precursor velocity. We emphasize again that strength increases, while primarily narrowing pulses, do, in general, decrease peak velocities. However, at individual stations where stress levels are low, such as shown in Figure 4.5, the complex interactions between void crushup effects and yielding during loading sometimes result in slightly higher velocities. At stations 1 and 2 in the calculation, peak velocities were lower than for the "best fit" results.

In Figure 4.5, we have labeled three points of interest on the velocity pulse at 2.54 cm. Points 11 and 12 correspond to crush curve points 11 and 12 of Table 4.2 and point Y is where yielding occurs for the first time at this location. The effects of yielding and of loading to a lower slope in the crush curve are similar, both result in an increased slope in the velocity pulse. The slopes of segments Y-12, 12-11, and 11-peak velocity in Figure 4.5 are controlled by the respective slopes in the loading curve. The precursor velocity is reached somewhere between points 12 and 13 on the loading curve and is controlled largely by the elastic constants of the grout (bulk modulus, shear modulus) and by the slope between points 12 and 13. Reduction of the elastic pressure (point 13 in Table 4.2) by itself does not significantly change the precursor velocity if the slope between points 12 and 13 is maintained constant.

PW 288  
PW 297

R = 2.54 (CM)

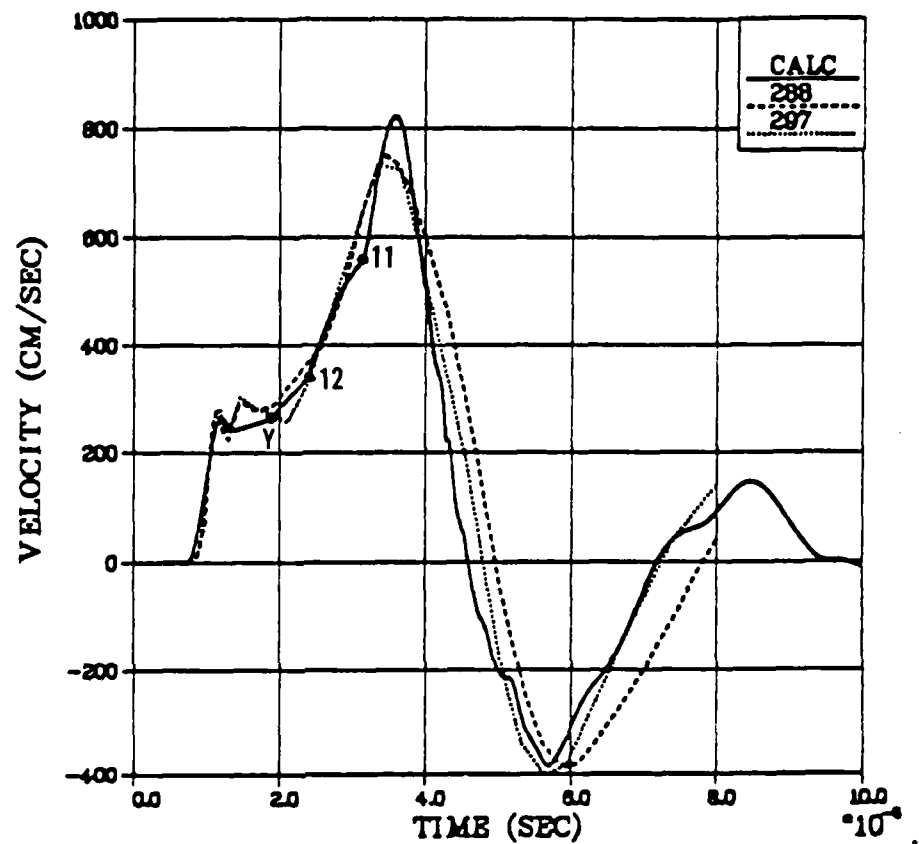


Figure 4.5. Comparison between measured particle velocities at 2.54 cm in LD2C4 grout and a calculation using the RDD constitutive models and "best fit" crush curve (Table 4.2) with 20 percent higher values of strain rate coefficients  $f_1$  and  $f_3$ . Points 11 and 12 refer to the crush curve and point Y to where yielding first occurs.



If the undamaged shear modulus of the grout is increased (from 51 Kb) while maintaining the longitudinal wave speed constant, i.e., reducing the bulk modulus and, therefore, the slope of the loading curve between points 13 and 14, the precursor velocity is reduced even if the slope between points 12 and 13 is maintained. This tends to reduce the magnitudes of the entire positive velocity pulses at 2.54 and 4.0 cm. Shear modulus increases also result in narrower pulses at all four stations.

Figure 4.6 shows another example of a crush curve variation influencing the velocity at 2.54 cm. For this calculation, the pressure at point 10 was lowered from 0.40 to 0.35 Kb, (in Figure 1.11, the slope corresponding to station 3 (2.54 cm) is lowered), while all the other pressures and specific volumes and material properties remained the same as in Table 4.2 and Figure 4.5. This resulted in a general attenuation of the velocity pulse in Figure 4.6 when compared to Figure 4.5 and a similar attenuation at station 4 (4.0 cm).

Changes in pressure still further down the crush curve are examined in Figure 4.7. For this calculation, all values are identical to those of Figure 4.6 except that point 11 of the crush curve has been raised from 0.21 Kb to 0.22 Kb, resulting in less attenuation below this pressure value (a steeper initial slope between points 11 and 12 in Figure 4.7) and considerably more attenuation above point 11, resulting in a lower peak velocity at 2.54 cm. If this pressure was raised still further, to 0.25 Kb, the slope of the velocity pulse would become still steeper near point 12, which would now be pushed to an earlier time, giving far less agreement with the measurements. Even more interesting, the peak velocity at 2.54 cm would be lower and would lie between points 11 and 12, never reaching the more attenuating portion of the crush curve. Figure 4.8 shows an example of this for slightly different material properties. Figure 4.9 shows the effect of lowering point 11 to 0.20 Kb. The final choice of 0.21 Kb, i.e., Figure 4.6, was a compromise between Figures 4.7 and 4.9.

PW 288  
PW 297

R = 2.54 (CM)

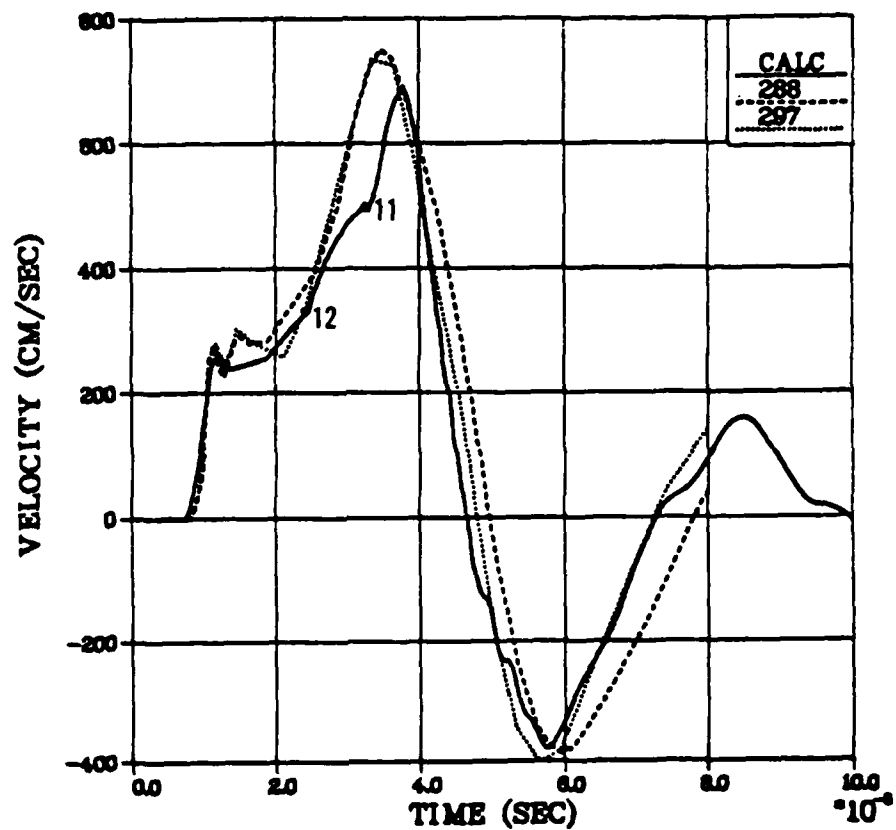


Figure 4.6. Comparison between measured particle velocities at 2.54 cm in LD2C4 grout and a calculation using the RDD constitutive models showing the effect of reducing the pressure from 0.40 Kb to 0.35 Kb at point 10 of Table 4.2.

PW 288  
PW 297

R = 2.54 (CM)

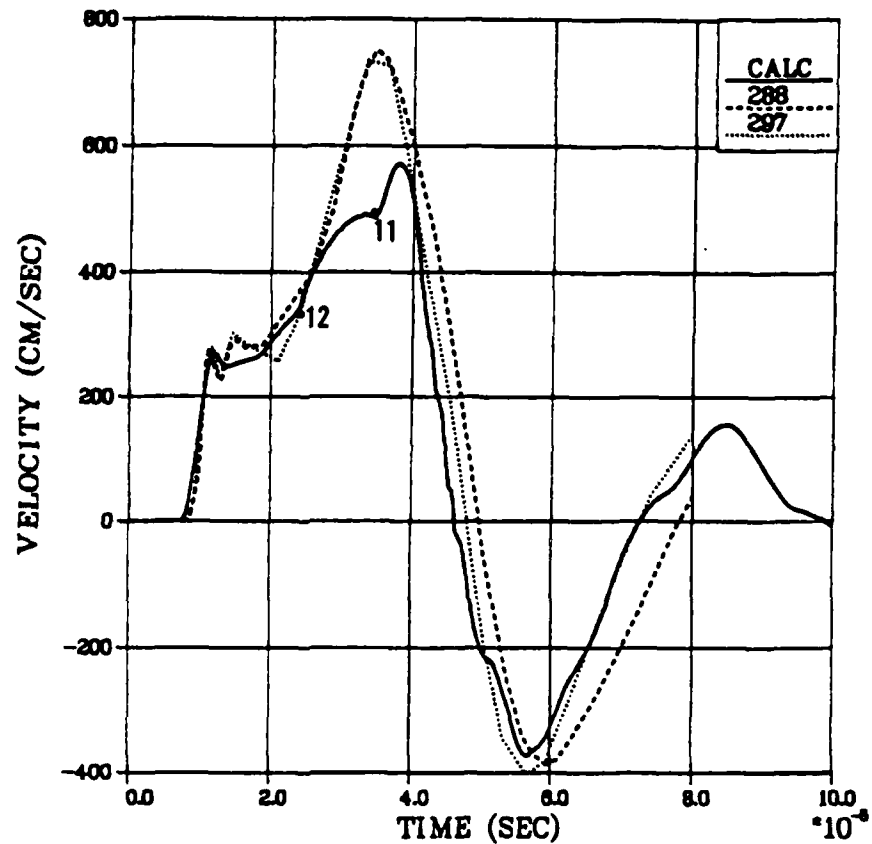


Figure 4.7. Comparison between measured velocities at 2.54 cm in LD2C4 grout and a calculation using the RDD constitutive models showing the effect of increasing the pressure from 0.21 to 0.22 Kb at point 11 from the calculation of Figure 4.6.

PV 288

R = 2.54 (CM)

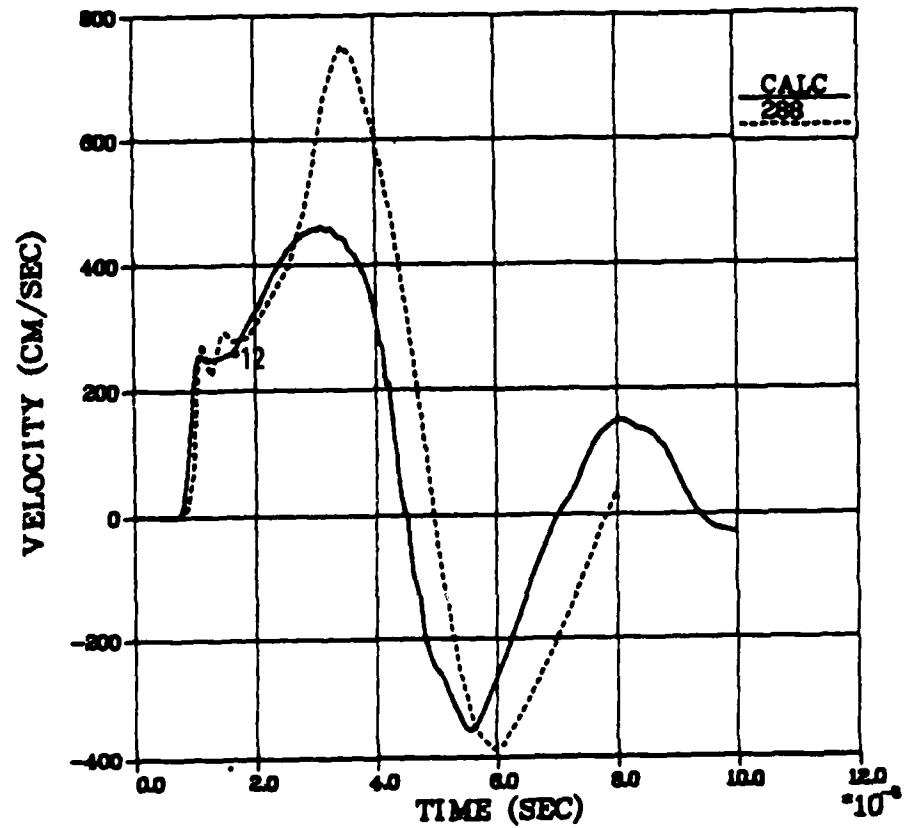


Figure 4.8. Comparison between measured velocities at 2.54 cm in LD2C4 grout and a calculation showing the effect of increasing the pressure at point 11 to 0.25 Kb for slightly different material properties.

PV 288  
PV 297

R = 2.54 (CM)

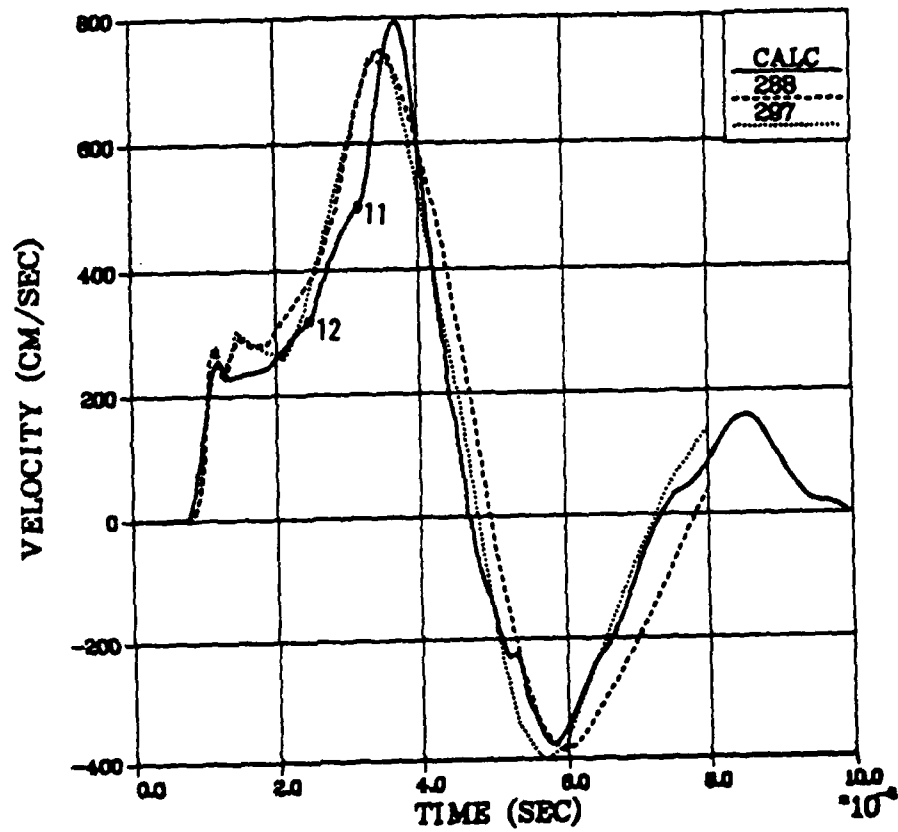


Figure 4.9. Comparison between measured velocities at 2.54 cm in LD2C4 grout and a calculation using the RDD constitutive models showing the effect of decreasing the pressure from 0.21 to 0.20 Kb at point 11 from the calculation of Figure 4.6.

We have been showing how very small systematic variations in the pressure at the bottom of the loading curve can alter the velocity pulse at a representative station. Changes in the specific volume for these data points can alter the velocity pulse somewhat differently. For example, small pressure variations at point 11 substantially changed the slopes of the loading curve both above and below this data point. However, a change in the specific volume at point 11 from 0.518 to 0.519 is subtly different in that the slope below this data point is increased almost 50 percent while above the point it is decreased less than 2.5 percent. Figure 4.10 shows the effect of this change in specific volume on the velocity pulse at 2.54 cm from the calculation of Figure 4.9. Now the change in velocity between points 11 and 12 has been lessened rather than the change between point 11 and the peak. This may alter the general shape of the velocity pulse at greater ranges.

The figures shown above give simulated velocities which are in general agreement with the measurements in spite of small perturbations in crush curve shape. The final crush curve shape (Table 4.2 and Figure 1.11) was arrived at through a trial and error set of calculations which included large variations in data points which gave velocity pulses very different from the measurements. We suggest the following guidelines for simulating velocity pulses in high porosity media. Using the expected general shape of the crush curve, first attempt to obtain approximately the correct width of positive velocity pulse by determining a failure surface. For the RDD models, this involved a choice of reference specific volume  $V_c$  which controls damage. For other constitutive models, it may involve specification of some relation between void crushup and strength reduction. The final cavity radius should provide a guide. Next, work out the detailed crush curve data points beginning at stations closest to the charge and moving outward, i.e., the higher pressure data points will be determined first. These probably have to be adjusted only slightly once the bottom of the crush curve is decided upon.

PW 288  
PW 297

R = 2.54 (CM)

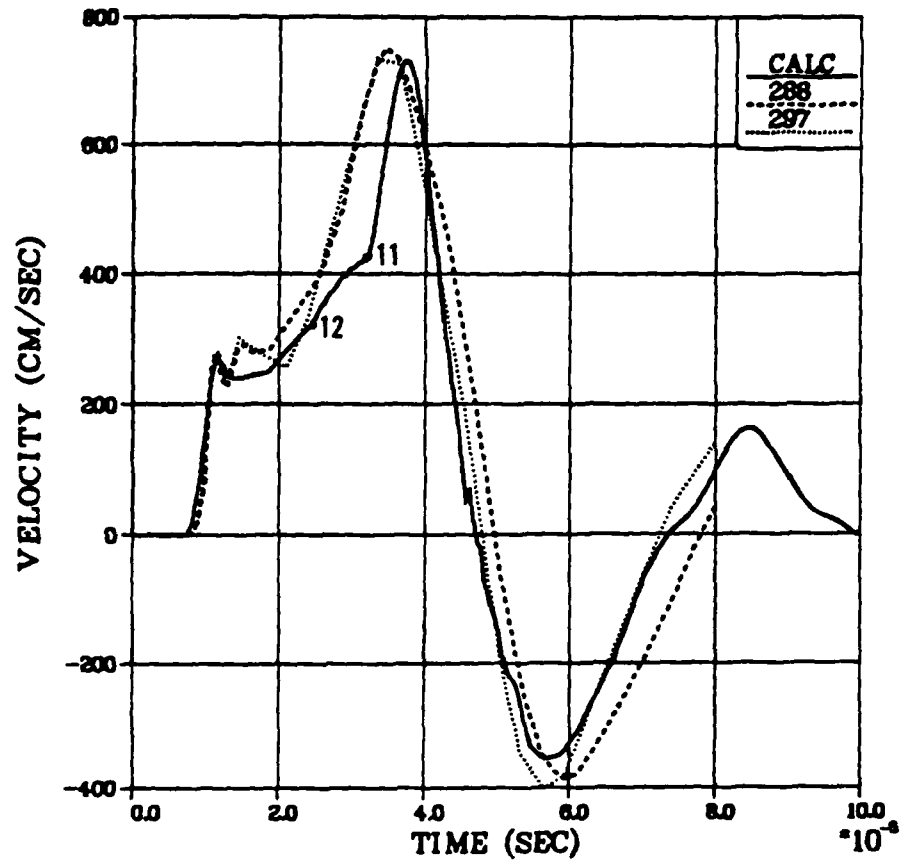


Figure 4.10. Comparison between measured velocities at 2.54 cm in LD2C4 grout and a calculation using the RDD constitutive models showing the effect of increasing the specific volume from 0.518 to 0.519 cc/gm at point 11 from the calculation of Figure 4.9.

#### 4.3 EFFECTIVE STRESS CALCULATIONS FOR LD2C4 GROUT

The effective stress model described in Section 3 for 2C4 grout has been applied to the simulation of the velocity records for LD2C4 grout. For these simulations, the dry strength,  $Y$ , was assumed to be

$$Y = 0.055 + 1.5 \bar{P} \quad (\text{Kb})$$

which is the identical expression used for the static strength in the RDD model. The maximum strength however was raised from 0.22 to 0.505 Kb to approximate the dry condition.

Since the pore fluid pressure and therefore the effective strength of the grout is directly linked to air-void crushup by the functional form in this model, the shape of the crush curve influences strength as well as attenuation. The first effective stress calculation for LD2C4 used our approximation of the measured load curve from Terra Tek (see Table 4.2 and the dotted curve of Figure 1.11). Simulated velocities, shown for the four stations in Figures 4.11-4.14 respectively, are in remarkable agreement with the measurements at three of the four stations especially for a first attempt with a new model. At 2.54 cm, calculated peak velocity is much lower than the measurement. Very small changes at the low pressure end of the crush curve, reduction of the pressure from 0.21 to 0.19 Kb at crush curve point 11 (Table 4.2) and a decrease in specific volume from 0.5201 to 0.5195 cc/gm at point 12, result in the simulated velocities reported by Cherry and Rimer (Reference 5). These calculated velocities differ significantly from those shown in Figures 4.11-4.14 only at 2.54 cm. Figure 4.15 shows the calculated velocities at 2.54 cm (from Reference 5) which are in good agreement with the measurements. However, calculated peak velocity occurs at too late a time. It should be noted that the differences between the crush curve used in this calculation and the measured crush curve is almost certainly less than the accuracy of the laboratory measurements of this crush curve.



PV2 287  
PV2 288

R = 1.27 (CM)

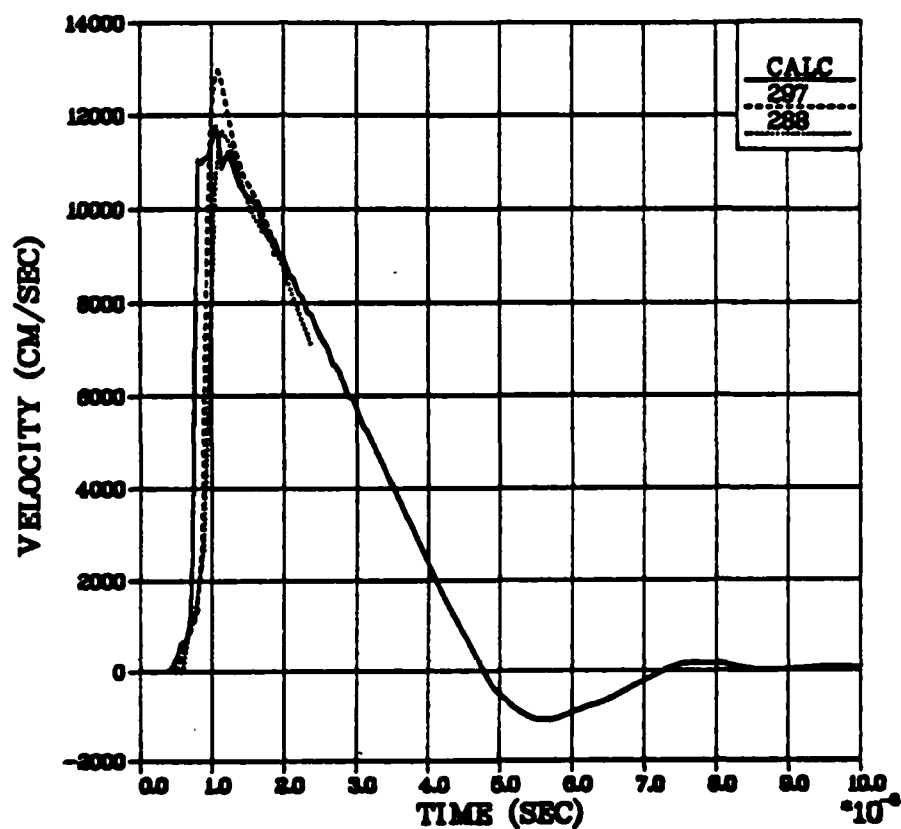


Figure 4.11. Comparison between measured particle velocities at 1.27 cm in LD2C4 grout and the velocities calculated using the measured crush curve (Table 4.2) and the effective stress model for the first time.

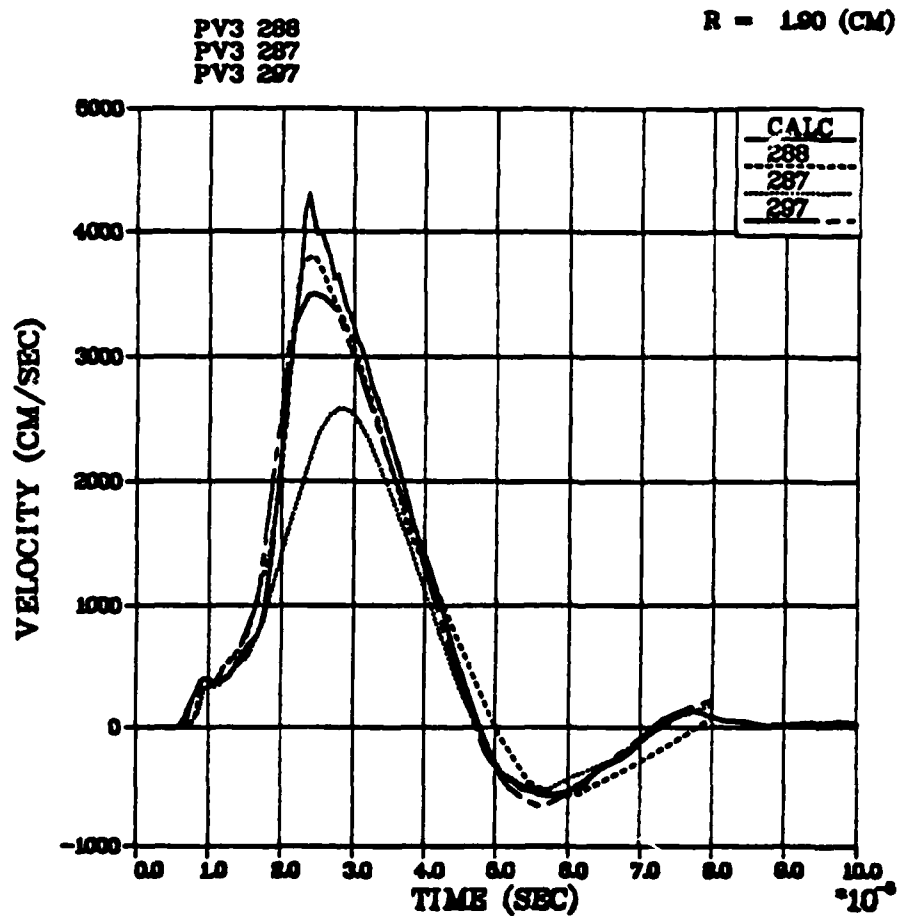


Figure 4.12. Comparison between measured particle velocities at 1.90 cm in LD2C4 grout and the velocities calculated using the measured crush curve (Table 4.2) and the effective stress model for the first time.

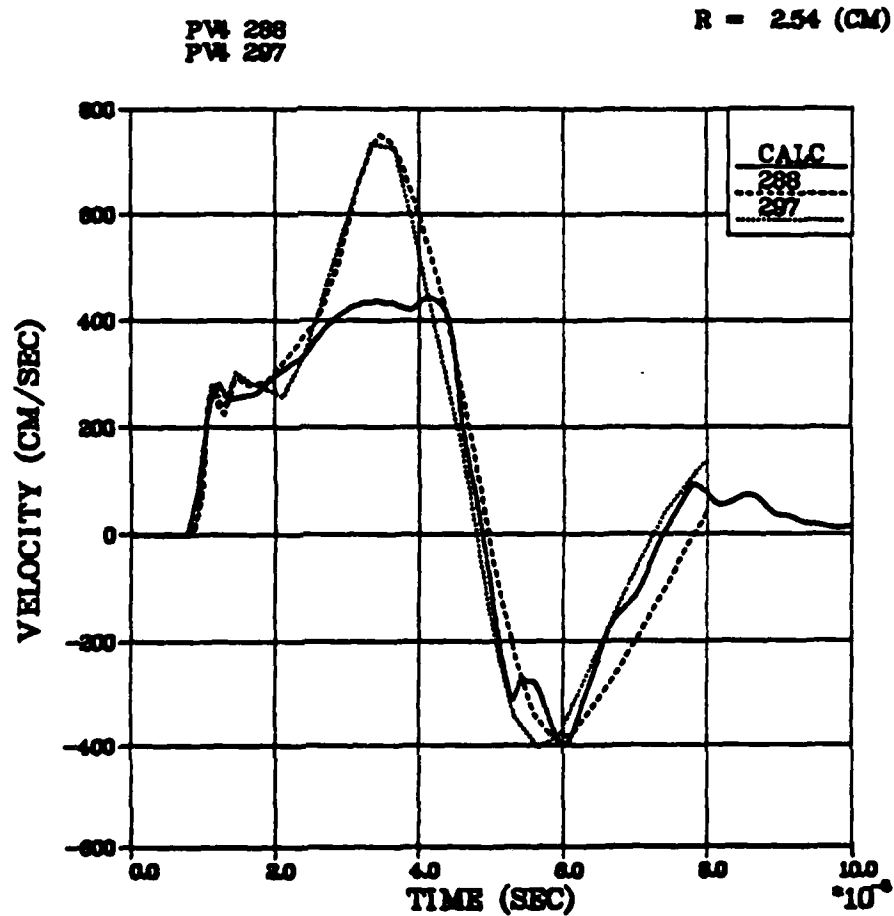


Figure 4.13. Comparison between measured particle velocities at 2.54 cm in LD2C4 grout and the velocities calculated using the measured crush curve (Table 4.2) and the effective stress model for the first time.

PV5 287  
PV5 297

R = 4.00 (CM)

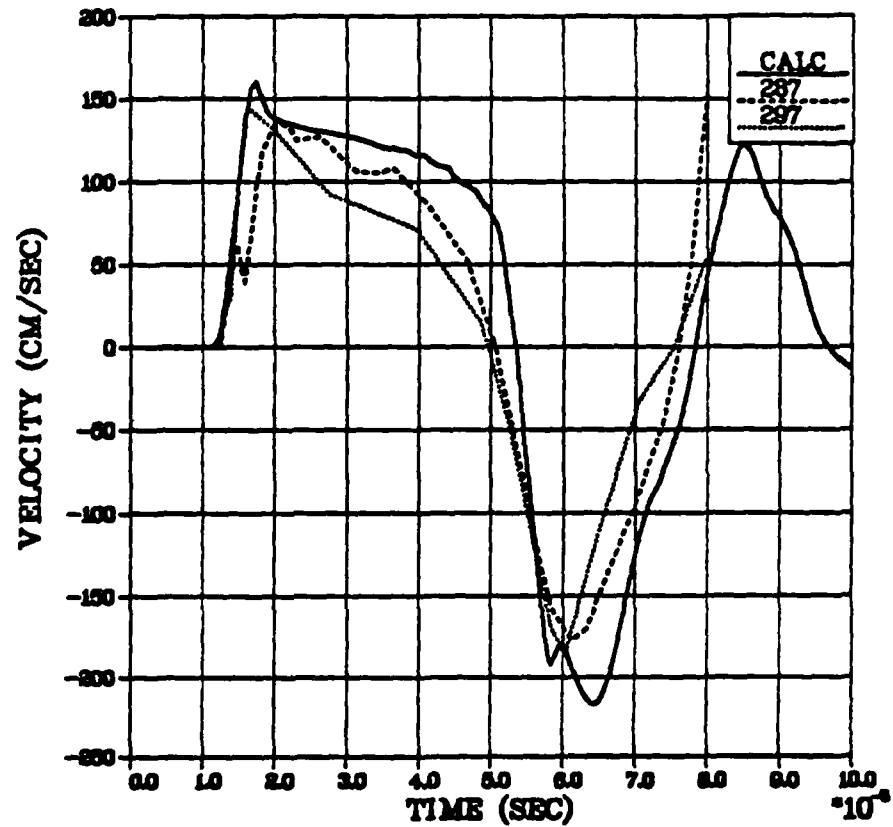


Figure 4.14. Comparison between measured particle velocities at 4.0 cm in LD2C4 grout and the velocities calculated using the measured crush curve (Table 4.2) and the effective stress model for the first time.

PV 288  
PV 297

P = 2.54 (CM)

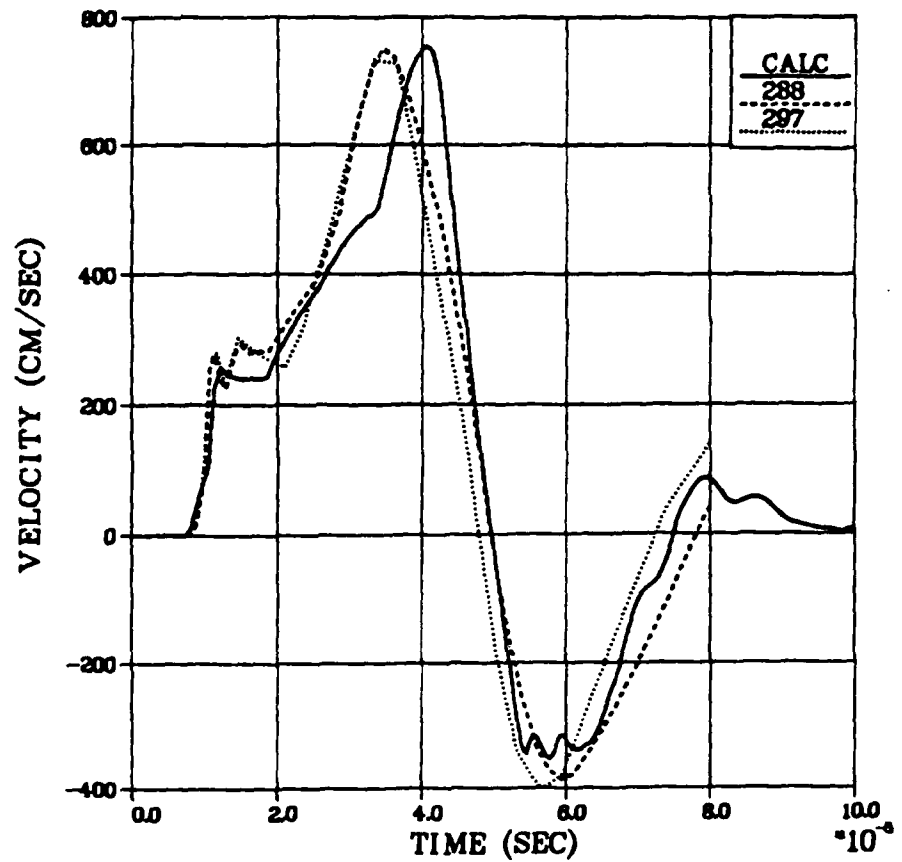


Figure 4.15. Comparison between measured particle velocities at 2.54 cm in LD2C4 grout and the velocities calculated by Cherry and Rimer (Reference 5) using the effective stress model.

The calculations described above applied the effective stress model both during shock loading and subsequent unloading. In line with our previous work for both 2C4 grout and LD2C4 using the RDD models, and for 2C4 grout using the effective stress model, we also simulated the high porosity grout velocity data with the assumption that the strength reductions due to pore fluid pressure buildup occur only on unload. These calculated velocities are shown for the four stations in Figures 4.16-4.19 respectively. This simulation used the measured crush curve of Table 4.1 with data point 11 changed in pressure from 0.21 to 0.20 Kb and in specific volume from 0.518 to 0.5155 cc/gm.

Overall, the calculated velocities are in as good agreement with the measurements as was obtained using the RDD models (Figures 1.6-1.9). Far fewer material properties assumptions are required for the effective stress model than for the complicated rate dependent RDD models. The results do however depend on as yet unverified assumptions about the functional dependence of pore fluid pressure upon air-void crushup. Also, the dry failure surface has not been measured for 2C4 or LD2C4 grout. A measurement of this failure surface for these grouts or for porous earth materials such as tuff or alluvium would be a significant step forward in the verification of the effective stress model.

Figure 4.20 shows the calculated residual stresses from the "best fit" effective stress law simulation for LD2C4 grout. Comparisons with the residual stresses calculated for LD2C4 using the RDD model (Figure 1.10) show similar values of peak compressive hoop stress  $\sigma_\theta$  (within 10 percent) but smaller radial stress peak for the effective stress calculation. In both Figure 1.10 and Figure 4.20, waves are still banging back and forth between the simulated walls of the surrounding water tank and the cavity. Near the cavity itself, the effective stress calculation allows for a far greater stress difference than did the RDD simulation. Calculated cavity radii for the two differ by less than 1.0 percent and are in agreement with the measurements.

PV2 297  
PV2 286

R = 1.27 (CM)

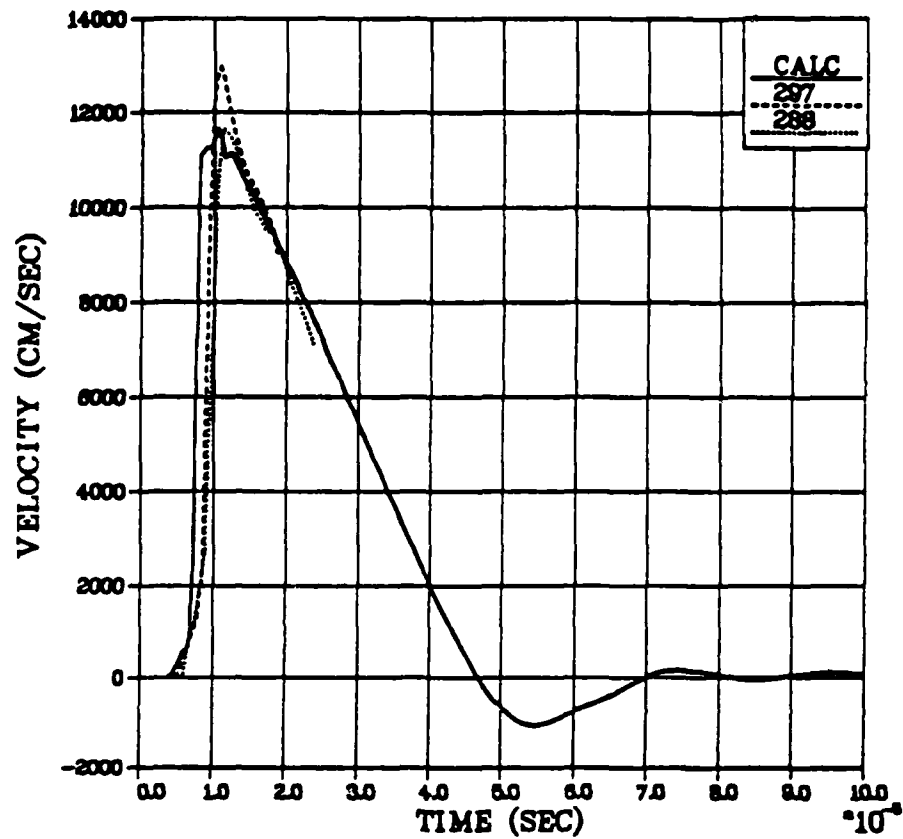


Figure 4.16. Comparison between measured particle velocities at 1.27 cm for LD2C4 grout and "best fit" simulation using the effective stress model.

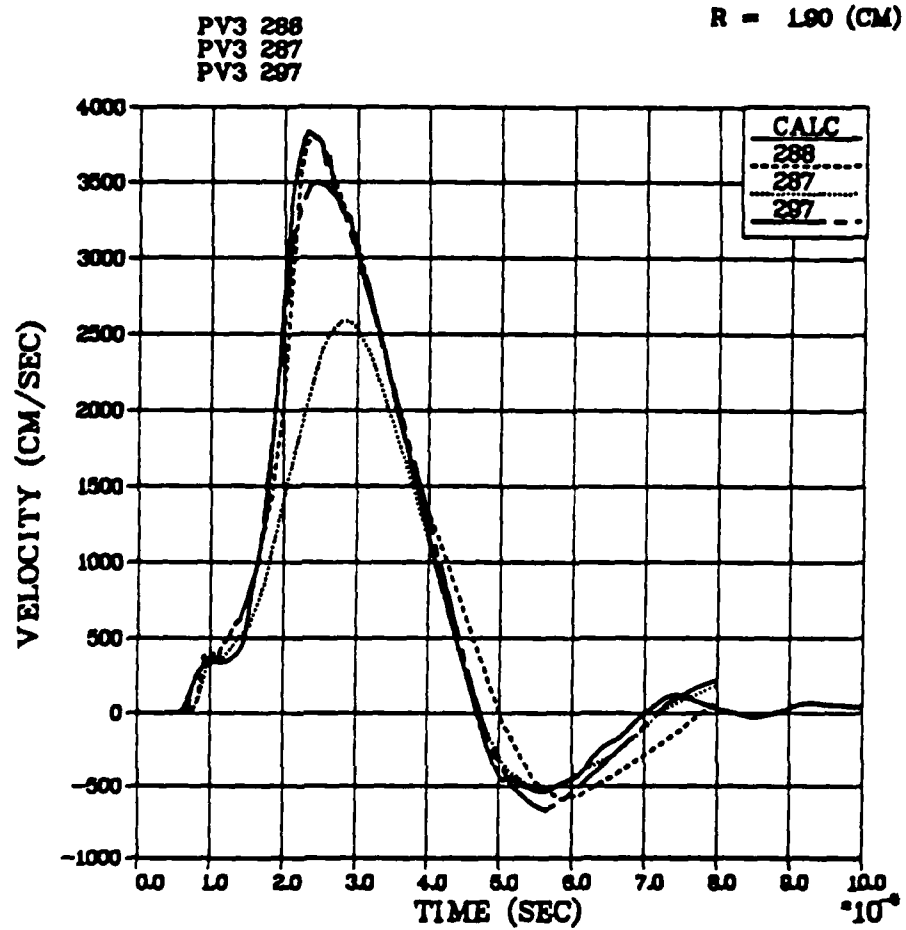


Figure 4.17. Comparison between measured particle velocities at 1.90 cm for LD2C4 grout and "best fit" simulation using the effective stress model.



PW 288  
PW 297

R = 2.54 (CM)

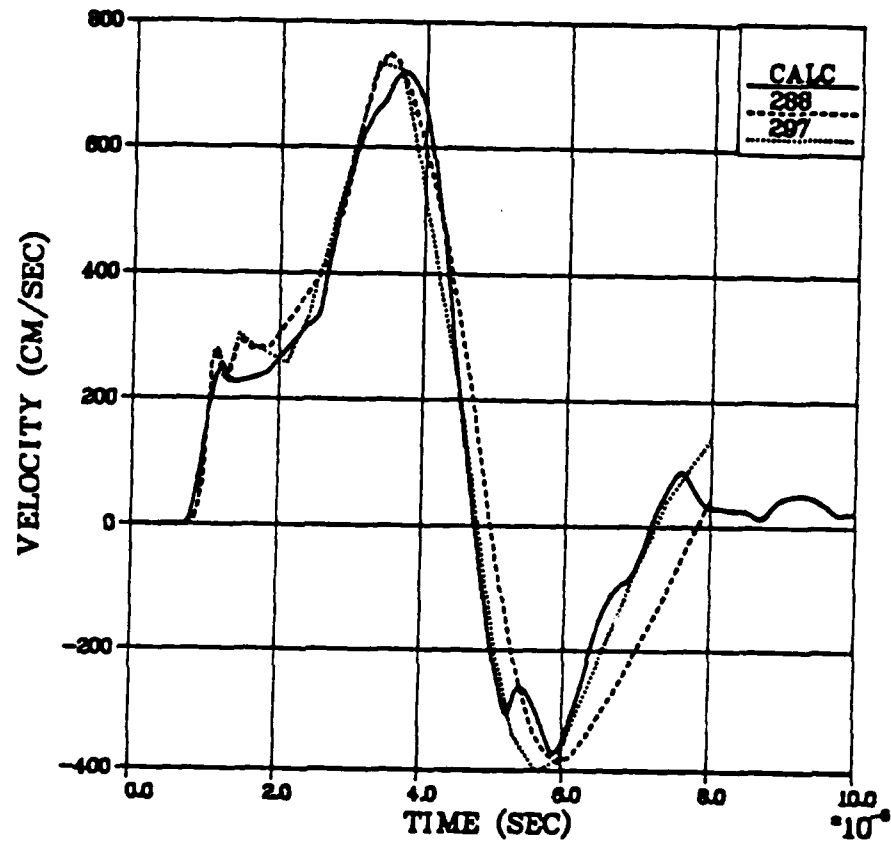


Figure 4.18. Comparison between measured particle velocities at 2.54 cm for LD2C4 grout and "best fit" simulation using the effective stress model.

PV5 287  
PV5 287

R = 4.00 (CM)

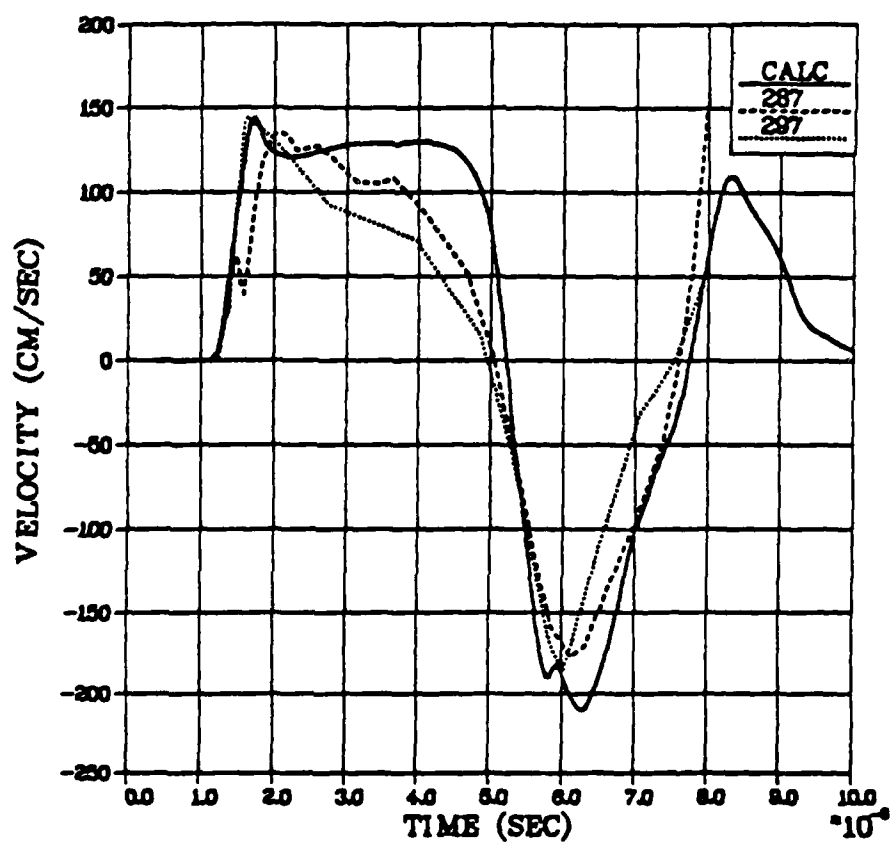


Figure 4.19. Comparison between measured particle velocities at 4.0 cm for LD2C4 grout and "best fit" simulation using the effective stress model.

# Skipper Stress Field LD2C4

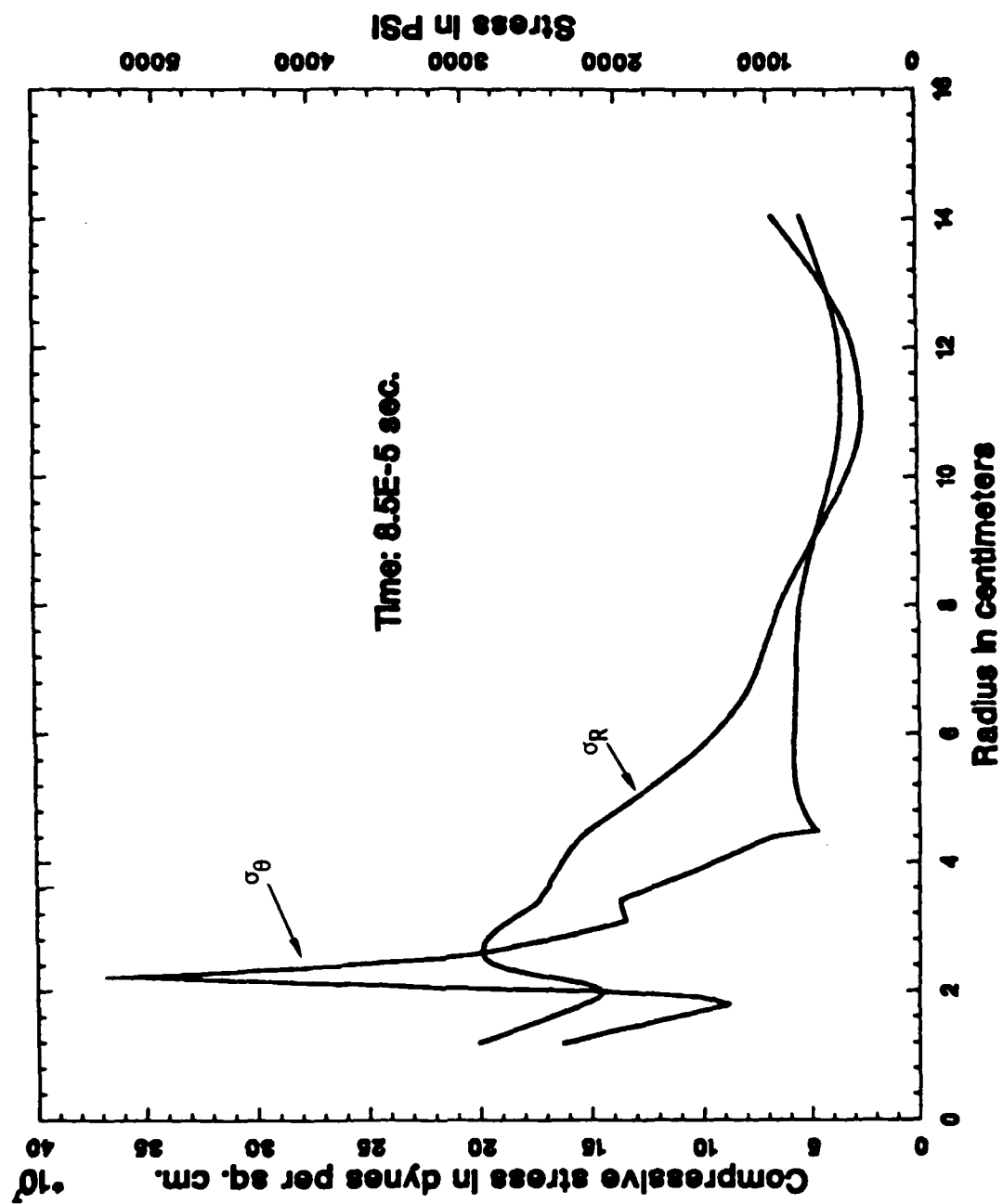


Figure 4.20. Calculated residual stresses for LD2C4 grout at 85 usec using the effective stress model.

#### 4.4 IMPLICATIONS FOR CONTAINMENT

Finite difference calculations have been made which simulate the particle velocity data from the grout spheres experiments in high porosity LD2C4 grout using two different constitutive models. The two calculations gave compressive residual hoop stresses of similar magnitudes, approximately a factor of five greater than overburden. Although the peak hoop stresses calculated for LD2C4 grout were approximately a factor of two lower than for 2C4 grout, their magnitudes were sufficiently high (340 bars) that we would expect significant increases in measured fracture initiation pressures when compared with the unexploded configuration. The experimental results, no increase in fracture initiation pressure for the exploded configuration, strongly indicate a rapid decay of the residual stress fields with time for the high porosity LD2C4 grout. For the highest flow rate hydrofracture measurements, the residual stresses may be reasonably assumed to decay to near overburden within at most a few seconds.

The experimental results bring into question the residual stress concept as a containment mechanism for the hot cavity gases from nuclear events in high porosity materials such as alluvium. Finite difference calculations for events in alluvium are sometimes presented to the Containment Evaluation Panel (CEP) to show the formation of compressive residual stress fields around the nuclear cavity. Although the calculational models used for alluvium have not as yet been validated by comparisons with particle velocity measurements, as was done here for LD2C4 grout, we expect that validated models will indicate the presence of these compressive residual stresses at the end of the dynamic motions (a few seconds). However, it may be necessary to continue these calculations, with appropriate models for creep or stress relaxation, to demonstrate the continued existence of the compressive stress fields for many minutes or until cavity pressure decay is complete or chimney collapse occurs. Residual stress relaxation accompanying cavity gas cooling and pressure decay has been measured by Smith (Reference 26) for 64 lb TNT charges in NTS G-tunnel saturated tuff.

The determination of constitutive models for porous alluvium has been handicapped by the absence of laboratory material properties measurements due to the difficulty of acquiring intact alluvium cores. We have shown that particle velocity measurements at a few ranges together with inexpensive finite difference calculations can be used as a material property measurement, i.e., to develop a crush curve, failure surface, etc., for a porous material, LD2C4 grout. Small insitu high explosive tests in alluvium may be used to develop material properties for alluvium in a similar manner once gauge limitations are overcome. Accurate measurement of both stresses and velocities may lead to a unique constitutive model for alluvium.

For a rock of interest to containment, from which representative cores may be obtained, the SRI small scale explosive tests provide a means for inexpensively determining the validity of our constitutive models. This procedure requires determination in the laboratory of the material properties relevant to the candidate constitutive model. For the effective stress model, this means measurement of the dry failure surface in addition to the standard tests. The question of size effects must be adequately addressed for this procedure to be relevant to containment questions in large scale nuclear tests.

## SECTION 5. CONCLUSIONS

In this report, we have shown that particle velocity measurements together with finite difference calculations may be used to develop a numerical constitutive model which describes the dynamic behavior for two earth-like materials, a saturated grout and a high air-filled porosity grout. In the absence of the stress measurements needed for uniqueness, two very different constitutive models were developed which allowed successful simulation of the particle velocities for both grouts. The particle velocity measurements resulted in the rejection of many other candidate models. The validity of these two models, the rate dependent RDD models, which do not simply scale to other explosive yields, and the rate independent effective stress model, which does scale, may be differentiated between by a simple laboratory experiment at a larger explosive yield.

The two constitutive models have different prescriptions for how material strength is modified by the passage of dynamic shock waves. However, both lead to the same conclusions, that a higher strength than measured from standard laboratory material properties tests is required during shock loading and that a considerably lower strength is required after the loading is completed.

The compressive residual stress fields calculated with either constitutive model are in reasonable agreement with the hydrofracture measurements for saturated 2C4 grout, but are considerably higher for the high porosity LD2C4 grout than would be expected from the hydrofracture data, indicating rapid residual stress relaxation for a high porosity alluvium-like material. This stress relaxation brings into question the residual stress concept as a mechanism for the containment of hot cavity gases for events in porous alluvium.

The procedure of using particle velocity measurements to develop material properties was tested for LD2C4 grout and resulted in the determination of a crush (loading) curve which was in excellent agreement with a crush curve measured in the laboratory. Thus, good particle velocity measurements from insitu high explosive tests may be used to obtain a crush curve for a material such as alluvium in which core samples are not available. When core is available, cylinders of this material may be tested on a small scale using the SRI explosive configuration and laboratory material properties data to measure our modeling success for the rock of interest to containment.





## REFERENCES

1. Cizek, J.C. and Florence, A.L., "Laboratory Investigation of Containment in Underground Nuclear Tests", SRI International Final Report for 1980, DNA 5731F, Feb 1981.
2. Cizek, J. C. and Florence, A.L., "Laboratory Investigation of Containment in Underground Nuclear Tests", SRI International Draft Final Report for 1981, submitted to DNA, Dec 1981.
3. Rimer, N. and Lie, K., "Spherically Symmetric Numerical Simulation of the SRI Grout Spheres Containment Experiments", S-CUBED Topical Report SSS-R-79-3831, submitted to DNA, October 1978.
4. Rimer, N. and Lie, K., "Spherically Symmetric Calculations of the SRI Grout Spheres Experiments for Four Different Laboratory Configurations", S-CUBED Topical Report SSS-R-80-4240, submitted to DNA, November 1979.
5. Cherry, J.T. and Rimer, N., "Simulation of the Effective Stress and Air Void Porosity Constitutive Models", S-CUBED Report SSS-R-82-5610, submitted to ARPA August, 1982.
6. Cizek, J. C. and Florence, A. L., "Laboratory Investigation of Containment of Underground Explosions", SRI International Bimonthly Progress Report No. 2, Submitted to DNA, March 1982.
7. Smith, R. D., Letter from Terra Tek, Inc., to Mr. Joe W. Lacombe, FCTC, dated May 3, 1982.
8. Lee, E., Finger, M., and Collins, W., "JWL Equation of State Coefficients for High Explosives," Lawrence Livermore Laboratory report UCID-16189, January 1973.
9. Finger, M., Private communication, June 8, 1976.
10. Duff, R., Private communication, July, 1977.
11. Cizek, J.C., and Florence, A.L., "Laboratory Investigation of Containment in Underground Nuclear Tests", SRI International draft Final Report for 1977, PYU-5958, submitted to DNA, January 1978.
12. Cizek, J. C., and Florence, A.L., "Laboratory Investigation of Containment in Underground Nuclear Tests", SRI International Final Report for 1978, DNA 4847F, January 1979.
13. Cizek, J. C. and Florence, A.L., "Laboratory Investigation of Containment in Underground Nuclear Tests", SRI International Final Report for 1979, DNA 5601F, January 1980.

14. Ehrgott, J.Q. (WES), letter to J. W. LaComb (DNA), July 8, 1981.
15. Cooley, E. H., Sakellariou, C. Butters, S.W., Schatz, J.F. and LaComb, J. W., "Material Properties of 2C4 Grout in Support of Nevada Test Site Nuclear Test Program", TerraTek Inc. Report TR 81-56, May 1981.
16. Cherry, J.T., Rimer, N., and Wray, W.O., "Seismic Coupling from a Nuclear Explosion: The Dependence of the Reduced Displacement Potential on the Nonlinear Behavior of the Near Source Rock Environment", Systems, Science and Software Technical Report SSS-R-76-2742, September 1975.
17. Tillotson, J.H., "Metallic Equations of State for Hypervelocity Impact", General Atomic Report GA-3216, July 1962.
18. Maenchen, G. and Sack, S., "The Tensor Code" in Methods in Computational Physics, Vol. 3, Academic Press, New York, 1964.
19. Vutukuri, V. S., Lama, R.D., and Saluja, S.S., "Handbook on Mechanical Properties of Rocks, Series on Rock and Soil Mechanics, Vol 2., No. 1, Pages 45-48, 211, Trans Tech Publications, 1974.
20. Patch, D.F., DNA Ground Motion Calculators Meeting at S-CUBED, April 14, 1981.
21. Wilkins, M.L., "The Calculation of Elastic-Viscous-Plastic Effects in Materials", in Shock Waves and the Mechanical Properties of Solids, Proceedings of the 17th Sizemore Army Materials Research Conference, Sept. 1-4, 1970, editors J. H. Burke and V. Weiss, Syracuse University Press.
22. Bache, T.C., Blake, T.R. Cherry, J.T., Barker, T.G., Lambert, D.G., Savino, J. M., and Rimer, N., "An Explanation of the Relative Amplitudes of the Teleseismic Body Waves Generated by Explosions in Different Test Areas at NTS", S-CUBED Final Report, DNA-3958F, October, 1975.
23. Heard, H.C., "The Influence of Environment on the Inelastic Behavior of Rocks", in Engineering with Nuclear Explosives, Vol. 1, available from the Clearing House for Federal Scientific and Technical Information, National Bureau of Standards, Springfield, Virginia, January 1970.
24. Garg, S.K., and Nur, A., "Effective Stress Law for Fluid-Saturated Porous Rocks", JGR, 78, pp 5911-5921, 1973.
25. Cherry, J.T., and Peterson, F.L., "Numerical Simulation of Stress Wave Propagation from Underground Nuclear Explosions", in Engineering with Nuclear Explosives, Vol. 1, January 1970.
26. Smith, C.W., "Contained Nuclear Explosion Models - High Explosive Simulation", Proceedings of Monterey Containment Symposium, August 1981.

## DISTRIBUTION LIST

### DEPARTMENT OF DEFENSE

Defense Nuclear Agency  
ATTN: SPTD, T. Kennedy  
4 cy ATTN: TITL  
  
Defense Technical Information Center  
12 cy ATTN: DO

Field Command  
Defense Nuclear Agency  
ATTN: FCTT, W. Summa  
ATTN: FCTT, G. Ganong  
ATTN: FCT, COL G. Ballantine  
3 cy ATTN: FCTK, B. Ristvet  
3 cy ATTN: FCTK, C. Keller

### DEPARTMENT OF ENERGY

Nevada Operations Office  
ATTN: P. Mudra

### OTHER GOVERNMENT AGENCY

Department of the Interior  
US Geological Survey  
ATTN: R. Carroll  
ATTN: P. Orkild

### DEPARTMENT OF ENERGY CONTRACTORS

Desert Research Institute  
Attention D. Schulke Sec Off  
ATTN: P. Fenske  
ATTN: C. Case

University of California  
Lawrence Livermore National Lab  
ATTN: B. Hudson  
ATTN: F. Morrison  
ATTN: L-209, G. Higgins  
ATTN: R. Terhune  
ATTN: L. Makague  
ATTN: C. Olsen

### DEPARTMENT OF ENERGY CONTRACTORS (Continued)

Los Alamos National Laboratory  
ATTN: F. App  
ATTN: R. Brownlee  
ATTN: C. Keller  
ATTN: T. Kunkle, ESS-5  
ATTN: B. Travis

Sandia National Lab  
ATTN: Org 7112, C. Mehl  
ATTN: R. Bass  
ATTN: C. Smith

### DEPARTMENT OF DEFENSE CONTRACTORS

California Research & Technology, Inc  
ATTN: M. Rosenblatt

Kaman Tempo  
ATTN: DASIAC

Pacific-Sierra Research Corp  
ATTN: H. Brodie, Chairman SAGE

Pacifica Technology  
ATTN: D. Patch

Physics International Co  
ATTN: L. Miller, Dept 4600  
ATTN: J. Thomsen

R&D Associates  
ATTN: P. Haas

S-CUBED  
ATTN: C. Dismukes  
ATTN: R. Duff  
4 cy ATTN: N. Rimer  
4 cy ATTN: K. Lie

SRI International  
ATTN: A. Florence



END

DATE  
FILMED

9 - 83

DTIC